Doctoral Thesis

Vapor phase deposition of functional nanocomposite thin films and their modification by ion beam irradiation

Submitted by

Venkata Sai Kiran Chakravadhanula

Supervised by

Prof. Dr. Franz Faupel

Multicomponent Materials,
Technical Faculty of the Christian-Albrechts-University of Kiel

April 21, 2011

Tag der Prüfung : 21.04.2011
Tag der Druckgenehmigung : 27.04.2011

Referrent : Prof. Dr. Franz Faupel
Koreferrent : Prof. Dr. Lorenz Kienle

Contents

Chapter 1

Introduction

Advanced functional materials are a prerequisite for many major research and development areas like informatics, medicine, energy and environment, the transport industry and space exploration. Sophisticated nanomaterials and systems with novel functional properties are a major desire. Much of this interest is powered by the growing expertise in fabrication methods that allow increasingly sophisticated ways of realizing nanostructures with well–controlled composition, size, and shape [1]. The development of synthetic methodologies has also advanced to a level where nanostructures are produced from many kinds of materials with the required quality, quantity, and yield for the systematic investigation of their peculiar properties. The precise synthesis of nanoparticles with well defined properties is a prerequisite for the development and design of high–tech coatings based on selective high–surface area materials of consolidated bulk materials [2, 3]. Additionally, for the case that the nanoparticles are embedded in a matrix, the later also determines different physical properties.

Nanostructured materials exhibit properties that are not observed for macroscopic feature sizes. Examples related to metallic nanoparticles in a dielectric matrix include electronic conductivity ranging from tunneling to percolation, surface plasmons giving rise to characteristic optical absorption [4–6] and enhancement of catalytic activity [7, 8]. As a consequence, such nanocomposite coatings have been of strongly increasing fundamental interest and great technological importance during the last decade [9–12].

Organic frameworks [13] and metal oxide supports [14] have frequently been used to maintain the dispersion of functional noble metal nanoparticles. Oxide materials like TiO_2 are active hosts not only for promoting catalytic performance [14–16] but also antibacterial effects [17]. Polymers and oxides are particularly attractive as dielectric matrices since they are generally versatile, and can be easily processed into thin films. Several oxides such as TiO_2 [18, 19], SiO_2 [20], ZnO [21], Al_2O_3 [22], MgO [23] and Indium Tin Oxide (ITO) [24] exhibit interesting properties. These functional properties can be further enhanced when the materials are used as a host matrix to form nanocomposites together with noble metal nanoparticles.

In this work, the synthesis and characterization of such nanocomposites, their associated properties, optical and antibacterial as well as modification of nanocomposites by swift heavy ion (SHI) irradiation are addressed. Despite the existence of various approaches towards the synthesis of nanocomposites, vapor phase deposition techniques like co–sputtering and co–evaporation are preferable because of being solvent–free and industrially viable [25]. Ag and Au nanoparticles embedded in different dielectric matrices, i.e., TiO_2 and PTFE, were synthesized by co–sputtering with varying metal volume fractions (MVFs) and were irradiated by SHIs.

Ion beams are important and unique tools in modern science and technology [26]. The availability of fast and heavy ions permits research on strongly perturbed solid–state regions. Fast and heavy ions deposit more energy in a restricted local region than the most powerful lasers currently available, being far from thermal equilibrium. The extremely high energy that can be deposited along the flight path of an ion can destroy the chemical bonds, so that permanent material modifications are left in the track [27]. The interaction of the ion with material is the key factor in the ion beam induced material modification in the form of ion tracks or the effects of overlapping ion tracks [28–30]. The effects of ion beams on the material depends upon the ion energy, the fluence and the ion species [31, 32]. High energy ions (energy $>$ 1 MeV/nucleon) with a velocity equivalent to the Bohr velocity, known as SHIs, have been used for engineering the functional properties of materials [33]. The modification of any particular property depends on the amount of energy deposited into the

material by the SHIs.

In this work, the primary focus has been on the SHI induced modifications in functional properties of the nanocomposites. The SHI beamlines from both the Hahn–Meitner–Institute (HMI) in Berlin, Germany and the Inter University Accelerator Center (IUAC) in New–Delhi, India, were used in this work for producing modifications in the morphology, optical and antibacterial properties of various nanocomposites.

Characterization of the pristine and irradiated nanocomposites in regards to the structure and morphology, optical and antibacterial properties have been carried out. Transmission electron microscopy (TEM) is one of the most powerful tools to understand the morphology and structure of nanoparticles directly in the matrix material and was used in this work. Additionally the 3D morphological analysis by electron tomography of the TiO_2 based nanocomposites was conducted in the later stage of the thesis due to the availability of a sophisticated state-of-art TEM.

While the interaction of light with metallic nanoparticles is determined by their collective electronic or plasmonic response, a compelling analogy exists between plasmon resonances of metallic nanoparticles and wave functions of simple atoms and molecules. Both the size and the interparticle distances play a major role in determining the optical properties of these nanocomposite thin films [34–36]. The optical properties of nanocomposites consisting of noble metal nanoparticles in a dielectric matrix are critically dependent on the particle size, shape, composition and interparticle distance. In this work UV–Vis/NIR spectroscopy was used to investigate the optical properties of the nanoparticles in order to obtain information about the nanocomposites [1, 35]. The combination of both, advanced TEM techniques and UV-Vis spectroscopy yields information on the correlation between the optical properties and the underlying geometric features of the nanocomposites [12].

Silver, gold and copper nanoparticles can directly interact with some functional groups of many bacterial cell membranes, and thus have strong cytotoxicity to various bacterial cells at lower metal usage compared to that required for bulk metals [37–43]. Apart from the excellent optical properties of the silver based nanoparticles [44], the silver ions released from the silver based nanoparticles are known to inhibit bacterial growth, thus leading to

the fact that silver nanoparticles are good antimicrobial agents [45–47] on some bacteria, viruses, algae and fungi. Germicidal effects of silver kill many microbial organisms in vitro, but testing and standardization of silver products proved to be rather difficult [48]. Also, Ag nanoparticles are being doped by Titania for higher efficacy than pure silver nanoparticles towards the inhibition and annihilation of E.coli bacteria [49]. Additionally, Ag nanoparticles embedded in different matrices have become quite important because of the prospective applications such as in imaging, biosensing, biodiagnostics, optical filters, antimicrobial, water purification, catalytic and photocatalytic processes [18,45,50–54]. TiO_2 itself is known to be antibacterial when irradiated by UV light [55]. In this work the antibacterial properties of these coatings, i.e., TiO_2, Au–TiO_2 and Ag–TiO_2 through florescence microscopy have been investigated by the group of Prof. Dr. Podschun. As the silver ion release plays an important role, it has been investigated with respect to the silver volume fraction in the Ag–TiO_2 nanocomposites in the preliminary studies. X–ray photoelectron spectroscopy and the UV–Vis spectroscopy were used for these studies. Additionally, it has been shown that the silver ion release is enhanced after ion beam irradiation.

The temperature appears to be among the main criteria for the nanocomposites' application, as its variation results in the modification of the microstructure and thereby the functional properties [56]. In–situ microscopy refers to the techniques that allow a direct observation of the dynamic properties at nanoscale through imaging and diffraction. Thus heating and cooling experiments within the TEM are powerful techniques for understanding temperature effects by real–time observation [57, 58]. In–situ heating studies of Ag–TiO_2 and Au–TiO_2 in the transmission electron microscope, a comparison with the modification by SHI was carried out.

The thesis is organized in seven chapters as follows:

Chapter 1 deals with the introduction into the field of nanocomposites, optical properties and SHI irradiation.

Chapter 2 deals with the theories associated at various stages of this work.

Chapter 3 deals with the experimental and characterization techniques employed in this work.

Chapter 4 deals with the synthesis of metal–TiO_2 nanocomposites, tomographic studies, and associated SHI induced modifications. An insight into the antibacterial functionality and optical properties of these nanocomposites is given. A comparison with the in–situ heating in the transmission electron microscopy with the SHI is discussed as there is microstructural modification in amorphous TiO_2 thin films during annealing [59].

Chapter 5 deals with the synthesis of metal–polymer nanocomposites and multi–layered systems with the associated SHI irradiation induced modifications.

Chapter 6 summarizes the work.

Chapter 7 gives an outlook.

Chapter 2

Theory

2.1 Vapor phase deposition

Several approaches such as reduction of a metal salt [60], ball milling [61], plasma polymerization in conjunction with metal deposition [62], co–evaporation of a metal and an organic component [63] and co–sputtering [64, 65] have been reported to produce functional nanocomposites. Many applications require good control of the MVF and composition of the particles. Generally wet chemical approaches are usually less or not suited. In most cases, vapor phase deposition has proven to be very successful [64, 66].

Vapor phase deposition processes involve the controllable transfer of atoms from a source to a substrate where film formation and growth proceed atomistically. Due to the absence of impurities, vacuum deposition has the advantage to be a very clean method. The better the vacuum, the longer is the "mean free path" for collisions of atoms and high–energy ions.

The basic vapor phase deposition methods to produce thin films are physical vapor deposition (PVD), i.e., evaporation and sputtering and chemical vapor deposition (CVD).

CVD is a chemical process referring to the formation of a non–volatile solid film on a substrate from the reaction of vapor phase chemical reactants containing the right constituents. In a typical CVD process, the substrate is exposed to one or more volatile precur-

sors, which react and/or decompose on the substrate surface to produce the desired film.

PVD process depicts a family of processes where at least one of the reactants, not in a gas phase is dispersed in a high vacuum chamber by either evaporation, sputtering, or arc–evaporation.

Evaporation involves the removal of atoms from the source by thermal means, whereas sputtering involves their dislodgement from the source surface through impact of gaseous ions. Evaporation has the advantages of good deposition rates, better vacuum, thus, cleaner environments for film formation and growth, and general applicability to all classes of materials.

Plasma deposition like sputtering involves collisional impact by which source atoms enter the gas phase. This deposition is based on the presence of vacuum, but is carried out by pumping a certain amout of additional gas into the chamber. The gas pressure plays an important role in the density of charged and uncharged particles and the energy distribution of particles in the plasma, when plasma is established in a vacuum. Plasma in good vacuum provides an ion source that can be accelerated to high energies in an electric field. In this work the preparation of nanocomposite films was carried out using co–sputtering from two sources simultaneously.

2.1.1 Sputtering

Sputtering is the erosion of solid surfaces during ion bombardment [67,68]. Sputtering is the name given to the result of momentum transfer between gas ions and the target. Physical sputtering is a non–thermal vaporization process. As mentioned earlier, sputter deposition involves additional gas. This can be done in low pressure gas (< 1 mbar), where the sputtered particles do not suffer gas phase collisions in the space between the target and the substrate. The deposition under such conditions often leads to compressive stress within the deposited film due to the densification by the high energy impact. On the other hand, sputtering can also be done using a high gas pressure (>10 mbar) where the energetic particles that are sputtered or reflected from the target are subjected to collisions, having two effects:

Firstly, the collisions will thermalize the ions before they reach the substrate. Secondly, they reach the substrate under various angles, alloying the deposition on complex surfaces. A simple model of some processes that may occur when an ion strikes a cathode surface was developed by Wehner and Anderson [69], where chemical effects were ignored and the atoms were treated as spheres. Fig. 2.1 is a schematic depicting the energetic particle bombardment effects on surfaces and growing films [70]which depends on the type of ion (mass, charge), the nature of surface atoms involved and on the ion energy.

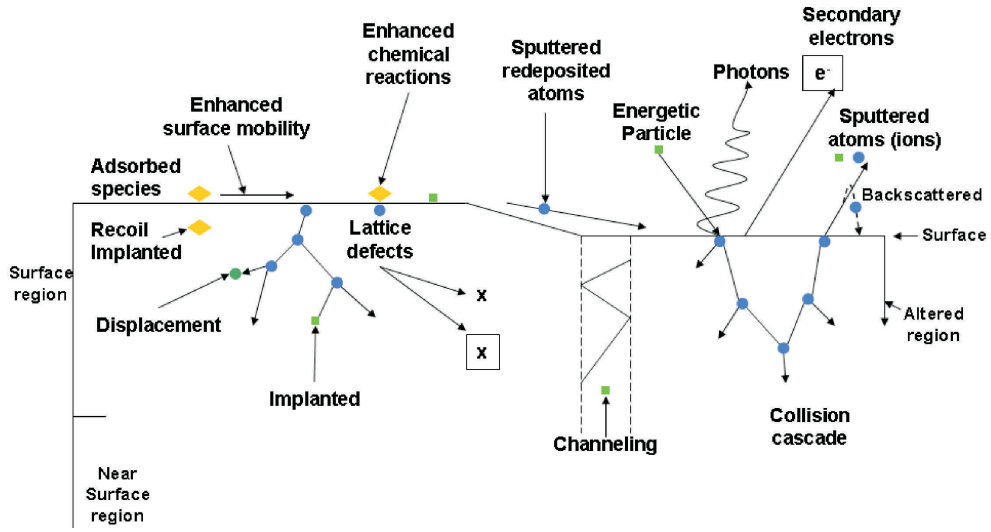

Figure 2.1: *Labeled schematic depicting the energetic particle bombardment effects on surfaces and growing films [70].*

Sputtering techniques are usually classified under DC, RF, magnetron and reactive. Combinations of these techniques also exist. In the scope of this dissertation magnetron sputtering, DC and RF were used. DC–sputtering is the oldest and simplest sputtering technique and is limited to electrically conducting materials. In DC–sputtering, a constant potential difference between anode and cathode is applied. The potential difference applied between cathode and anode drops completely in the first millimeters in front of the cathode. This cathode voltage drop sustains the plasma by accelerating secondary electrons emitted for the cathode. Thus, to sustain a DC–discharge, the electrodes have to be conducting. In this work, the metallic components have been sputter deposited by using a DC magnetron sputtering. If one or both are non–conductive, e.g., deposition of dielectric films, the electrodes will be charged up due to the accumulation of positive or negative charges

and the discharge will be extinguished. To overcome this problem an alternative voltage (RF–sputtering) can be applied between cathode and anode, and the charge accumulated during half cycle will be partially neutralized by the opposite charge accumulated during the next half cycle. Thus charge build–up on insulating targets is avoided with the use of RF–sputtering where the sign of the anode–cathode bias is varied at a high rate. RF–sputtering works well to produce highly insulating oxide films, polymeric films but only with the added expense of RF power supplies and impedance matching networks. Stray magnetic fields leaking from ferromagnetic targets also disturb the sputtering process. In this work, the dielectric components, i.e., PTFE and TiO_2 have been deposited using RF magnetron sputtering.

In addition to this a magnetic field can also be applied. The most well known type of sputtering characterized by magnetron discharge is called magnetron sputtering and can be divided in cylindrical, circular and planar [71]. In planar magnetron sputtering an axisymetric magnetic field is applied with a permanent magnet behind the cathode in such a way that the magnetic field lines start and return at the magnet, as shown in Fig. 2.2. Thus, a "magnetic ring" is formed at the cathode surface and will be responsible to trap the electrons that are accelerated away from the cathode. These electrons will move in helices around the magnetic field lines and they will travel a much longer path–length in the plasma than in conventional glow discharges, increasing the ionization collisions and consequently the ion fluxes.

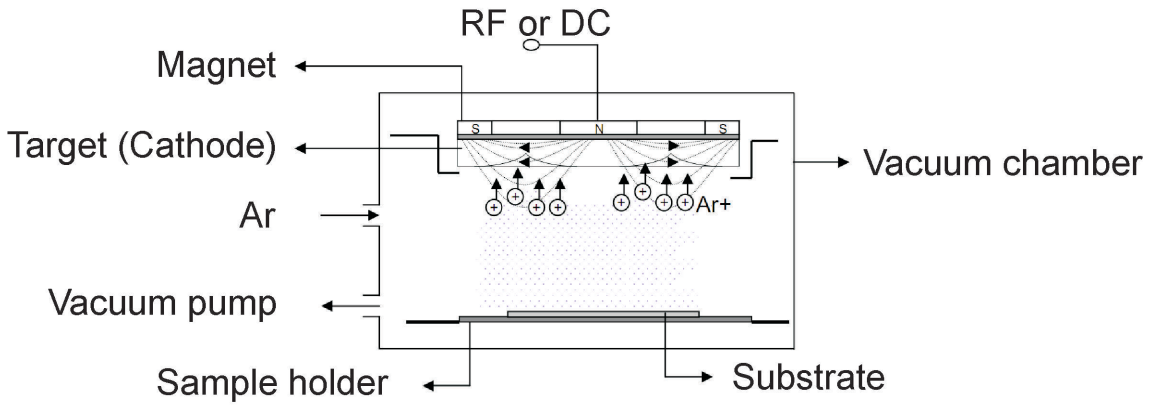

Figure 2.2: *Schematic depicting a magnetron sputtering device.*

The most common sputtering sources are planar magnetrons in which the plasma is magnetically confined close to the target surface, thereby achieving a higher sputter rate. This also enables reactive sputtering of compound films. Sputtering is used in this work to deposit thin films of nanocomposites.

Sputter targets play a pivotal role in the entire process of sputtering. Generally, the metal targets are fabricated by melting either in vacuum or under protective atmospheres, followed by thermomechanical processing. Non–metallic targets are generally prepared by hot–pressing of powders. The metal (Au/Ag) targets tend to have purities of 99.99 %, whereas those of the non–metals (TiO_2) are generally less pure with a typical upper purity limit of 99.9 %. These metallurgical realities are sometimes reflected in emission of particulates, release of trapped gases non–uniform target erosion and deposited films of inferior quality. Targets are available in a variety of shapes (e.g., disks, toroids, plates, etc.) and sizes.

2.1.1.1 Advantages of sputter deposition

- Sputtered films have better adhesion as they can penetrate through high residual gas absorbed on the surfaces, due to the high impact velocity.
- Sputter targets have longer life time being quiet suitable even for industrial applications. Large selection of materials can be used for sputter deposition and even on larger areas.
- In magnetron sputtering, reactive sputtering can be easily accomplished using reactive gaseous species activated in plasma.
- Compact design can be realized as source and substrate can be placed in close optimum distance.

2.1.1.2 Disadvantages of sputter deposition

- Sputter rates, i.e., deposition rates of some materials are lower than those that can be obtained through other methods like evaporation.
- In magnetron sputtering, targets are not used efficiently, as a result of preferred local material removal.
- The plasma can produce reactive radicals from the rest gas atoms.
- Difficulty exists in sputtering of magnetic materials through magnetron sputtering.

2.1.2 Nucleation and growth of noble metals in PTFE and TiO_2

Contrasting properties of metals and polymer/oxides are exhibited while metals are densely packed crystalline solids with a high cohesive energy and polymers are made up of large covalently bonded macromolecules held together by weak van der Waals interactions in an open structure. Cohesive energy of Metals in typically two orders of magnitude higher than that of polymers [72]. Suitable polymers for sputter deposition were investigated in detail through the interaction of low energy ions with polymers in the group of multicomponent materials [73]. The competition between chain scission and crosslinking is pivotal. Generally, Polymers with a high sputter rate should exhibit a low crosslinking tendency. Teflon exhibits a sputter yield which is about two orders of magnitude above that of most other polymers [65,73]. Biederman [64] also reported the excellent suitability of Teflon for sputter deposition. On the other hand, deposition of TiO_2 films is also known through the method of sputter deposition [59, 74]. Condensation coefficient C (often also denoted as sticking coefficient) is the ratio of the number of adsorbed metal atoms to the total number of metal atoms arriving at the surface, which plays a significant role in evaporation. C of metal atoms on metals are generally very close to unity in sputtering because of the high energy of the impinging particles and also at elevated temperatures. Generally, depending on the host–metal combination and the temperature, the C varies in magnitude [75]. For Teflon, C is very small even at elevated temperatures [76]. The synthesis of nanocomposites by co–

sputtering takes place between highly cohesive energy metals (Ag and Au) [77] and a low cohesive energy polymer which leads to a very low interaction between the metal atoms and the polymer matrix [72].

Since isolated metal atoms impinge on the polymer/oxide surface, various competing process might be considered to occur like the random walk of the metal atoms, diffusion into the host, metal atoms encountering each other on their diffusion path may form aggregates at the surface or in the bulk, metal atom reemission into the vacuum, nucleation and agglomeration which have to be taken into account to understand the formation of nanoparticles in the polymer/oxide matrix [72]. In both polymers and TiO_2, the formation of clusters is due to the difference in the surface energy between the metallic component and the host material [72].

2.2 Irradiation of nanocomposites

The interesting feature of the SHI beam is the deposition of localized high energy density within a confined volume, being far from thermal equilibrium. The energy lost by the ions, modifies different properties of materials. The modification of any particular property depends on the amount of energy deposited into the material by the SHIs [26, 29, 78]. SHI beamline from both HMI, Germany and IUAC, India, had been used in this work for producing modifications in various nanocomposites.

2.2.1 Swift heavy ions

Penetration of an energetic ion with any material results in loss of energy mainly by two nearly independent processes:

- Elastic collisions with the nuclei known as nuclear energy loss $(dE/dx)_n$, which dominates at an energy of about 1 keV/amu
- Inelastic collisions of the highly charged projectile ion with the atomic electrons of

the matter known as electronic energy loss $(dE/dx)_e$ which dominates at an energy of about 1 MeV/amu or more.

In inelastic collisions, the transfer of energy from the projectile to the atoms through excitation and ionization of the surrounding electrons takes place [79]. In each collision, the amount of electronic loss varies between tens of eV and a few keV per Angstrom(Å). The inelastic collision is the dominant mechanism for transfer of energy to the material for producing tracks for a SHI moving at a velocity comparable to the Bohr velocity of the electron when its value crosses a threshold value for track formation. The type and energy of the beam, electrical and thermal conductivity of the material vary the diameter and length of the track [33, 80–82].

SHI are very useful for modification of the properties of films, foils and surface of bulk solids [83]. Bombardment of solids with SHIs leads to the formation of damage zones in the material. They penetrate deep into the materials and produce long and narrow disordered zone along their trajectory. The passage of SHI induces very rapid processes which are difficult to observe during or immediately after their passage. The resulting damage, such as size, shape and structure of defects store the information about these processes. The degree of disorder can range from point defects to continuous amorphized zone (Fig. 2.3) along the ion path called latent track (damage zone created along the paths of SHIs) [84].

The passage of SHI in nanomaterials mainly produces electronic excitation of the atoms in the materials. Quantitatively, it is capable of depositing electronic excitation energy of about 1 to 10 keV/Å in the materials. Such large electronic excitation leads to various changes in materials. Due to large amount of electronic energy deposition within a confined volume, the materials go into the molten state transiently in a narrow cylindrical region. Atomic motions in the columnar regions generated by SHI transfer the electronic excitation to the displacement of lattice atoms.

The formation of track is the result of high local electronic energy deposition along the ion path and hence conditions for track formation in different materials are different because of their different properties. Two different mechanisms can be considered [85] for track formation:

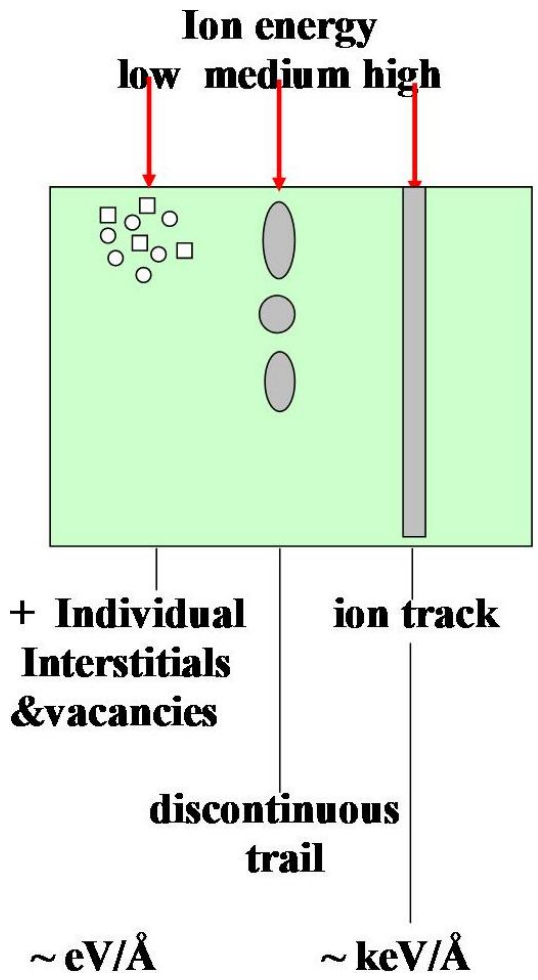

Figure 2.3: *Interaction of SHI with samples, showing the importance of selectivity for ion type and fluence.*

- Coulomb explosion model
- Thermal spike model

Coulomb explosion model is based on the assumption that the energetic ion creates a cylindrical region of highly ionized matter along its path. The charge separation corresponding to ionized species present in the cylindrical zone gives rise to a nuclear–track potential which attracts electrons and repels positively charged target ions, provided the recombination time of the electrons is long enough. Repulsive electrostatic forces (Coulomb force) act during the period before electronic neutrality is restored and give rise to a violent explosion. The Coulomb explosion is significant, if the charge neutralization time exceeds 10^{-14} s [86]. This phenomenon leads to the localized destruction of the lattice. The Coulomb explosion

model describes the condition that the Coulomb repulsive forces within the ionized region are sufficient to overcome the lattice bonding forces in terms of a local electrostatic stress being greater than the local bonding strength. Through the calculation of the stress ratio in different materials, Fleischer et al. [87] demonstrated that plastics are more sensitive to radiation than glasses, which are more sensitive than most crystals.

On the other hand, the thermal spike model uses different approaches based on transient thermal processes [88]. The target is considered as a two–component medium:

1. the electrons, which are described by the quasi–free electron gas theory and
2. the atomic lattice with known thermal properties.

During the characteristic time 10^{-13} s, the projectile ion gives its energy to the electron gas, thereby transferring the energy to the lattice through the electron–phonon coupling [89]. The electron–phonon coupling stands for the ability of electrons to transfer their energy to the lattice. The interaction between electrons and phonons originate from the phenomenon of local polarization. This is based on the assumption that when the temperature exceeds the melting point of the crystal, then a molten state is formed in a localized zone. The rapid thermal quenching of the hot region induces an amorphous track left along the ion path in a short span of time (t=10^{-11} s), with the diameter of typically few nm. The narrow cylinder of material that was heated to high temperature transiently and then rapidly quenched by thermal conduction, results in the modification/disordering of the track core. Depending on the target material, experimental observation [90,91] that only continuous tracks are formed if the energy deposition along the ion path exceeds a threshold value of electronic energy loss (S_{eth}) is known. The evolution of the track morphology depends on stopping power, proposed by Toulemonde et al. [90] and later confirmed by Meftah et al. [91]. Toulemonde et al. [90] described the necessary and sufficient conditions for formation of ion tracks in different materials.

In the modification of the functional properties of the nanocomposites by using ion beams, a desired modification of materials can be achieved by selecting a particular ion type

and its energy. This is difficult to achieve from other techniques, since the energy deposition is very much localized in this method and the process is far from equilibrium.

Hence, selective modifications can be performed in comparison to other processes like heating, where almost the whole system is modified. Controlled energy disposition with spatial selectivity is the notable feature of ion beams. Due to these interesting features, SHI have been proven to be the versatile tool for engineering materials and provide a broad range of possibilities to modify the different materials and their properties.

The loss of energy due to the passage of energetic ions through matter is mainly through collisions either with nuclei or with electrons [85, 88]. In low energy regime, the velocity of ions is relatively less when compared with the Bohr velocity of orbital electrons. Hence the incoming ions hit the target nuclei elastically and the energy is directly transferred to target nuclei resulting in displacement of target atoms. This nuclear energy loss is dominant at lower energies.

In contrast to the low energy regime, i.e., in the high energy regime the ions deposit a large amount of energy within a confined volume. Due to huge amount of electronic energy deposition, the material is in a molten state for a extremely short duration of time (a few pico–seconds), creating a cylindrical track along their path. The material modification takes place in this cylindrical track. The formation of these tracks involves a number of factors, thus modifying not only the morphological properties but also the functional properties which leads to immense interest in this field.

2.2.2 Ion–solid interaction

When energetic ions or charged particles penetrate, they lose their energy in colliding with fundamental identities, i.e., atoms of the matter. The phenomenon of interaction of ions with matter can be microscopically understood in terms of its interaction with electrons and nuclei. The collisions of ions with nuclei are elastic collisions, which results in the transfer of its energy to the target nuclei. However the collisions between charged ions and electrons of the target materials are inelastic collisions resulting in excitation and ionization of target

atoms. Both type of interaction processes, i.e., interaction of ion with nuclei and electrons result in a loss of energy ion and they are termed as nuclear energy loss (S_n) and electronic energy loss (S_e). Both, the electronic and nuclear energy losses of the ion depend on the energy of ion and are Coulombic in nature. In the case of electronic interaction, it is pure Coulombic while it is screened Coulomb potential for nuclear case. The energy ΔE, an ion loses when moving a given path is a stochastic quantity, i.e., a different ion will lose different amount of energy. The mean value of the energy loss ΔE/(Δx→0) for a large number of ions is termed the stopping power, S, which is the sum of the both energy losses and is given by:

$$S = -\frac{1}{\rho}\frac{dE}{dx} = S_e + S_n \tag{2.1}$$

where S_e and S_n are the electronic and the nuclear stopping powers respectively.

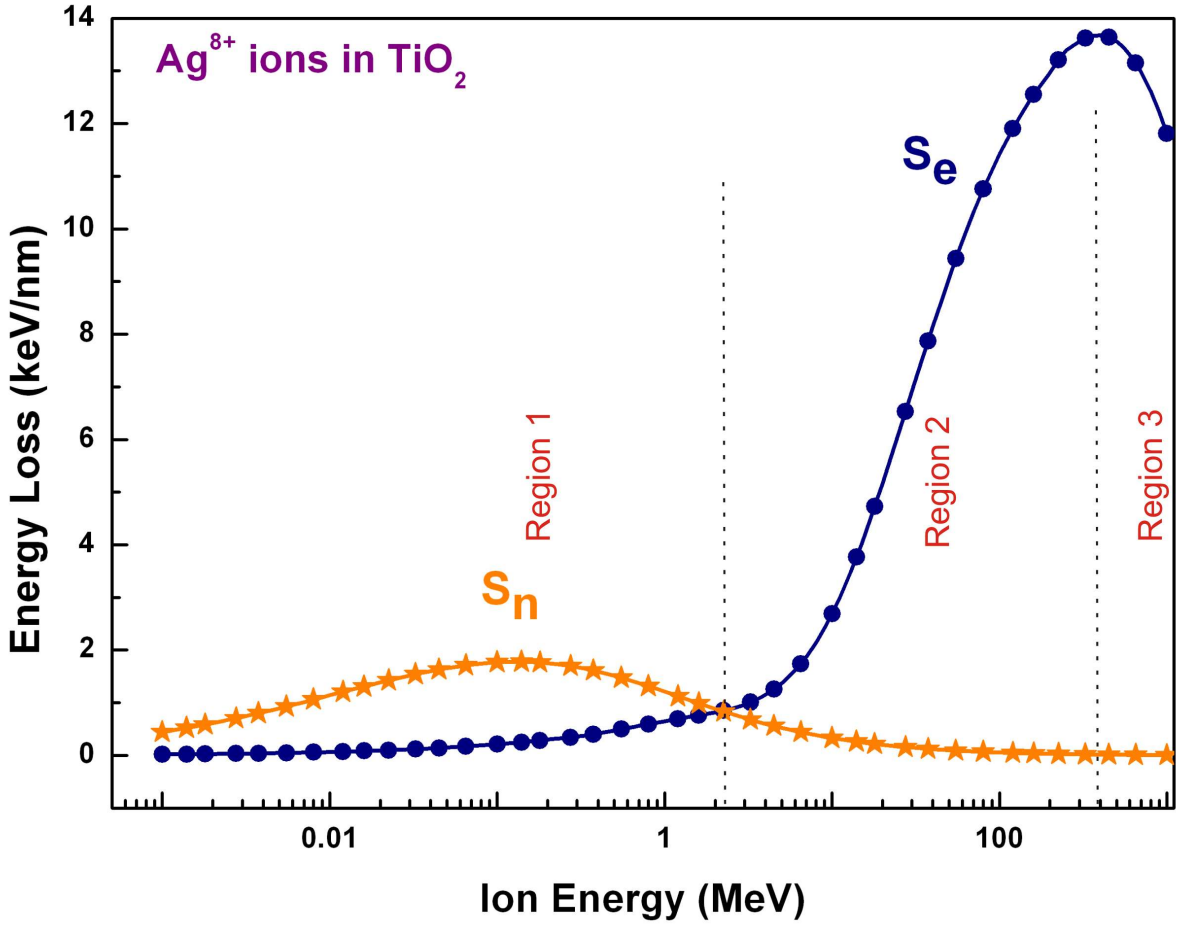

Figure 2.4: *Stopping powers (in keV/nm) for Ag–ions in TiO_2 as calculated by SRIM.*

The Stopping and Range of Ions in Matter (SRIM) is a collection of software packages which calculate many features of the transport of ions in matter. SRIM includes calculations which produces tables of stopping powers, range and straggling distributions for any ion at any energy in any elemental target [92]. The variation of energy loss of ions with the energy of the ion is shown in Fig. 2.4 simulated by SRIM. The stopping power consists of two components, (i) nuclear (region I) and (ii) electronic stopping power (region II + III). At low energies (1 keV/nucleon), the nuclear energy loss predominates. The ion collides with the target nuclei and transfers the energy and momentum to the recoil atom resulting in the displacement of atoms and the changes in the direction of the ions (elastic collision). At higher energies (1 MeV/nucleon), where the velocity of ion is comparable with the Bohr velocity of orbital electrons, the ion interacts with the electrons of the target atoms resulting in the ionization of the target atoms and/or transfer of electrons to higher states (inelastic collision). Since the mass of the ion is much higher than the mass of the electron, the initial direction of the ion in the solid remains almost unchanged.

2.2.2.1 Nuclear energy loss

The projectile ion moving with energy of the order of few keV/nucleon interacts with screened or unscreened nuclei of the target atoms. The energy loss dE of an ion by elastic nuclear interaction, in a layer dx, is proportional to the atomic density N as well as the total energy transferred in all individual collisions T_n. As can be seen in Fig. 2.4, in the higher energy regime, the contribution of S_n is insignificant.

2.2.2.2 Electronic energy loss

Projectile ions moving with very high energy and having velocity comparable to Bohr velocity of orbital electrons are called SHIs. As they pass though the matter, they lose their energy mainly through the interaction with electrons resulting in knocking of electrons from their electronic orbit leaving atom in excited/ionized state. Regions II and III illustrated in Fig. 2.4 are dominated by electronic energy loss. The difference between region II and III depends on the difference in velocities of ions passing through solid.

When velocity of ion is less than the orbital velocity of electrons ($V_I < V_O$), i.e., in region II of Fig. 2.4. In this case the ion is not fully stripped. In this case, electronic energy loss is approximately proportional to the velocity or $E^{1/2}$ of the projectile ion, where E is the elementary charge.

When velocity of ion is greater than or equal to the orbital velocity electrons ($V_I \geq V_O$), i.e., beyond the Bragg peak (region III), the ion is fully stripped. Beyond the Bragg peak, the charge state of the ion increases and finally becomes fully stripped from all its electrons and moves with a velocity greater than the average velocity of the atomic electrons in the shells of the target atoms.

In general, electronic stopping power can be divided into two regions. Firstly, the low velocity, where the projectile is only to some extent ionized and the stopping is proportional to V_I. Secondly, the high velocity, where the projectile is fully stripped, leading to the inverse square relation of velocity with stopping power.

2.2.2.3 Range of ions in solid

The projected ion range in solid is defined as the mean depth from the target surface at which the ion comes to a halt. The main parameters governing the range are the energy E_0, the atomic number Z_I of the ion and the atomic number of Z_2 of the target. The range along the path is the total distance the ion traversed along the trajectory. The energy loss phenomenon is statistical in nature as the collisions between projectile ions and target atoms are random. All ions penetrating the solid do not have the same penetration depth, but there is distribution along its path called longitudinal straggling. Since each successive collision of projectile ion with target atoms leads to deviation from its straight line path resulting in a straggling in lateral direction called lateral straggling. As SHI penetrate the matter, they lose their energy and the matter gains this energy. The projectile ions continuously lose the energy and finally stop at some place called as projected range/penetration depth. Since SHIs deposit large amount of electronic energy (a few keV/nm) within the confined volume of the material, sufficient for the material to transform into molten state, the thermal energy confined is dissipated to its surrounding by electron–phonon coupling.

2.2.3 SHI irradiation facility

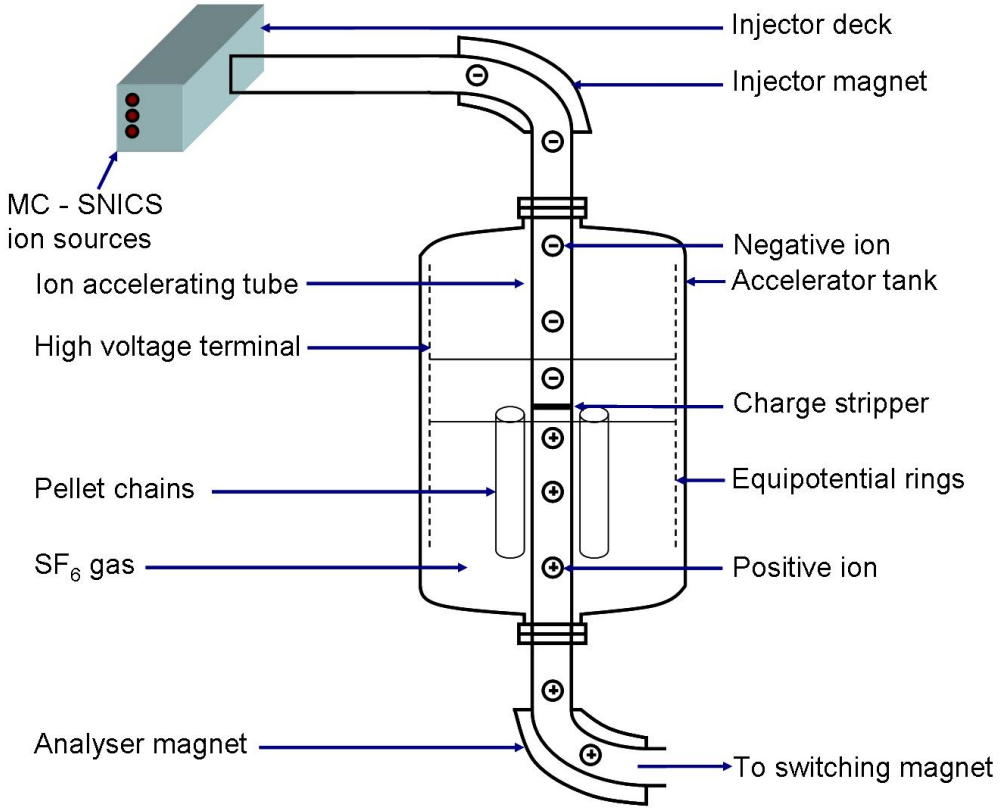

Figure 2.5: *Schematic of the 15UD Pelletron accelerator facility at IUAC.*

SHI irradiation studies of nanocomposite are currently of enormous interest, because this technology allows us to engineer the nanoscale materials within the ion tracks. The material modification can be controlled by ion beam parameters. SHI irradiation of materials can result in crystallization, amorphization, growth and dissolution, and expansion of materials along the ion track [29, 31, 78]. The Fig. 2.5 depicts the schematic of the 15UD Pelletron accelerator facility at IUAC which enables the selection of the various parameters involved for the irradiation of nanocomposites. As SHIs pass through nanocomposites, they create the nanodimensional tracks in PTFE/TiO_2 and the gold/silver nanoparticles present within these tracks go into molten state. It has been seen from thermal spike calculations that the temperature of cylindrical ion tack is larger than the melting point of nanoparticles but temperature in an annular cylindrical zone surrounding the ion track is also sufficient for nanoparticles to go into molten state.

Ion fluence, i.e., the total number of ions incident on the material per unit area is another significant parameter for modification of the materials due to SHI irradiation. The amount of energy deposited into the materials is the product of electronic stopping power and ion fluence (S_{ex}). The qualitative picture of modifications in the properties (optical, structural, electrical, magnetic, etc) of materials can be understood as a function of the product (S_{ex}). Since the size of ion tracks is of the order of few nanometers, SHI can be used as a tool for synthesis of nanostructures [93].

2.3 Noble metal particles and surface plasmon resonance

Noble metals (Cu, Ag and Au) exhibit a particularly wide range of material behavior from the bulk to atomic transition. These features become quite interesting in nanoscale region [36]. Hence a complete understanding and manipulation of size dependent physical and chemical properties of noble metal nanoparticles has become the subject of intensive research [2, 41]. The first characteristic length scale encountered in shrinking from bulk to nanoparticles is the wavelength of light. In nanocomposites,the interaction of an electromagnetic wave reveals the optical properties of these materials caused by different intrinsic and extrinsic size effects. Optical responses of large metal nanoparticles to external electromagnetic fields simply depend on their sizes, free electron density and therefore on their dielectric function relative to that of the surrounding medium [1]. This size–dependent effect is extrinsic because optical properties such as dielectric functions of the nanoparticles are similar to those of bulk metals [35]. These optical properties can be quantitatively described with Mie theory proposed in 1908 for small metallic spheres. Mie calculated the optical response of a metal sphere using Maxwell's equations under appropriate boundary conditions and observed that the optical extinction (scattering + absorption) of light from metal particles strongly depends on their size and dielectric constant of metal and surrounding matrix. When the size of nanoparticles approaches to electron mean free path (the average distance an electron travels between two successive collisions, and ∼50 nm for gold and silver), the dielectric function and refractive indices become size dependent [94]. As a result, the optical

response such as plasmon absorptions of small metal nanoparticles (R«λ) have different size dependencies compared with large nanoparticles and are called intrinsic or quantum size effect. Intrinsic size effects focuses on the question of how electronic and structural properties such as ionization potentials, binding energies, chemical reactivity, crystallographic structure, melting temperature and optical properties vary as a function of size and geometry. The associate change in spacing between the electronic energy states with variation in particle size is known as quantum size effect. The collective electronic excitations as a function of size are known as Mie resonance. Mie theory can be applied to estimate the optical response of metal particles upto quasi–static regime. Eventually, when particle size becomes comparable to the Fermi wavelength of an electron, i.e., de Broglie's wavelength of an electron at the Fermi energy or 0.5 nm for gold and silver, optical, electronic and chemical properties of metal particles are dramatically different and they behave like molecular species with discrete electronic states [35].

Propagating electromagnetic wave in the dielectric medium with incorporated spherical metal nanoparticle causes displacement of conduction electrons relative to the positively charged ionic core and the Coulomb restoring force causes for oscillation of the conducting electrons on the surface. The oscillation comprises an electromagnetic field coupled to the oscillations of conduction electrons and are called surface plasmons. The formation of a surface plasmon can be observed when the electric field of the incoming radiation induces the formation of a dipole in the nanoparticle. There is a restoring force which tries to compensate it, so that a unique resonance frequency matches this electron oscillation within the nanoparticle. They are characterized by strong field enhancement at the interface, while the electric field vector decays exponentially away from the surface (in the nm range) [95,96] as depicted in Fig. 2.6. When the dimensions of the conductor are reduced, boundary and surface effects become very dominant, and for this reason, the optical properties of small metal nanoparticles are dominated by such a collective oscillation of conduction electrons in resonance with incident electromagnetic radiation.

Many terms are used in the literature for "Localized Surface Plasmon Resonance" (LSPR), such as Particle Plasmon, Mie Resonance (valid only for spheres), Surface Plasmon

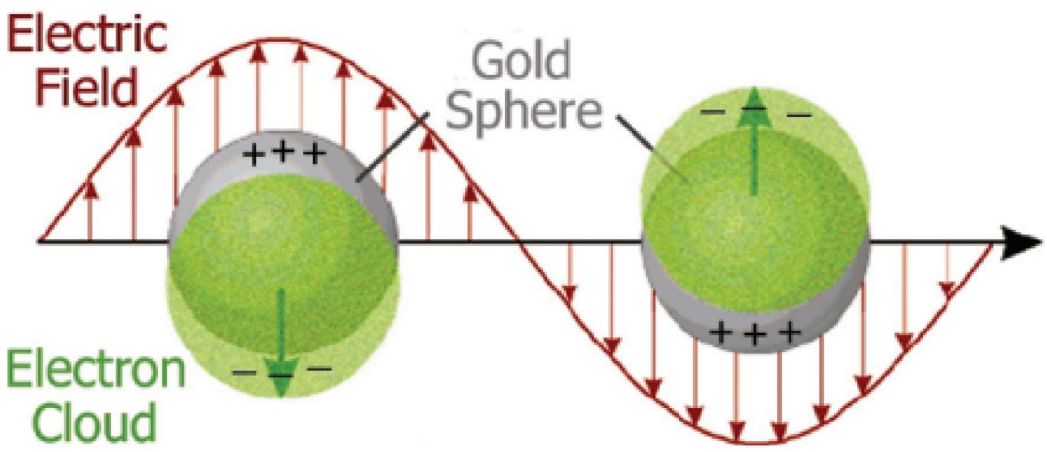

***Figure 2.6*:** *Schematic description of the electronic cloud displacements in nanoparticles under the incidence of an electromagnetic wave [1].*

Resonance SPR (most common term), Surface Plasmon–Polariton, and Localized Surface Plasmon–Polariton Resonance. Different nomenclatures exist for plasmons which might be sometimes misleading namely, (1) Volume or bulk, (2) Surface and (3) Localized, depending on the geometry of the metal under study.

The collective longitudinal oscillation of electrons that occurs within the bulk of the metal, beyond the penetration depth or skin depth of any optical field, i.e., in the order of 20 nm – 80 nm is termed as volume or bulk plasmon. Having the highest energy, these are typically measured by electron energy loss spectroscopy (EELS) using an XPS or in a TEM.

The collective longitudinal oscillations of electrons that occurs at a boundary between a metal and a dielectric are termed as SPR. A related excitation is the surface plasmon–polariton. The difference between both of them is that the polariton excitation is coupled with photons, whereas a plasmon can also be exited by electrons or other radiation.

The surface plasmon–polariton in which the excitation is localized in three dimensions is the localized plasmon. This is precisely the case with a metal nanoparticle, and it is the type of plasmon to which we will refer mostly.

Surface plasmons are collective excitations of the electrons at the interface between a conductor and an insulator. They are described by evanescent electromagnetic waves that are not necessarily located at the interface. When a particle is under the action of an

electromagnetic field, its electrons start to oscillate, transforming energy from the incident electromagnetic wave into, for example, thermal energy in an absorption process. The electrons can also be accelerated, and then, they can radiate energy in a scattering process. The attenuation by the sum of scattering and absorption of an electromagnetic wave going through a material is called the electromagnetic extinction.

Assuming non-interacting spherical particles, Mie was the first to describe the optical properties of nanoparticles quantitatively by solving the Maxwell equations for the optical response of spherical particles with arbitrary size immersed in a homogeneous medium, and subjected to a plane monochromatic wave. The dielectric function $\epsilon(\omega)$ can be written as an additive of an interband and intraband electron transitions [97].

$$\epsilon(\omega) = \epsilon_{interband}(\omega) + \epsilon_{intraband}(\omega) \tag{2.2}$$

The electron transitions from occupied to empty bands separated by an energy gap contribute to the interband contribution. The electrons are bound by restoring force given by the energy difference between ground and excited electronic states in metals, usually at the ultra violet (UV) region.

The electron transitions at the Fermi level in incompletely filled bands, or when a filled band overlaps in energy with an empty band gives rise to intraband contributions. At lower energies, these transitions also provide an absorption mechanism. The contribution due to the free conduction electrons can be described by the Drude model.

$$\epsilon_{intraband}(\omega) = 1 - \frac{{\omega_p}^2}{\omega^2 + i\Gamma\omega} \tag{2.3}$$

where ω_p is bulk plasma frequency (${\omega_p}^2 = ne^2/\epsilon_0 m_{eff}$) expressed in terms of the free electron density n,the electron charge e, the vacuum permitivity ϵ_0 and the electron effective mass m_{eff}. The damping constant Γ is related with the life time of all electron scattering processes in the bulk material that are mainly due to electron–electron, electron–phonon, electron–defect scattering. For a small particle, since the mean free path of the conduction electrons is limited by the particle boundaries, the electron-surface scattering also becomes dominant.

Modifying the value of Γ corrects the dielectric function, when the particles are not too small. The correction is complicated and results in band narrowing, band splitting, and

frequency shifts in either direction, for very small particles (R $<$ 50 Å). For particles that are not too small, Γ can be related to the particle size by the expression

$$\Gamma(R) = \Gamma_b + \frac{A\upsilon_F}{R} \tag{2.4}$$

where the bulk damping constant $\Gamma_b = \upsilon_F/l_b$ (l_b bulk mean free path of electrons), υ_F is the velocity of the electrons at the Fermi energy and A is a geometric factor that relates the appropriate electronic mean free path to the average particle radius. The expression implies that electrons in a small particle sustain scattering processes with a mean–free path of the order of radius of the particle in addition to the electronic scattering processes occurring in the bulk metal. Thus information regarding the scattering processes involved during optical excitation are embedded in this equation, thereby correlating to the width of the SPR.

As a result, well separated metallic nanoparticles are characterized by a broad, intense absorption band in the visible range of the spectrum. The bandwidth, the peak height, and the position of the absorption maxima depend on the material, size, size distribution, shape, interparticle separation, the surface state, surface coverage and the surrounding environment of the nanoparticles. The different localized plasmon resonance frequencies and strengths are related to the differences in the onset of interband transitions, e.g., Ag $\sim$4 eV, and Cu $\sim$2 eV.

The dielectric constant of the surrounding medium plays a predominant role in determining both the plasmon frequency and the intensity. The dielectric environment of the particle helps to determine the strength of the restoring force that the electrons experience. Changing the medium around the nanoparticles with a different refractive index material strongly alters the plasmon behavior of the nanoparticles. Generally, for non–absorbing surrounding, an increase in the index of refraction of the surroundings red–shifts the LSPR [98, 99]. The geometrical distribution of the nanoparticles in or on host material makes a pronouncing difference [94, 100].

Intensity, position and bandwidth are affected by the changes in the nanoparticle size. This is an intrinsic effect, which means that the variation in the size modifies the expression with the dielectric constant of the metal and thus alters the resonance condition. As there is a decrease in size on the nanoparticles, there is a blueshift in the SPR [35, 101, 102]. Both

theoretical and experimental results indicate an inverse dependence of the bandwidth due to surface scattering [103].

Shape dependence of the LSPR of nanoparticles is reported [1, 104]. Different shapes like rods, disk, squares, triangles, stars and others exhibit double to multiple resonance bands according to their shape. In the case of arbitrarily oriented nanorods, the existence of two bands, i.e., longitudinal mode and the transverse mode is the optical signature [105, 106]. In addition, the distance between the neighboring nanoparticles affects the dipole–dipole interaction between the nanoparticles thereby having a significantly affecting the surface plasmon band. The surface plasmon band broadens and shifts to higher wavelength when the inter–particle spacing becomes smaller [98, 107].

As already mentioned, Mie first provided the complete solution concerning the absorption and scattering of light by a spherical single metallic particle. Models accounting for the collective properties of metal particles in composites were developed. Maxwell–Garnett (MG) theory and the Bruggeman effective medium approximation (EMA) are widely known among them. The Maxwell Garnett geometry consists of small inclusion particles embedded in a host material and the Bruggeman geometry consists of two intermixed components. Modified theories also help to expand the applicability limits of the EMA to higher metal volume fractions.

With these theories, an effective dielectric function is calculated from the dielectric functions of both basic materials by using the MVF. The MG theory has been derived for topologically asymmetric composites, where one constituent predominates and forms a host medium (dielectric) for the small grains of the other constituent (metal) embedded in it. The EMA approach is principally based on two assumptions. Firstly, the inhomogeneities are so large that each point in the material can be associated with the macroscopic dielectric function. Secondly, the system can be described as an effective medium if the random unit region, embedded in the effective medium is not detectable in an experiment using electromagnetic radiation confined to a specified wavelength range.

Both the MG and EMA models are limited to systems with low metal or nanoparticle concentration. Also, difficulty exists in prediction of the far infrared absorption. With an

increase in the MVF, the interparticle distance becomes smaller and leads to an interaction between the nanoparticles. Hence, the EMA theory is unable to explain the experimental results obtained for higher metal volume fractions, due to the multi–polar polarizability contributions.

2.4 Antibacterial properties

Antibacterial properties of materials are of interest to mankind since ages. The basic importance of using the nanoparticles is that these nanoparticles with a larger surface–to–volume ratio provide more efficient means for antibacterial activity.

Apart from Ag, Au in a variety of forms has been used in medicine throughout the history of civilization. Over the recent decades, Au nanoparticles have attracted significant interest as a novel platform for various applications such as nanobiotechnology and biomedicine [108] because of convenient surface bioconjugation [109] with molecular probes. The early work by Robert Koch demonstrated that gold compounds were active against the tubercle bacillus [38]. Subsequent extensive work in the 1930's and 1940's demonstrated that a variety of gold compounds were active against a broad spectrum of microorganisms [110]. With regard to antibacterial activity, Williams et al. [111] showed that Au nanoparticles themselves do not affect the bacterial growth or functional activity, rather conjugates to Au nanoparticles decrease the number of growing bacterial cells.

The widespread use of silver went out of fashion with the development of modern antibiotics. Since the bacteria are unlikely to develop resistance against silver as compared to antibiotics, as silver attacks a broad range of targets in the microbes, there has been renewed interest in silver as a broad–spectrum antibacterial agent. In recent years, more and more investigations have focused on the preparation and/or functionalization of Ag nanoparticles, ranging from DNA–Ag assemblies [112] to various functionalizations [113, 114] and polymer stabilizations [115, 116].

Silver in its metallic state is inert but it reacts with the moisture in the skin or the fluid arround getting ionized which is highly reactive, as it binds to tissue proteins and brings

structural changes in the bacterial cell wall and nuclear membrane leading to cell distortion and death.

Feng et al. [117] say that the silver ions enter into the bacterial cells by penetrating through the cell wall and consequently turn the DNA into condensed form which reacts with the thiol group proteins and result in cell death. Also, the silver ions also interfere with the replication process.

Two possible mechanisms were suggested by Matsumura et al. [118]: Firstly that the bacterial cells take in silver ions which damages the bacterial cell. Secondly, the generation of reactive oxygen species through inhibition of respiratory enzymes by silver ions damages the bacterial cell itself.

Sondi et al. [119] also observed that the silver nanoparticles interact with the building elements of the bacterial membrane and cause damage to the cell. They confirmed the incorporation of silver nanoparticles into the membrane by formation of pits on the cell surface. They concluded that nanomaterials could prove to be simple, cost effective and suitable for formulation of new type of bacterial materials.

Morones et al. [120] studied the effect of different concentrations of silver on growth of bacteria and demonstrated that at a concentration above 75 μg/ml there was no significant bacterial growth. They also found the presence of silver in the cell membrane and inside the bacteria. Only individual particles were found attached to surface membranes.

Yanaka et al. [121] found that the silver ions penetrate into the bacterial cells rather than residing in the cell membrane. Their study pointed out that a ribosomal sub–unit protein and some enzymes and proteins are affected by the silver ions. Thus, they concluded that bactericidal action of silver ions is basically caused due to the interaction of silver ions with ribosome and the suppression of enzymes and proteins necessary for Adenosine triphosphate production.

The mechanism of action of silver is linked with its interaction with thiol group compounds found in the respiratory enzymes of bacterial cells. Silver binds to the bacterial cell wall and cell membrane and inhibits the respiration process. In some cases, silver acts by

inhibiting the uptake of phosphate and releasing phosphate, mannitol, succinate, proline and glutamine from bacterial cells [122]. On the other hand, the mechanism for the antimicrobial action of silver ions is not properly understood however, the effect of silver ions on bacteria can be observed by the structural and morphological changes. It is suggested that when DNA molecules are in relaxed state the replication of DNA can be effectively conducted. But when he DNA is in condensed form it loses its replication ability hence, when the silver ions penetrate inside the bacterial cell the DNA molecule turns into condensed form and loses its replication ability leading to cell death [122].

Extremely large surface area enables silver nanoparticles to show efficient antimicrobial property compared to other salts, which provides better contact with microorganisms. The nanoparticles get attached to the cell membrane and also penetrate inside the bacteria. The bacterial membrane contains sulfur–containing proteins and the silver nanoparticles interact with these proteins in the cell as well as with the phosphorus containing compounds like DNA. When silver nanoparticles enter the bacterial cell it forms a low molecular weight region in the center of the bacteria to which the bacteria conglomerates thus, protecting the DNA from the silver ions. The nanoparticles preferably attack the respiratory chain, cell division finally leading to cell death. The nanoparticles release silver ions in the bacterial cells, which enhance their bactericidal activity [117–122]. Also, it is corroborated that the bactericidal effect of silver nanoparticles is size dependent [120, 123].

Despite the various efforts towards the effective use of silver as an antibacterial agent, the exact mechanism of action of silver on the microbes/bacteria is still not known. But the possible mechanism of action of metallic silver are the silver ions and silver nanoparticles which have been suggested according to the morphological and structural changes found in the bacterial cells [122].

Different groups have tried to synthesize metal–based TiO_2 based nanocomposites physical and chemical routes to meet various demands of different applications [124–127]. Biologists, medical doctors and material scientists work towards achieving better antibacterial and antifouling nanomaterials capable of giving better properties [128]. In this thesis the antibacterial properties are assessed through the method of fluorescence microscopy and

the modified conventional disc diffusion method through the group of Prof. Dr. Podschun at the Institute for Infection Medicine. Here, the antibacterial property of silver is related to the amount of silver and the rate of silver released. Since silver ion release is a vital parameter for understanding the antibacterial activity of materials, preliminary efforts towards the measurement of silver–ion–release have been conducted through the studies using XPS and UV-Vis spectroscopy both before and after irradiation.

Chapter 3

Experimental and characterization techniques

In this chapter the experimental facilities for the synthesis of the nanocomposites, the irradiation facilities used and the various characterization techniques employed towards the analysis of the nanocomposites are discussed.

3.1 Experimental

The experimental section in this work is carried out as following (1) synthesis of the nanocomposites (2) characterization of the nanocomposites in terms of their morphology, MVF and their functional properties, (3) SHI irradiation of the nanocomposites at different fluences with respect to the MVF and (4) characterizing the irradiated nanocomposites in order to observe the changes in the properties. These facilities will be discussed in the following sections.

3.1.1 Preparation of nanocomposite thin films

Composite coatings were prepared by co–sputtering the host dielectric materials TiO_2 and PTFE and metal (silver/gold/copper) from two different magnetron sources, i.e., RF and

DC respectively in a home–made deposition chamber(Fig. 3.1). The deposition chamber was evacuated to base pressures of 10^{-7} mbar, by two different types of vacuum pumps: A rotary pump (Pfeiffer DUO 005 M) was used to generate the pre–vacuum (10^{-1} mbar) and a turbo molecular pump (Pfeiffer TMU 260) coupled to the rotary pump to create the end vacuum. Both continuous and independent monitoring of the deposition rates of the metal and dielectric material were done in–situ by using two quartz–crystal monitors. Metal was deposited by using a DC planar magnetron source ION'X 2UHV (Thin Film Consulting). A similar make RF magnetron source was used for sputtering the dielectric material copper–bonded Titanium dioxide (Williams Advanced Materials) or Teflon (home–made) to prevent charging of the target.

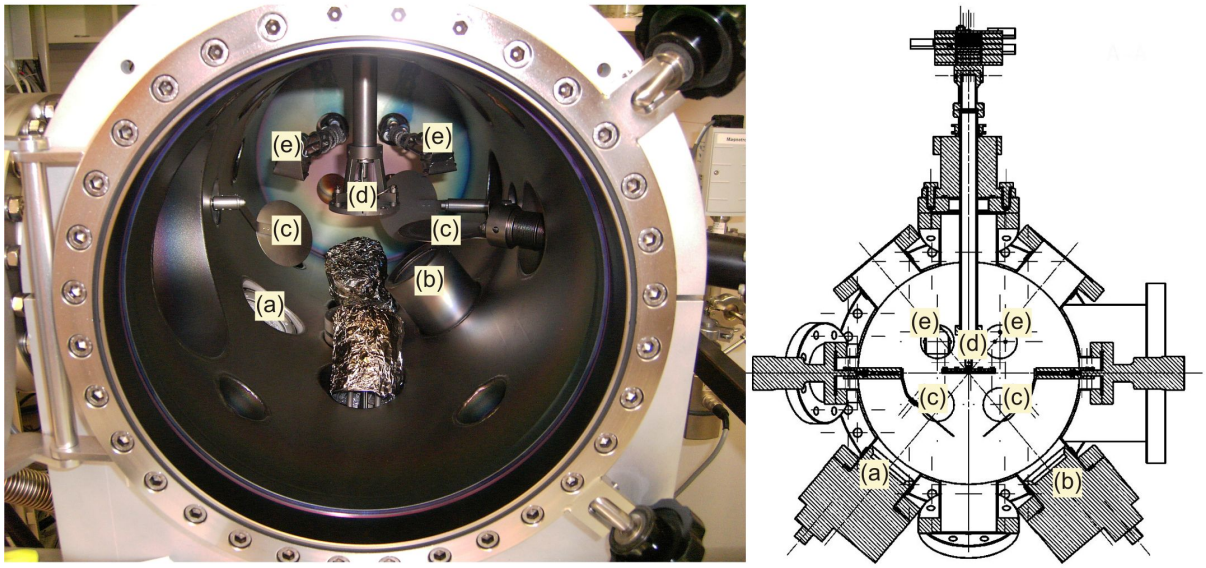

***Figure 3.1*:** *Chamber employed in this work for the deposition of nanocomposite films. (a) Metal magnetron (DC), (b) Polymer or oxide magnetron (RF), (c) Shutters, (d) Rotatable sample holder and (e) Quartz–crystal monitors*

In this work, Ag/Au/Cu and Teflon/TiO_2 targets were disks of diameter 2.05 inches. Pre–bonded TiO_2 was used to avoid thermal cracking. Generally, metal–filled epoxy cements/Indium of high thermal conductivity are employed for bonding. The deposition rate of TiO_2 could be changed between 1 – 4 nm/min by variation of the RF power, while in the case of polymer PTFE, the deposition rates were varied from 1 and 8 nm/min by varying the RF power. On the other hand, typical deposition rates between 0.5 to 3 nm/min have been

used for the deposition of Au and Ag. The deposition rate of the host and the metallic component were controlled by variation of the power applied to the magnetron sources, thereby controlling the MVF. The sample holder was rotated throughout the deposition process to achieve uniform and homogeneous deposition on all the samples mounted on the sample holder.

The thickness of the coating was measured by a surface profilometer (Dektak 8000) through the nanocomposite coating on a masked silicon wafer. Subsequently, the metal concentration was determined by using an energy dispersive X–ray spectrometer (SEM–EDX Philips XL30) which had been calibrated initially, thereby estimating the MVF. The morphology of the nanoparticles has been studied by transmission electron microscopy (Philips–CM30/Philips Tecnai F30 G^2). With the availability of a new Philips Tecnai F30 G^2, high resolution TEM and electron diffraction studies were carried out on a particular set of samples. Optical extinction studies were carried out by a UV/Vis/NIR spectrophotometer (Perkin Elmer Lambda 900). Several pieces of nanocomposite coated POM polymer pieces have been used for the bacteriostatic studies using fluorescence microscopy.

3.1.2 Irradiation of the functional nanocomposites

After the synthesis and characterization of the nanocomposites, the samples have been subjected to irradiation. Irradiation has been primarily done by using the SHIs. Despite the few possibilities of carrying out irradiation, in this work, the study has been primarily focused on the modifications in the functional properties of the nanocomposites. As shown in Fig. 3.2, at the HMI, Germany, the chamber called Biber was used for the irradiation of the nanocomposites. Samples are mounted in this chamber which is maintained under high vacuum conditions for the purpose of irradiation.

Despite the fact that the facility in Berlin could be used only for a short time, because the facility has been closed, further work has been carried out at the material science beamline facility at New–Delhi, India. The chamber that was used at IUAC India for the irradiation of nanocomposites is shown in Fig. 3.3.

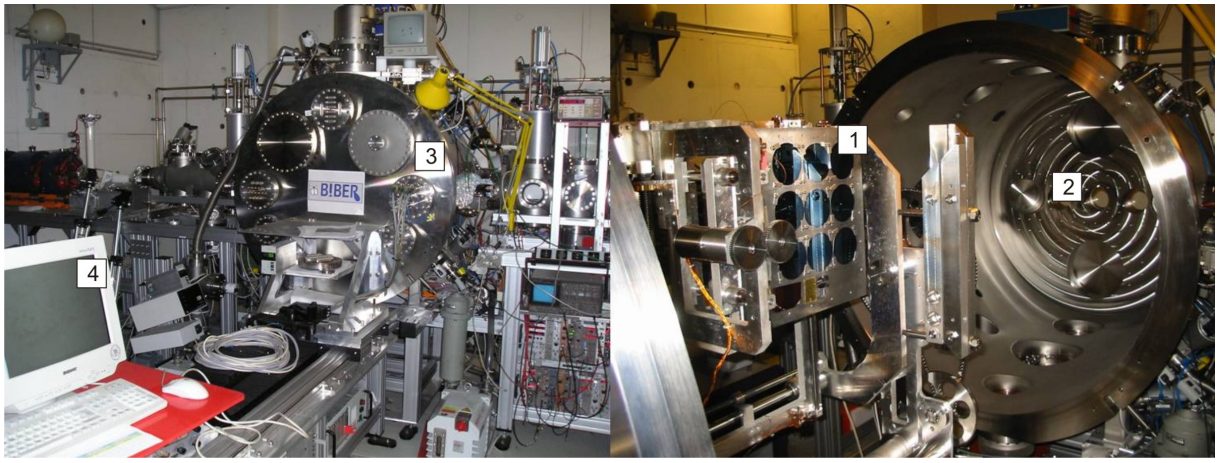

Figure 3.2: *The facility at the HMI, Germany for the irradiation of nanocomposites using SHI.*

Figure 3.3: *The facility at the IUAC, India for the modification of nanocomposites using SHI.*

At both the facilities the irradiation of the nanocomposite coatings have been carried out in chambers with high vacuum conditions (10^{-6} mbar). Also, the ion beam energy with a particular fluence was selected based on the variation of time. Computerized scanning functionality of the ion beam enabled the preprogrammed automated scanning of the entire sample surface as shown in Fig. 3.2 at 4. Nanocomposite coatings on glass, Si wafer and carbon coated Cu–TEM grid were used as samples for the irradiation. These samples were mounted on 25 cm $\times$ 25 cm sample holders at HMI. At IUAC, a rotatable sample holder capable of holding about 25 samples (1 cm^2) was used.

3.2 Characterization

3.2.1 Electron microscopy

An electron microscope is a type of microscope that uses a beam of electrons to illuminate a specimen and create a highly magnified image. Electron microscopes have much greater resolving power than light microscopes that use electromagnetic radiation and can obtain much higher magnifications, while the best light microscopes are limited to magnifications. Both electron and light microscopes have resolution limitations, imposed by the wavelength of the radiation they use. The greater resolution and magnification of the electron microscope results from the fact that the de Broglie wavelength of an electron is much smaller than that of a photon of visible light. The two types of electron microscopes which were used in this work are:

1. Scanning electron microscope **SEM XL30 (Philips)**

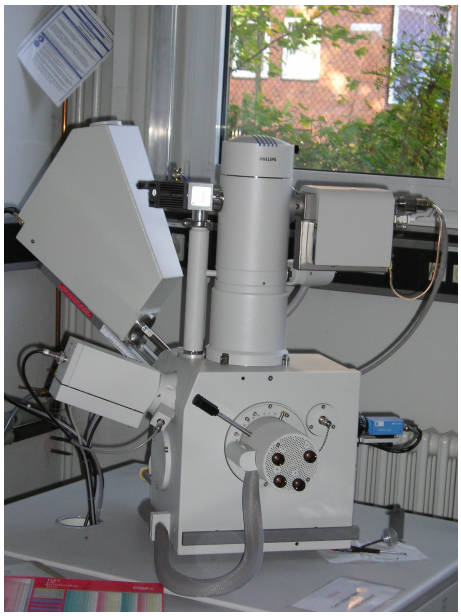

Figure 3.4: *SEM XL30 with an EDX detector used in this work towards the EDX analysis to determine the volume fraction.*

Cathode: LaB_6 – Crystal

Accelerating voltage: 1 to 30 kV

Minimum lateral resolution: about 10 nm

Maximum magnification: approximately $200,000$ times

Maximum sample size: $100 \times 100 \times 20$ mm

Detectors: Everhart–Thornley detector, Detector for X–ray microanalysis (EDAX)

2. Transmission electron microscope

   Tecnai F30G^2 (Philips)

Figure 3.5: *Tecnai F30G^2 (Philips) used in this thesis work.*

Accelerating voltage: 80 – 300 kV,

Point resolution: 0.20 nm

Line Resolution: 0.102 nm

Information Limit: 0.14 nm

Magnification range (TEM): 60 x to 5000 Kx

STEM HAADF resolution: 0.19 nm

Magnification range(STEM): 150 x to 230 Mx

Tilt angle (Double tilt): ±40°

Tilt angle (Tomography): ±70°

Detectors: Detector for X–ray analysis (EDAX), HAADF Detector

Gatan CCD camera (2k × 2k), Gatan GIF Tridem

CM 30 TEM (Philips)

***Figure 3.6*:** *TEM CM30 used in the initial stages of this thesis work.*

Accelerating voltage: 100 – 300 kV

Point resolution: 0.25 nm

Tilt angle: ±60°

Beam diameter: 2 nm

Detectors: Detector for X–ray analysis (EDAX)

Gatan CCD–Camera

A brief description of the microscopes and the methods used are discussed in the following sections.

3.2.1.1 Scanning electron microscopy (SEM)–Energy dispersive X–ray analysis (EDX)

The SEM is a type of electron microscope that images the sample surface by scanning it with a high–energy beam of electrons in a raster scan pattern. The electrons interact with the atoms that make up the sample, producing signals that contain information about the sample's surface topography, composition and other properties as shown in the Fig. 3.7.

Electron beam microanalysis is a powerful, non–destructive, X–ray spectrochemical technique capable of performing elemental analysis of micro volumes, typically of the order of a few cubic micrometers in a non–destructive way. Analysis of X–rays emitted from a sample can be accomplished by an energy dispersive spectrometer discriminating X–ray energies. As a result of the interaction between the impinging electrons and the target atoms, X–rays are emitted which are characteristic in energy for the constituent chemical elements. A histogram of the X–ray intensities versus their energy called an X–ray spectrum enables not only the identification but also the quantification of the chemical elements present in the specimen. A quantitative analysis is performed by extracting the net intensities of the different peaks present in the spectrum via background subtraction. These intensities are then corrected for detection efficiency and matrix effects and also for the absorption and fluorescence of X–rays in the specimen.

In view of the small volume involved, namely the beam–specimen interaction volume, the EDX technique is particularly suited for determining the:

- local chemical composition of inhomogeneous specimens.
- chemical composition of very small quantities of material or small particles.
- spatial concentration distribution or gradients of constituent chemical elements, either along a line or over an area.

- chemical composition of films deposited.

Some characteristic features of the SEM–EDX technique are listed below:

- Range of elements: all elements of the periodic table from beryllium onwards.
- Minimum detectable mass fraction: from 0.2 % to 1 %.
- Relative accuracy of the quantitative results lies between 2 % and 20 % depending on the correction method employed and the known chemical standards.
- Spatial resolution depends on the mean atomic number, density of the specimen and on the primary beam energy. 0.2 to 10 microns.

The interaction of the electron beam with the specimen produces a variety of signals of which the most important are the secondary electrons (SE), backscattered electrons (BSE) and X-rays as shown in the Fig. 3.7. This represents the energy lost by the incident electrons as they propagate through the specimen. The SE signal is most commonly used for imaging mode and derives its contrast primarily from the topography of the sample. These electrons are of low energy and are very easily influenced by voltage fields. The BSE signal is caused by the elastic collision of a primary beam electron with a nucleus within the sample.

Two types of radiation can be detected when the electron beam strikes the specimen, characteristic radiation and continuum radiation. For an electron to eject an inner shell electron from the atom, it must possess a minimum amount of energy. This energy is the binding energy of the particular inner shell electron, which is specific, characteristic energy for each electron in the atom. The discrete and specific energy required to excite any given X–ray line is called the "absorption edge energy" or "critical excitation energy" or "ionization energy". It is always slightly higher in energy than the corresponding X–ray emission line. From the analysis point of view one must select an acceleration voltage exceeding the absorption energy of the line intended for analysis. In practice, one exceeds the minimum energy by a factor of 2 to 3 (over voltage) to efficiently excite the X–ray line with an electron beam. In EDX, the X–rays are arranged in a spectrum by their energy and

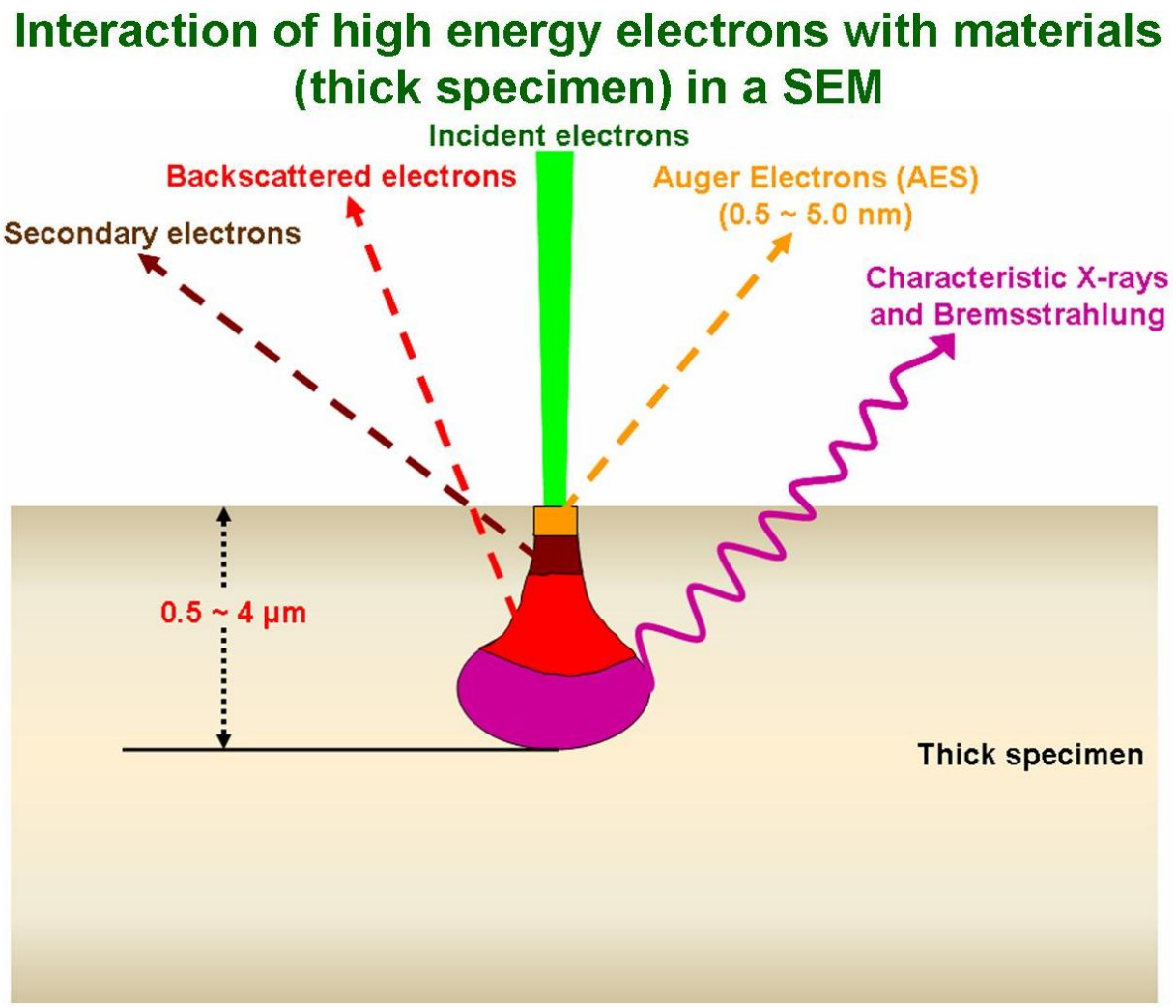

Figure 3.7: *Interaction of electrons with materials (thick specimen) in a SEM.*

from low energy to high atomic energy. The continuum X-rays are the background of the EDX spectrum and are sometimes referred as the white radiation. In theory the continuum is expected to extend from the maximum energy of the primary beam electrons and increase exponentially to zero keV energy. In reality, the background goes to zero at the low end of the energy spectrum due to the absorption by the detector window, the detector dead layer and the gold layer. The total collected X–ray spectrum consists of both characteristic and white radiation. Since the characteristic radiation carries most of the information related to the composition of the specimen, the separation of the X–ray continuum is an important step in the quantification of the elemental composition. The effect of the continuous background radiation is partly responsible for the fact that there is a non–linearity between the different

elements and the intensity of the corresponding X–ray line, resulting in decreasing peak height towards high energies.

For EDX, X–rays create pulse heights in the energy dispersive detector, which depends on the energy of the incoming X–ray. These pulses are collected by a multi channel Analyser (MCA). The detector consists of a collimator that ensures that X-rays generated from parts of the SEM column or chamber do not reach the detector. The X–ray detector is separated from the specimen by a window which is transparent to the X–rays, at the same time securing a vacuum in the region of the detector when the chamber area is vented. The detector itself consists of lithium–doped silicon coated at the front with a thin layer of Au. The X-rays produce charge pulses in the Si that are proportional to their energy and X-rays of all energies are detected virtually simultaneously. Also, because there is no focusing involved, all X-rays are detected if they occur within the solid angle subtended by the crystal.

The X–ray analysis has served as a powerful tool for understanding the composition and therby served as an effective method for the determination of the metal–volume–fraction (MVF). The ability of this technique to analyze the composition of the thin nanocomposite coating at various places has led to the determination of the MVF. This has been done by comparing it with a standard metallic film of the known comparable thickness. Thus calculating the MVF.

Determination of the local atomic concentration of metal atoms in the composite films was done by using the EDX. A uniform metal film with nearly the same thickness as the composite film was used as the standard for EDX measurement. A comparison of the relative atomic concentration of the metal between the composite films and the standard film of known thickness is used to determine the atomic concentration in the composite film. The fluorescence and adsorption contributions in this range of film thickness ($40 - 70$ nm) are very small, which was supported by the linear dependence of the metal intensities on the standard thickness. The MVF in the composite films were determined from the combination of EDX analysis and thickness measurement by profilometry [129]. The MVF in the composite can be determined from the ratio of the thickness of the metal in the composite to composite film thickness. In order to minimize the error, an average of three values have been calculated

from three representative areas on the sample and the standard exclusively prepared towards the EDX analysis on a Si substrate.

3.2.1.2 Transmission electron microscopy (TEM)

As per the sorrow expressed by Feynman in 1952 "It would be very easy to make analysis of any complicated chemical substance; all one should have to do would be to look at it and see where the atoms are. The only trouble is that the electron microscope was one hundred times poor." This really matters as better microscopes are necessary for better analysis even in the field of materials science. Philips CM30 electron microscope with a maximum acceleration energy of 300 keV was used in the initial stages to analyze the morphology of the metallic clusters. During the final stages of my work the availability of Tecnai F30 G^2 with advanced facilities has provided additional possibilities.

3.2.1.2.1 Interactions and interaction volume :

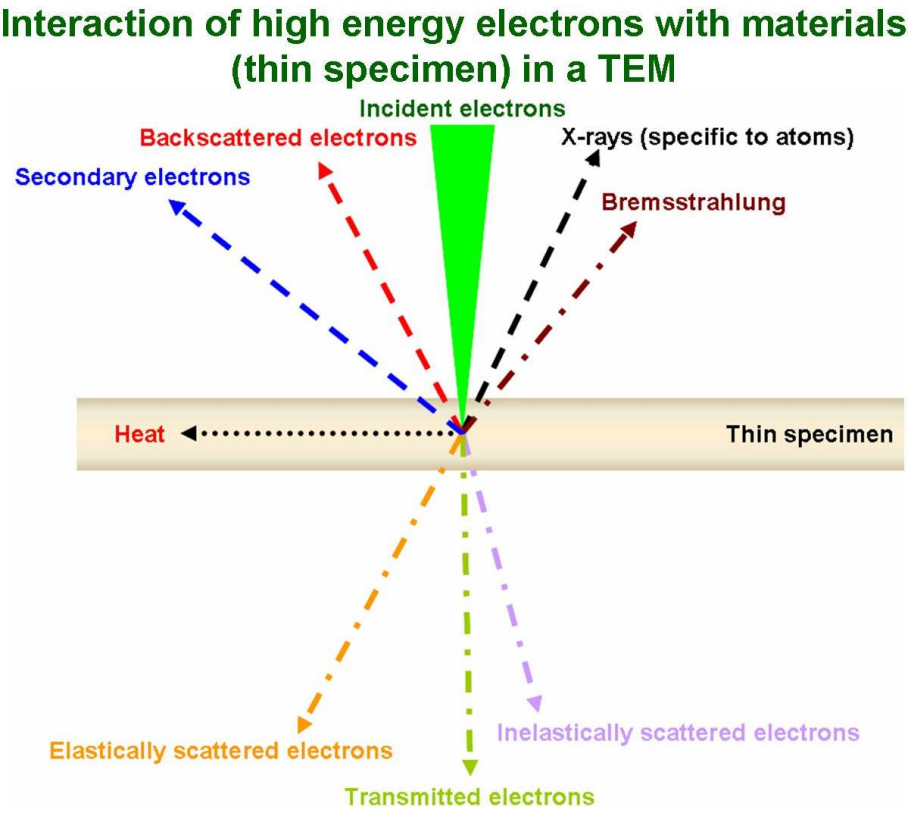

Figure 3.8: *Interaction of high energy electrons with materials (thin specimen) in a TEM.*

When electrons enter the specimen, they interact with the constituent atoms in the specimen through electrostatic forces. If electron travels close to an atom, the presence of the atomic and nuclear electrostatic potential will affect the speed and/or direction of the traveling electron. The initial velocity of the electron varies due to this interaction or the electron is scattered. If only the direction has been changed, the scattering is called elastic scattering. Elastic scattering involves Coulomb interaction with an atomic nucleus. For inelastic scattering the change of speed is involved. Inelastic scattering occurs as a result of Coulomb interaction between a fast incident electron and the atomic electrons surrounding each nucleus. In other words, the incident electron does not pass its energy to the atom during an elastic scattering process, while in inelastic scattering process, the energy exchange between the incident electron and atoms in the specimen happens. An overview of the interaction of high energy electrons with thin materials, i.e., in a TEM is shown in Fig. 3.8.

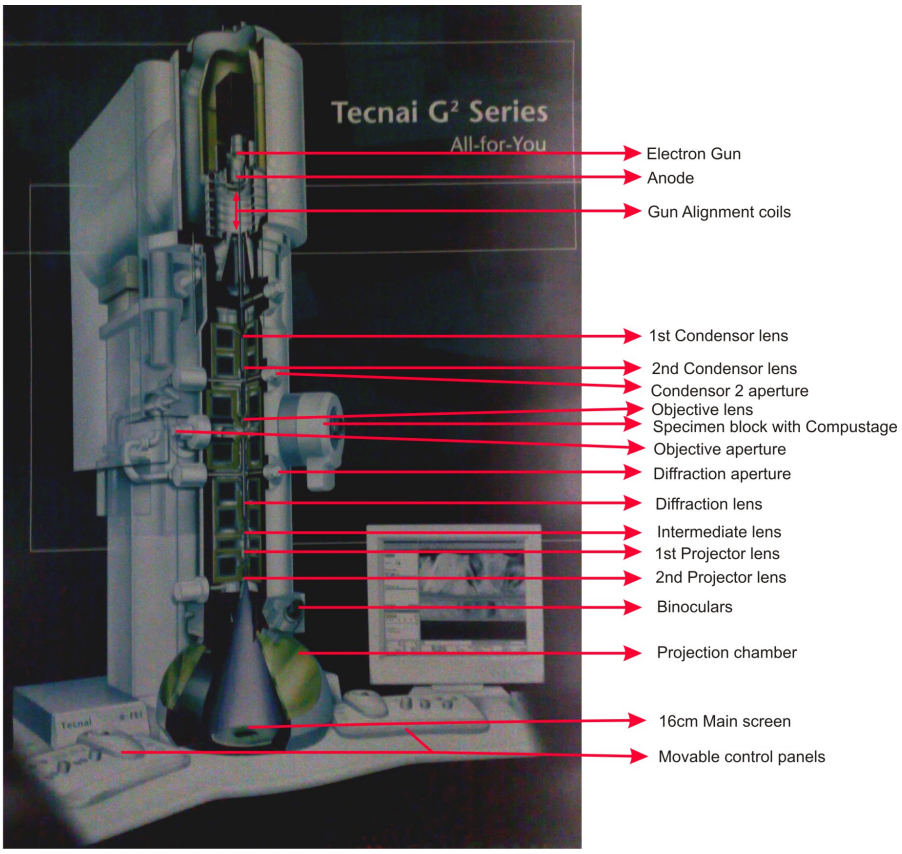

Figure 3.9: *Tecnai F30 G^2.*

The microscope consists essentially of three parts, the electron gun where the beam is generated, the lenses, deflection coils and stigmators that make the image projecting it on the screen and the projection chamber with one or more types of electron detectors to record images, diffraction patterns, etc (plate camera, TV, etc.) as can be seen from the Fig. 3.9.

3.2.1.2.2 Modes of operation :

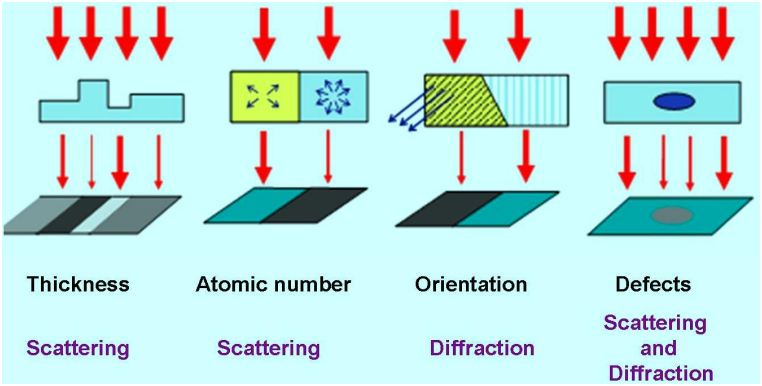

Figure 3.10: *Major factors affecting TEM image contrast.*

Thickness, atomic number, orientation and defects are the major factors which affect the contrast in the TEM images as shown in Fig. 3.10. Conventionally, image, diffraction and spectroscopy are the three general modes of operation of the TEM used in this work are as follows and are depicted in the Fig. 3.11.

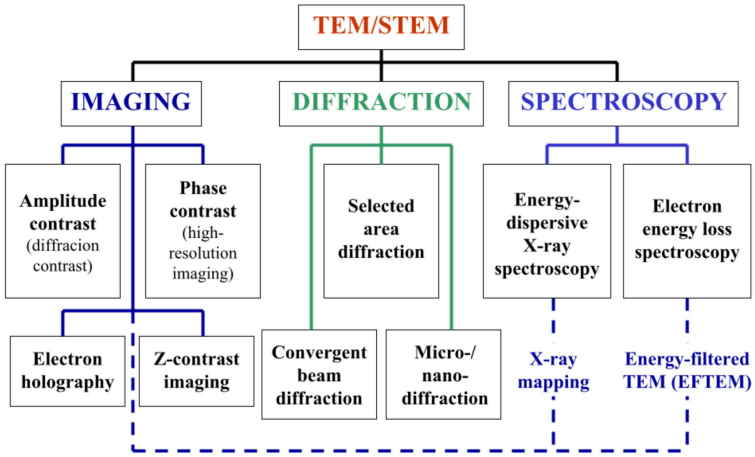

Figure 3.11: *Modes of operation of the TEM.*

The availability of a better microscope Tecnai F30 G^2 towards the end of my work had

led to better analysis procedures with associated better quality of results. The techniques capable of structural characterization on the nanometer scale on the microscope were at hand. Resolution being primarily discussed in terms of the ability of an imaging system to discriminate between two discrete objects, which is closely coupled to the wavelength of the incident illumination was enhanced.

3.2.1.2.3 Tomography :

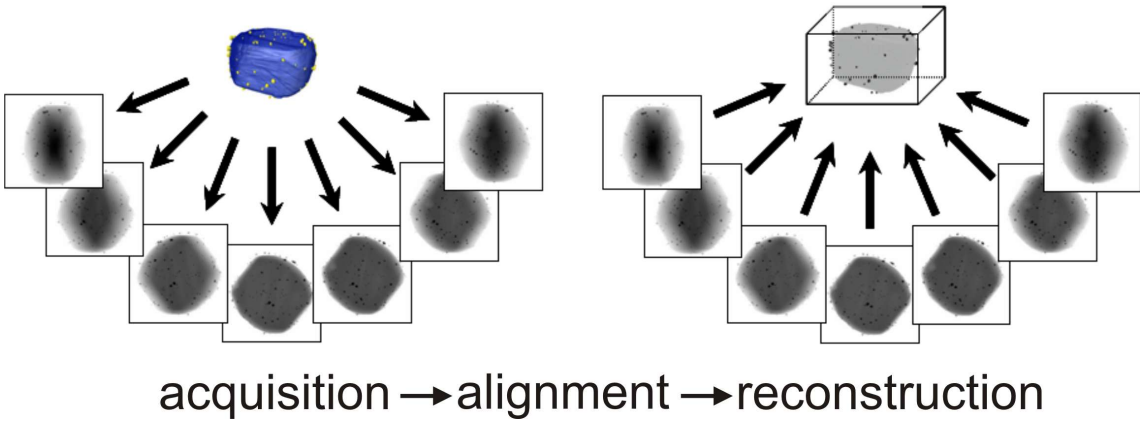

Figure 3.12: *Principle and working of three dimensional electron tomography in a TEM.*

Electron tomography allows the alignment, reconstruction and visualization of the three dimensional (3D) structure of the nanocomposite thin film from a tilt series of 2D images [130, 131]. Understanding the morphology related properties of the nanocomposites requires both two dimensional and 3D visualization of the nanocomposites. With the advancing techniques, electron tomography has been applied both in the fields of materials science and biological science to understand the location of different components in different materials. Although conventional transmission electron microscopy (CTEM) has been applied to characterize the morphology of the nanocomposites, the limit of observation by top view (CTEM) or by cross–sectional analysis methods cannot visualize the nanocomposite thin film completely. In top–view observations, despite tilting the sample, superposition leads to difficulty in assessing the morphology. On the other hand, in cross–sectional observations, either during the conventional preparation or focused ion beam method, complexity in preparing the representative section without modifying the particles through the depo-

sition of energy, generally exists. Despite considering meticulous sample preparation, the probability of cutting the nanoparticle with the surface having the smaller diameter or larger diameter is higher. Additionally, in nanocomposites all the nanoparticles are never uniformly cut. This induces falsifying scientific information. Hence tomography offers the solution. In practice, at first acquirement of a series of images through automated image acquisition at defined angles, then alignment of the acquired tilt–series, followed by the reconstruction of the aligned–series and visualization as can be seen in the Fig. 3.12.

In electron tomography, projection images of the specimen are acquired from a range of different angles by tilting the sample relative to the electron beam. Alignment followed by using a reconstruction algorithm, combines the information from the 2D projection images towards obtaining a full 3D reconstruction [132]. From the existing different iterative reconstruction algorithms [133], SIRT has been used in the present work as it is quiet suitable to produce best signal–to–noise ratio images. Despite the large number of projections, the reconstruction is affected by missing wedge artifacts due to the limited tilt range during acquisition, leading to an elongation of the particles on z–direction [132].

Amira 4.1.1 (Visage Imaging GmbH) has been used to carry out the volume rendering of the tomograms to provide a 3D impression of the overall morphology. Volume rendering is a visualization technique that gives a 3D impression of the whole data set without segmentation. The underlying model for volume rendering is based on the emission and absorption of light that pertains to every voxel of the view volume. The algorithm simulates the casting of light rays through the volume from pre–set sources which determines how much light reaches each voxel on the ray and is emitted or absorbed by the voxel. Then it computes what can be seen from the current viewing point as implied by the current placement of the volume relative to the viewing plane, simulating the casting of sight rays through the volume from the viewing point. Volume texture visualization projects the dataset at any desired angle. Hence, the morphology of the feature of interest is clearly visible [134].

Also, various imaging modes can be used for obtaining tomographic tilt series, depending on the nature of the specimen. The reconstruction computations use different iterative reconstruction algorithms [135]. Furthermore, the functional properties are sensitive to the

morphology of the nanocomposites, because the surface layers are predominantly sufficient to induce a considerable alteration in the properties. This work also emphasizes the necessity of taking into account the three–dimensional morphology of nanoparticles in nanocomposites to understand and control their functionality.

3.2.1.2.4 In–situ heating in the TEM :

In–situ microscopy refers to the techniques that allow a direct observation of the dynamic properties at nanoscale through imaging and diffraction. Thermal induced structural transformation and transition are the most traditional in–situ techniques. In–situ study of the temperature induced phase transformation, structural and compositional evolution of nanocomposites is important for understanding the structure and structural stability of the nanocomposite coatings. TEM is an ideal approach for conducting this type of experiments, in which a specimen can be heated upto 1000 °C in a Gatan double–tilt heatable sample holder with a Tantalum furnace as can be seen from the Fig. 3.13.

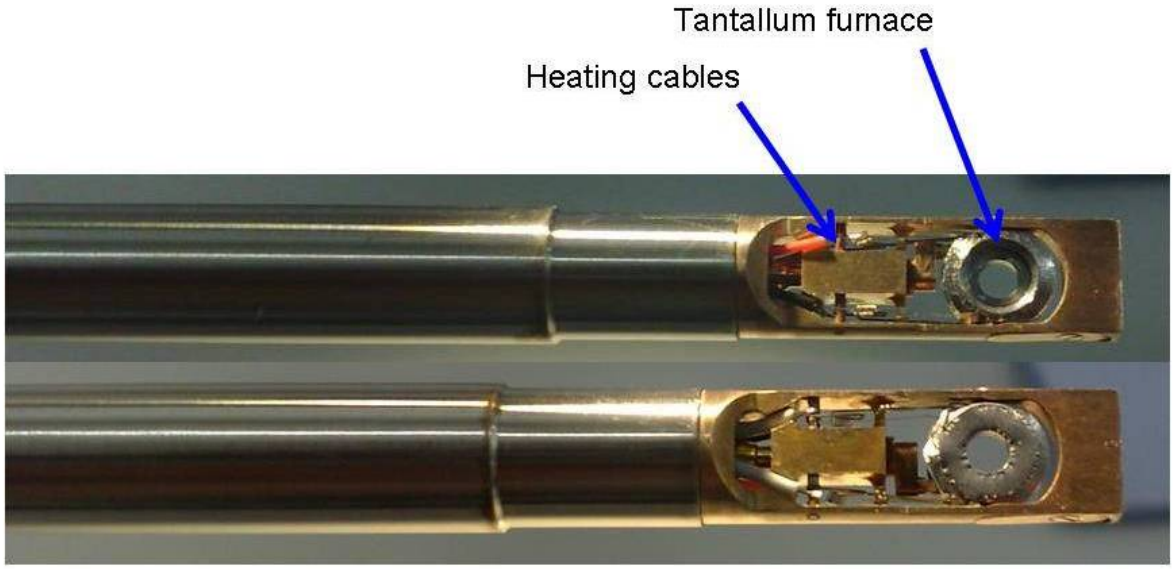

Figure 3.13: *Gatan double tilt sample holder with Ta furnace used in this work to heat the samples in the TEM.*

Due to the size, structure and composition sensitivity of nanocomposites, the morphology and the associated properties could be quite diverse. Characterizing the morphological properties of the nanocomposites depending on the thermal induced transformation under

equilibrium conditions is a study of basic importance. This aids towards a better understanding of the thermal transformations. In this work, in–situ thermal transformation of the TiO_2 based nanocomposites have been carried out. A comparative study with that of the non–equilibrium ion beam induced modification is made.

3.2.2 Ultraviolet–Visible/Near Infra Red spectroscopy

Ultraviolet, visible and near infra red (UV–Vis/NIR) spectroscopy is the measurement of the attenuation of a beam of light after it passes through a sample or after reflection from a sample surface. This UV–Vis/NIR spectroscopy technique, includes a variety of absorption, transmittance and reflectance measurements in the ultraviolet, visible and near-infrared spectral ranges. These measurements can be done at single wavelength or over an extended spectral range. The spectral range of the instruments is generally from 185 nm to 3000 nm. There is a linear relationship between absorbance and absorber, i.e., concentration, which makes UV–Vis/NIR spectroscopy especially attractive for making quantitative measurements.

A schematic diagram of the typical UV–Vis/NIR spectrophotometer is shown in the Fig. 3.14. Materials that can be characterized by UV–Vis/NIR spectroscopy include semiconductors for electronics, lasers and detectors, optically active materials, solid-state laser hosts, optical fibers, waveguides and amplifiers for communication and materials in the field of solar energy conversion. The range of the spectroscopy also spans the human visual perceptional range 400 nm to 750 nm, thus being useful in characterizing the absorption, transmission and reflectivity of a variety of technologically important materials like pigments, coatings for windows and filters. The use of UV–Vis/NIR spectroscopy in materials science research can be divided into two broad categories:

1. Quantitative measurements in the gas, liquid or solid phase

2. Characterization of optical and electronic properties of materials

Being a diagnostic tool in quantitative applications, it is often only necessary to measure

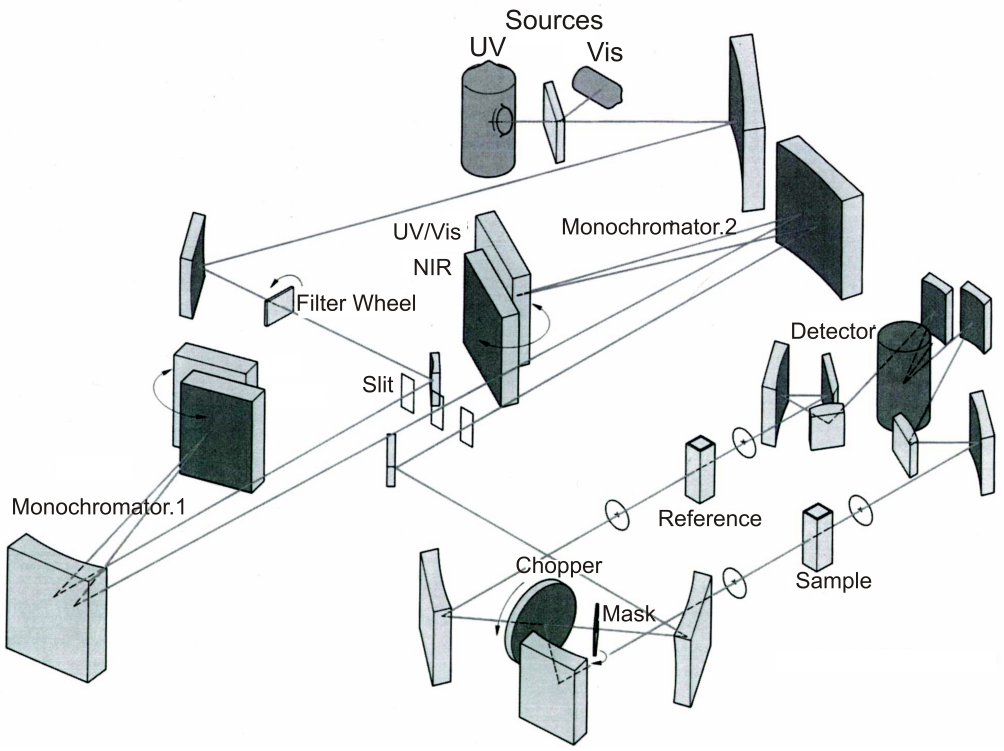

Figure 3.14: *Setup and ray diagram of the UV–Vis/NIR Spectrometer – Lambda 900 from Perkin Elmer.*

the absorbance or reflectivity at a single wavelength. Other qualitative applications require recording at least a portion of the UV–Vis/NIR spectrum for optical or electronic characterization. Since absorption of radiation corresponds to the excitation of outer electrons, UV–Vis/NIR spectroscopy also helps in estimating the bandgap of materials.

In this thesis, UV–Vis/NIR spectroscopy Lambda 900 (Perkin Elmer) has been mainly used to characterize the noble metal–dielectric nanocomposites because of their strong SPR in the visible region of electromagnetic spectrum.

3.2.3 Profilometer

The Dektak 8000 is an advanced surface texture measuring system which accurately measures surface texture and film thickness. Measurements are made electromechanically by moving the sample beneath a diamond tipped stylus. A stylus based surface profiler measures the actual physical surface of the sample. The radius of the standard diamond stylus is

12.5 microns. When using a low stylus force the stylus may tend to lift off the surface if large step is encountered at higher scan speeds.

3.2.4 X–ray photoelectron spectroscopy

X–ray photoelectron spectroscopy (XPS) is a surface analysis spectroscopic technique for determining the elemental and chemical composition of materials' surface using X–rays. XPS involves irradiation of a sample with soft X–rays and the energy analysis of emitted photoelectrons which are generated close to the sample surface. Energy is measured downwards from an assumed zero level taken at Fermi level. Normally, vacuum level should be chosen as zero level energy, but in XPS binding energies are measured with respect to the Fermi level.

XPS is a non–destructive surface analysis technique based on photoelectric effect. The photoelectric effect is the emission of electrons from a surface upon exposure to, and absorption of, electromagnetic radiation (X–rays). The electrons emitted are called as photoelectrons. The kinetic energy of the photoelectrons depends on the energy of photons expressed by the Einstein photoelectric law.
Einstein's relation $E_K = h\nu$ – BE
where BE is the Binding energy of the particular electron to the atom. The electrons ejecting from the core level identify the element by binding energy. So BE is the unique signature of the element present.

Einstein's Conservation law states that when a sample is irradiated by photons with energy $h\nu$, there is absorption of energy by an electron and ejection of photoelectron with energy E_k as can be visualized from the Fig. 3.15.

$$h\nu = E_f - E_i$$

$$E_k = h - E_b - \varphi_s$$

where,

E_k = Kinetic energy of photoelectrons outside Sample

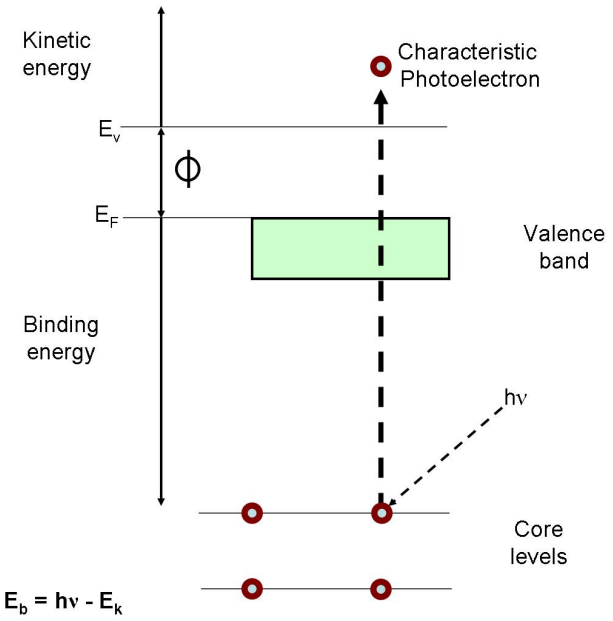

Figure 3.15: *Einstein's conversation law.*

BE = binding energy of electrons

φ_s = work function of spectrometer (compensated electronically)

Photoionization crosssection (σ), is used for the quantitative analysis of elemental concentrations

$$I_A = [A]\,\sigma_A T \lambda_A$$

$$\frac{[A]}{[B]} = \frac{I_A}{I_B}\frac{\sigma_B^*}{\sigma_A^*}\frac{\lambda_B}{\lambda_A}$$

where,

I_A Measured XPS intensity

T Energy transmission function of analyzer

λ Mean free path

$[A]$ Atomic concentration of A

From above equations relative atomic concentration can be derived. Here A and B refer to the atomic concentration of two different elements. I is the measured photoelectron peak intensity.

The Photoionization Crosssection for an element depends on

- BE – Binding Energy
- Atomic number (Z) and
- Relative direction of photon incidence and photoelectron emission (φ)

φ has a specific angle for XPS called Magic angle 54.7° (usual values 50°– 60°). The photoionization crosssection also correspond to the number of photoelectrons produced from a core level.

The analyzed photoelectrons in XPS come from the superficial layers, photoelectrons from deeper layers suffer inelastic collisions in the material. The photoelectrons ejected from the atoms very near the surface escape unscattered (i.e., suffer elastic scattering) resulting in XPS spectrum. If I_o is the flux of electrons originating at depth d then the flux emerging without being scattered I_d is given by following relation. It decreases exponentially with depth.

$I_d = I_o \exp(- d / \lambda e \sin\theta)$

where,

I_o = flux of electrons originating at depth d

I_d = flux emerging without scattering

$d/\sin\theta$= distance traveled through solid

λe= inelastic mean free path

(For Energy $100 - 1500$ eV, λe : 0.5 to 3.0 nm)

As can be seen in the Fig. 3.16, the bulk of the spectrum represents photoelectrons emerging from the surface of the sample. As the electrons suffer energy loss during their way coming out from the solid not all of the electrons ejected by X–ray can reach the analyzer. In fact due to the low inelastic mean–free path, λ_e, only electrons ejected from 0.5 nm – 2.0 nm depth below the surface can be extracted by the analyzer. This makes the XPS analysis an

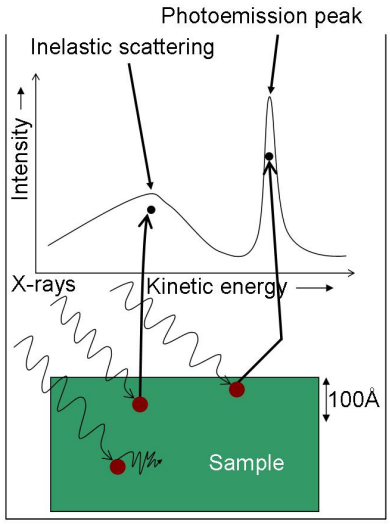

***Figure 3.16*:** *XPS spectrum contribution.*

extremely surface sensitive method. In addition the actual escape depth also depends on the direction in which they are traveling within the solid.

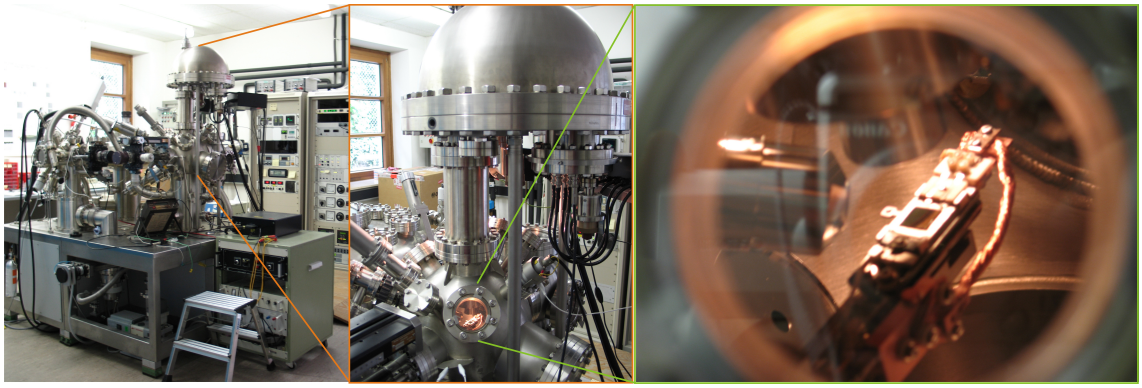

***Figure 3.17*:** *X–ray photoelectron spectroscopy (Omicron – full lab setup) used in this work towards determining the surface concentration of Silver and thereby in the silver ion release studies.*

Measurements in this thesis work were performed by XPS full lab setup from Omicron Nanotechnology GmbH (Fig. 3.17) in its ultra high vacuum analytical chamber where the pressure is usually in 10^{-9} mbar range. The analytical chamber consists of sample holder, X–ray source, and a hemispherical electron analyser (VSW EA 125), a detection system which counts the number of photoelectrons and a data acquisition and processing system. An Aluminium anode of the X–ray source (VG Microtech XR3E2) was used here.

3.2.5 Antimicrobial studies

The antimicrobial effects of nanocomposites coated surfaces were evaluated by means of two different assays:

3.2.5.1 Modified conventional disc diffusion method

Antibacterial studies using the modified conventional disc diffusion method at different MVFs required the nanocomposite coating to be deposited onto cleaned silicon 1 cm × 1 cm wafer samples – two samples per bacteria species. In other words, bactericidal activity due to silver release from the surface into the external milieu was determined. The coated surface of a prepared specimen was placed top down onto a Mueller–Hinton agar plate inoculated with the test bacteria. Ag ions, which are released at the interface between the composite film and the agar plate, diffuse continuously into the agar gel. After overnight incubation at 37 °C, a clear zone of growth inhibition around the test specimen could be observed as shown in the Fig. 3.18. The antimicrobial activity, is determined by the diameter of the growth inhibition zone. Prepared specimens were tested with reference strains of Staphylococcus aureus ATCC 6538, Staphylococcus epidermidis ATCC 155, and Bacillus megaterium ATCC 14581.

3.2.5.2 Fluorescence microscopy

For the bacteriostatic studies using fluorescence microscopy, several pieces of POM polymer cleaned in isopropanol in an ultrasonic cleaner, were mounted on the sample holder in the vacuum chamber in a separate experiment. Antimicrobial activity on the surface of coated specimen was estimated by means of direct visualization of bacterial surface growth by microscopy of test specimen after incubation with the GFP–producing strain E. coli SAR 18. Non–transparent black POM polymers coated with nanocomposites were incubated with 1×10^7 bacteria/ml in 24 well tissue culture plates. After 1 h of incubation, non–adhered bacteria were removed by washing and the test specimens were further incubated in PBS/10 % tryptic soy broth for up to 24 h. Samples of test polymers were taken at t = 0, 1 h, 6 h and 24 h,

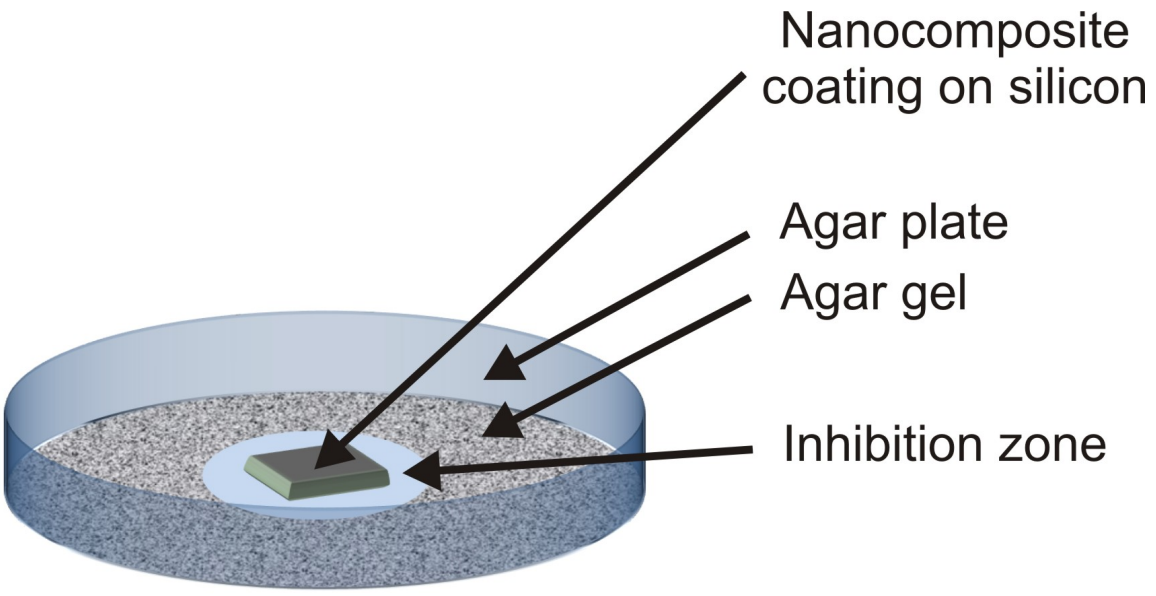

***Figure 3.18*:** *Schematic of the modified conventional disc diffusion method.*

placed onto a cover slide, and examined under a Zeiss Axioskop 2 fluorescence microscope equipped with a Canon EOS 300D digital camera at the group of Prof. Dr. Podschun.

3.2.5.3 Ag ion release

The silver based antimicrobial materials release Ag^+ ions to create a pathogenic environment in order to be effective. The oxidation of metallic silver to active species (Ag^+) is mediated through an interaction of the silver with the aqueous environment. The X–ray photoelectron spectroscopy (XPS) was used to measure the Ag^+ ion release due to the high sensitivity of XPS to small amounts of silver. The samples were immersed in 1 ml of deionized water for one day at room temperature. After that, samples were removed, blotted free of water and transferred to 1 ml of deionized water to continue the release process. Daily, 0.1 ml of the suspending fluid was removed and put on a clean Aluminium foil, where the fluid was evaporated at 160 °C. The surface concentration of Ag after fluid evaporation at 160 °C was measured by XPS.

Solutions of $AgNO_3$ with difference in molarities were used to calibrate the XPS Ag signal. The XPS signal of $AgNO_3$ solutions with defined silver ion concentration led to a calibration curve [136]. The calibration curve was obtained by plotting the XPS signal as a

function of the silver ion concentration of the standard solution [136].

An effort to study the Ag ion release was also made by using the change in the SPR of the nanocomposites through UV–Vis/NIR spectroscopy [137]. The relative change in the position of plasmon absorption maxima and peak intensities were plotted for studying the nature of silver release. All the measurements have been done after straight–line subtraction of the peaks.

Although preliminary work pertaining to the antibacterial properties has been carried out by M.Sc. A. Sbaei [136] and M.Sc. V. G. Kotnur [137] towards their masters thesis, that has not been discussed in this thesis separately.

Chapter 4

Titanium dioxide based nanocomposites

The properties of TiO_2 are promising for applications in photovoltaics, photocatalysis, photoelectrochomics and sensors [19]. Different materials have been doped into TiO_2 by different preparation methods like wet chemistry, high temperature treatment and ion implantation [19]. TiO_2 has been used in this work as it has a high refractive index, good mechanical and chemical stability, low cost and widespread availability [138, 139]. Metal nanoparticles in an amorphous matrix like TiO_2 have been studied mainly because of their optical properties, especially the nanoparticles of the noble metals like Ag [138–140] and Au [141–147]. Different groups have tried to synthesize metal incorporated TiO_2 based nanocomposites through physical and chemical routes to meet various demands of different applications [19, 124–126, 144, 148, 149].

In this work Ag–TiO_2 and Au–TiO_2 nanocomposite thin films that have been prepared by co–sputtering from two different magnetron sources in a home made vacuum deposition chamber are investigated.

4.1 Ag–TiO_2 nanocomposites

Several efforts towards the synthesis of Ag–TiO_2 based nanocomposites by various chemical methods [18, 49, 139, 148, 150–153] have been made. The control of MVF in the thin films

when they are prepared by wet chemical methods is rather difficult. In the case of sol–gel methods, the heating involved during the synthesis of the nanocomposites makes the synthesis route substrate dependent. Generally, the fabrication of optical composites is done by vacuum deposition techniques. These require an array of sophisticated equipment: a high vacuum chamber, very pure deposition materials, a means of evaporating these materials, thermal control, a mechanism for monitoring the thickness of the materials deposited and many characterization techniques [154]. The development of these nanomaterials and the devices which exploit them require effective integrated relationships from the physics and chemistry point of views.

Recent attempts for the synthesis of Ag–TiO_2 nanocomposite coatings by physical methods like reactive co-sputtering from mosaic targets have been made [155, 156]. Mosaic targets generally have the problem of nearly fixed concentrations either by using pieces [157], discs [139] or wires [155] of Ag on the TiO_2 targets. Apart from this problem, the re–sputtering effect causes a variation in the concentration of the nanocomposites with an associated difficulty in reproducing the results. Despite the possibility to tune the properties of the Ag–TiO_2 nanocomposites, the ability to tune the MVF is rather difficult when using this type of deposition [158]. Efforts towards the preparation of nanocomposite thin films by using reactive co–sputtering the nanocomposite films were also carried out. Difficulties existed in maintaining the stoichiometry of TiO_2, during the the preparation of nanocomposite thin films of TiO_2 by using reactive co–sputtering. Hence magnetron sputtering directly from the targets of TiO_2 was preferred and employed in this work.

4.1.1 Morphology

Nanoparticles are important for nanocomposite thin film applications like optical and antibacterial coatings. The morphology of the nanocomposites plays a pivotal role in determining the functional properties of the nanocomposite thin films. However, the use of nanocomposite coatings requires further study of possible size effects on their properties. The morphology of the nanoparticles has been studied by using transmission electron microscopy (Philips Tecnai F 30 G^2). HRTEM and electron diffraction studies were carried out.

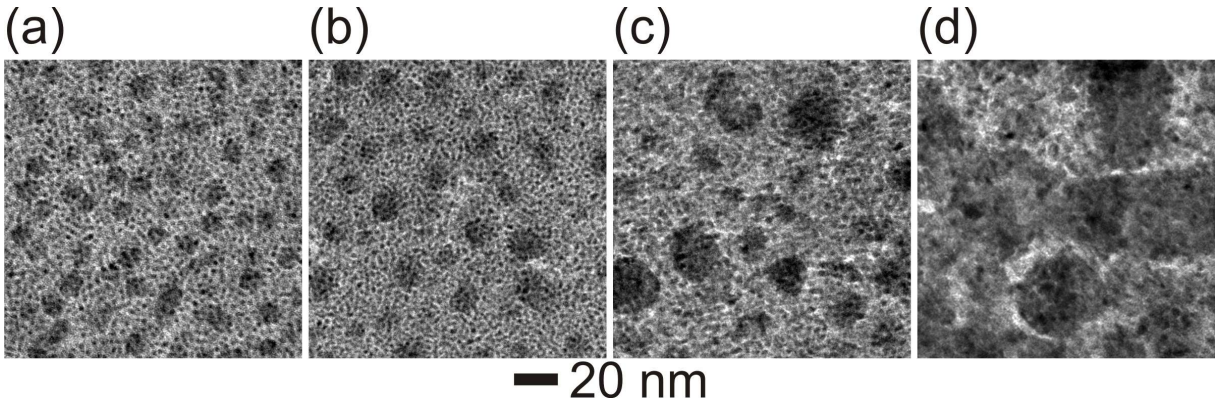

***Figure 4.1**: Transmission electron microscopy images of Ag–TiO_2 nanocomposites with MVFs of (a)15 % (b)26 % (c)34 % and (d)47 %.*

In this work, the formation of metallic nanoparticles upon vapor phase co–sputtering of Ag and TiO_2 can be understood in terms of the high cohesive energy of the silver and the low silver–matrix interaction energy. This leads to high silver atom mobility on the growing nanocomposite surface and silver aggregation whenever silver atoms encounter each other or a silver cluster. When energetic Ag atoms impinge on the TiO_2 surface, which is growing simultaneously, the arriving metal atoms undergo various processes, like random walk on the TiO_2 surface, diffusion on the growing nanocomposite film, metal atoms encountering each other within the diffusion path [159]. In the bright field TEM images of Fig. 4.1 the Ag nanoparticles appear with darker contrast in the bright TiO_2 matrix. The changes in the MVF can be seen from the TEM micrographs in Fig. 4.1, with the MVF variation from 15 % to 47 % Ag in the Ag–TiO_2 nanocomposites. On observation of the Fig. 4.2(a), two different sizes of nanoparticles can be noticed. The small particles are more clearly evident in the HRTEM micrograph of Fig. 4.2(b), which also show the nanocrystalline nature of the Ag nanoparticles from their lattice fringes. The small nanoparticles have a particle diameter between 1–2 nm and a mean distance of 4–5 nm from one another. The corresponding electron diffraction pattern in Fig. 4.2(c) also shows that Ag particles are crystalline as evidenced by the rings with diffuse intensity representing the various Miller planes. Based on the SAED patterns, the d–spacings of the diffraction rings are determined to be 0.242, 0.207, 0.147 and 0.125 nm, and can be indexed as (111), (200), (220) and (311) reflections, respectively. Pure TiO_2 [74] and Ag–TiO_2 [139] films prepared under similar room temper-

ature conditions have an amorphous TiO_2 matrix. The explanation for the formation of the larger Ag particles would be an artifact of the sequence of switching off the sputter sources (Ag source after the matrix source), which was clearly ruled out in this case. Additionally, freshly prepared samples were considered for investigation to rule out the possibility of a bimodal particle size by aging of the nanocomposite thin films through Ostwald ripening. So far it has never been reported that metal clusters existing on a polymer prepared by co–sputtering lead to bimodal size distribution by surface segregation [11]. Even embedding of clusters deposited on the surface was seen upon annealing above the surface glass transition temperature [160]. Bimodal particle size distribution has been previously reported in oxide matrices like TiO_2 and SiO_2 and also diamond–like–carbon attributing the observation to diffusion [139, 161–165], but less importance has been given towards the position of the nanoparticles in the nanocomposite.

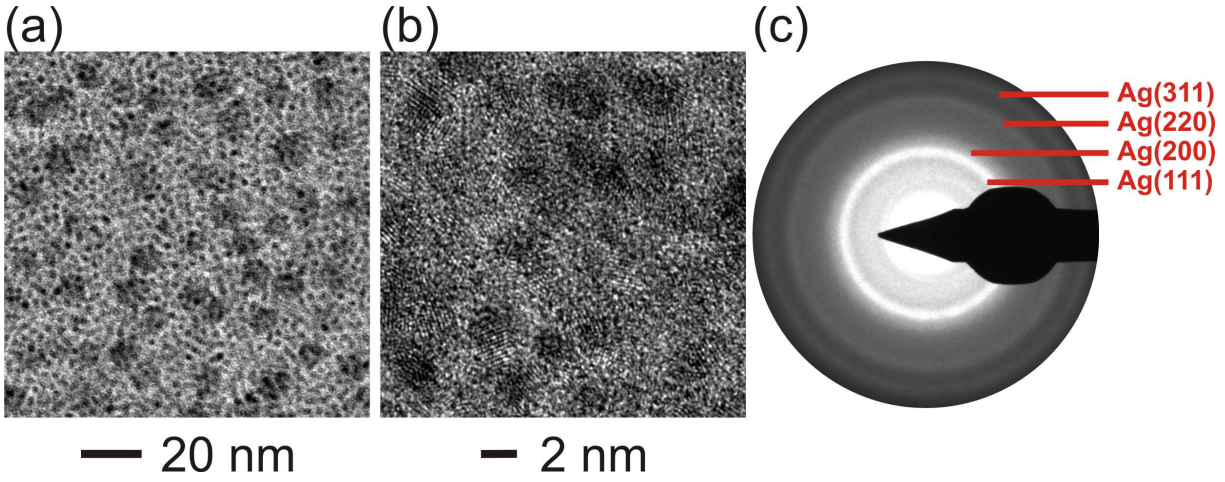

Figure 4.2: *Transmission electron microscopy images of Ag–TiO_2 nanocomposites with SAED of the 15 % Ag–TiO_2 nanocomposite showing the crystalline nature of the Ag through the rings with varying intensity, representing the various Miller planes and the HRTEM image of the 15 % Ag–TiO_2 nanocomposite with bimodal distribution clearly showing the lattice planes of the Ag nanoparticles.*

Unlike the nanocolumns with a mean diameter of 20 nm as reported by Dakka et al. [139] from the mosaic targets, nearly uniform distribution of Ag nanoparticles in the TiO_2 matrix has been observed. In this case, as the process of co–sputtering takes place from two different magnetron sources simultaneously, there exists an advantage to vary the

deposition rate of Ag and TiO_2, thus being able to tune the MVF. On varying the MVF from 13 % to 47 %, there is an increase in the nanoparticle size with an associated decrease in the interparticle distance [159]. Additionally, the silver is finely dispersed as nanoparticles, thus saving additional material compared to the bulk Ag, considering the large effective surface area for functionality.

Generally, changes in the MVF can be observed from the TEM micrographs in the Ag–TiO_2 nanocomposites [159]. Individual TEM images are generally 2D, which limit their usage for understanding the 3D structure of nanomaterials. The solution to this problem is the analysis through the state–of–art technique of 3D electron tomography. Understanding the morphology related properties of the nanocomposites requires both 2D and 3D visualization [166, 167] of the nanocomposites [132, 135, 168, 169].

Ag–TiO_2 and Au–TiO_2 nanocomposite thin films which have been prepared by using the process of co–sputtering from two different magnetron sources have been studied by using this technique of electron tomography. Tomography was performed on the functional nanocomposite thin films with Ag nanoparticles in a TiO_2 matrix with a GIF Tridiem Camera (2k $\times$ 2k pixels). The image contrast was improved by energy filtering (Zero loss peak, ZLP) [170] using a slit width of 20 eV. The tilt–series data set have been acquired with 281 images by using a tomography holder from Fischione instruments and the Inspect 3D software. Small tilt steps of 0.5° and from +70° to −70° have been used to get a high resolution. No evidence of beam damage was observed in the specimen during the acquisition of the tilt series. A movie of the volume and surface rendered tomograms can be viewed in the supporting information provided on the compact disc.

Alignment and reconstruction of the data were carried out using the software IMOD [171] by a combination of cross–correlation and marker tracking. Reconstruction was performed by 25 iterations of the Simultaneous Iterative Reconstruction Technique (SIRT) algorithm [135] implemented in Explore3D.

Keeping in mind the associated drawbacks of cross–sectional TEM (section 3.2.1.2), the necessity of having information from the third dimension becomes rather pivotal in the present case of thin films with a high nanoparticles density. The different volume rendered

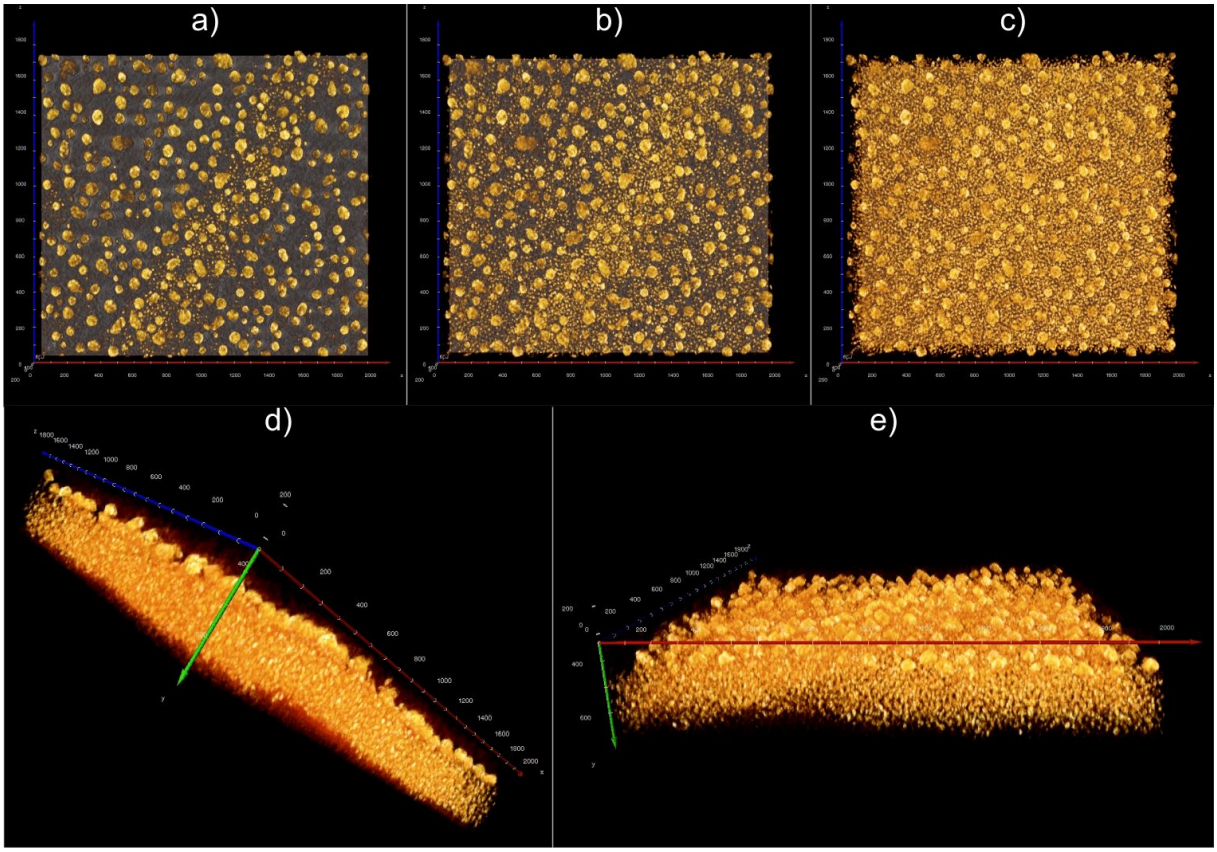

Figure 4.3: *Volume rendering of the Ag–TiO_2 nanocomposite: (a) to (c) 1/3 and 2/3 sections and the full thickness of the film seen in the XY–plane (d) and (e): Different orientations of the nanocomposite film showing the larger nanoparticles on the top surface and the smaller clusters inside the matrix of the nanocomposite film.*

views depicted in Fig. 4.3(a – e) clearly provide evidence for large metallic nanoparticles with a diameter of $\sim$ 7 nm, which are located on the surface and for smaller nanoparticles with a diameter of $\sim$ 2 nm, which are fully embedded in the matrix. Figs. 4.3(a – c) shows volume renderings of a part of the samples starting from the surface up to the full film thickness. Figs. 4.3(d – e) shows the nanocomposite film on tilting it to views where the larger particles on the top surface. Note, that such imaging by CTEM would be rather difficult (section 3.2.1.2). The surface–rendered tomograms are provided on the compact disc. Comparing the results from the 3D electron tomography and the CTEM (Fig. 4.2) the morphology of the nanocomposite thin film can be unambiguously visualized in the former case. Fig. 4.3(c) shows a volume rendered projection in the XY–plane of the whole nanocomposite from the 3D electron tomography, which is similar to that of the view obtained in the

CTEM images.

The 3D images of the two tilted views in Fig. 4.3 clearly show that the larger metallic nanoparticles are on the top surface. On the other hand, the smaller nanoparticles are embedded in the matrix. Additionally, when analyzing only CTEM images, the MVF cannot be estimated correctly. Different non–polymer matrix based nanocomposites have shown distinct particle sizes [139, 161–165]. In most cases, neither importance nor detailed discussions towards the size distribution has been provided. In the present case, it is possible that the large nanoparticles result from diffusion of metal from smaller nanoparticles that are present in the film as will be discussed in the following sections.

The morphology of the nanocomposite thin film can be explained by a two step model. The first step involves formation of small nanoparticles during vacuum phase deposition in flight or on the growing surface. In the second step after the deposition process, the larger particles are formed through particle coarsening by Ostwald ripening [172] (A) and surface segregation (B) cf. Fig. 4.4(a). Differences in the chemical potential are inversely related to the radius of the nanoparticle and are the driving force for Ostwald ripening. This can also be observed in the reconstruction slice in Fig. 4.4(b) where on the surface no smaller nanoparticles are seen between the larger nanoparticles. Additionally, segregation can also be seen in the reconstruction slice of Fig. 4.4(b) where, beneath the larger nanoparticles, hardly any smaller nanoparticles can be seen in the depletion zone. Thus this model would explain the bimodal distribution for the present case. Additional proof for this theory comes from the results of the work as discussed in [159] along with Mr. Tomislav Hrkac, who deposited a TiO_2 cover layer on the top of the Ag–TiO_2 nanocomposite. Here, no Ag nanoparticles are on the surface and thus having no local higher diffusivity leading to the formation of larger nanoparticles.

The larger particles are formed on the surface of the nanocomposite through the mechanism discussed above. At higher MVFs, similar to the percolation of the smaller nanoparticles in the matrix, the percolation of the larger particles also takes place on the surface. As the contrast of the larger nanoparticles becomes dominant at higher filling fractions, difficulty exists to study the morphology of the nanocomposite thin film even through electron

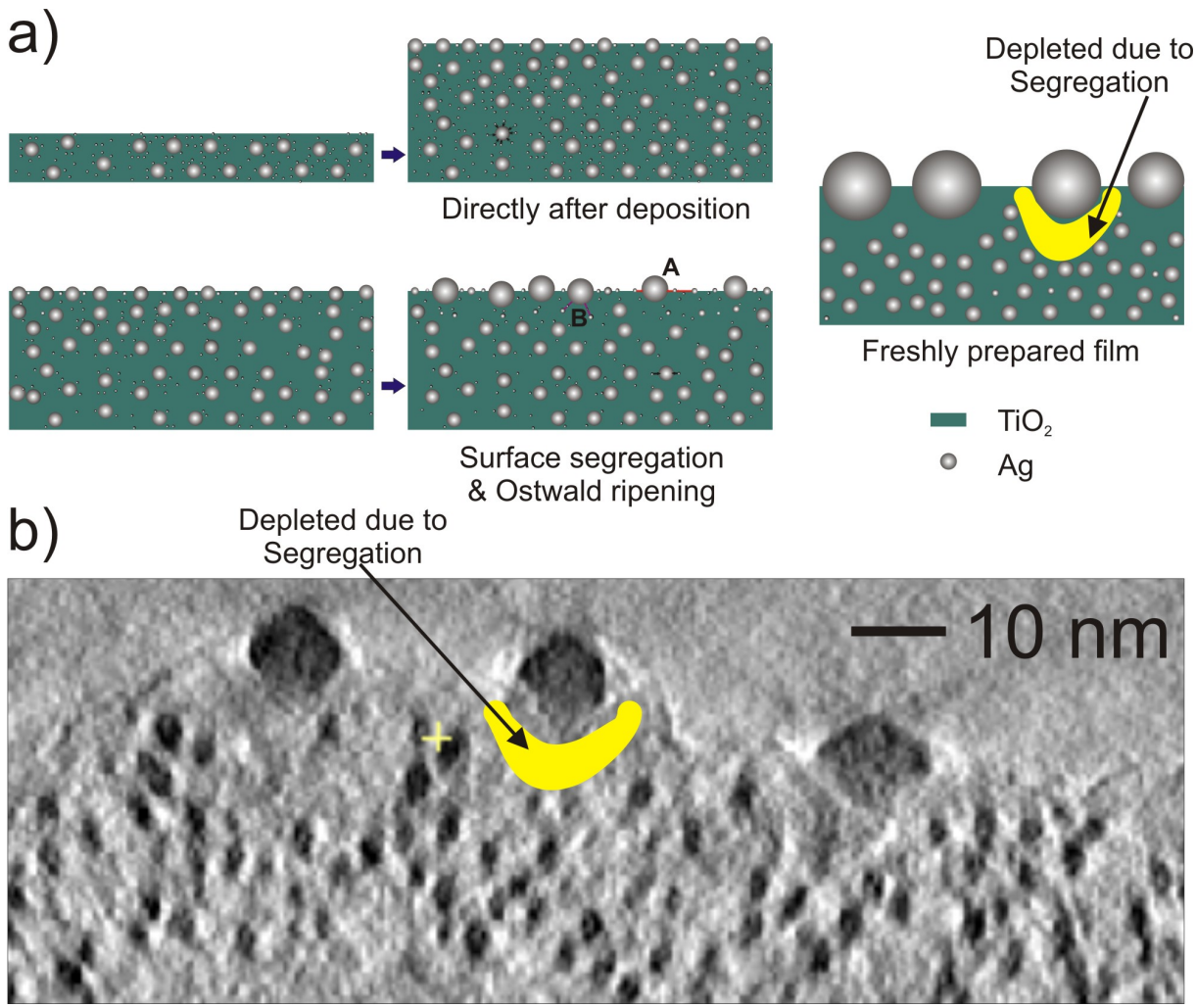

Figure 4.4: *(a) Model showing the two step process involved in the formation of nanocomposite thin films with bimodal particle size distribution. Region "A" shows the Ostwald ripening and "B" depicts surface segregation. (b) Electron tomographic reconstruction slice showing the larger nanoparticles and smaller nanoparticles and also depicts clearly the area around the larger nanoparticles to be nearly free from smaller nanoparticles.*

tomography, thus leading to the falsifying conclusions. In conclusion, tomography is a very useful technique to study the morphology of nanocomposites and thereby to understand the growth of nanoparticles. Due to the fact that this is a very sophisticated method it requires an in–depth knowledge of the process parameters and can accordingly be rather time–consuming.

4.1.2 SHI irradiation

4.1.2.1 Changes in the particle size

On irradiation with 100 MeV Ag^{8+} ions at various fluences of 1×10^{12}, 3×10^{12} and 1×10^{13} ions/cm^2, changes in the nanocomposite morphologies like the associated growth of the nanoparticles have been observed. These changes in the particle morphologies after irradiation at different fluences can be seen in the nanocomposites with 13 %, 15 % and 17 % Ag. In all the studied MVFs, similar phenomena have been observed. To avoid redundancy, only the 15 % MVF are shown here.

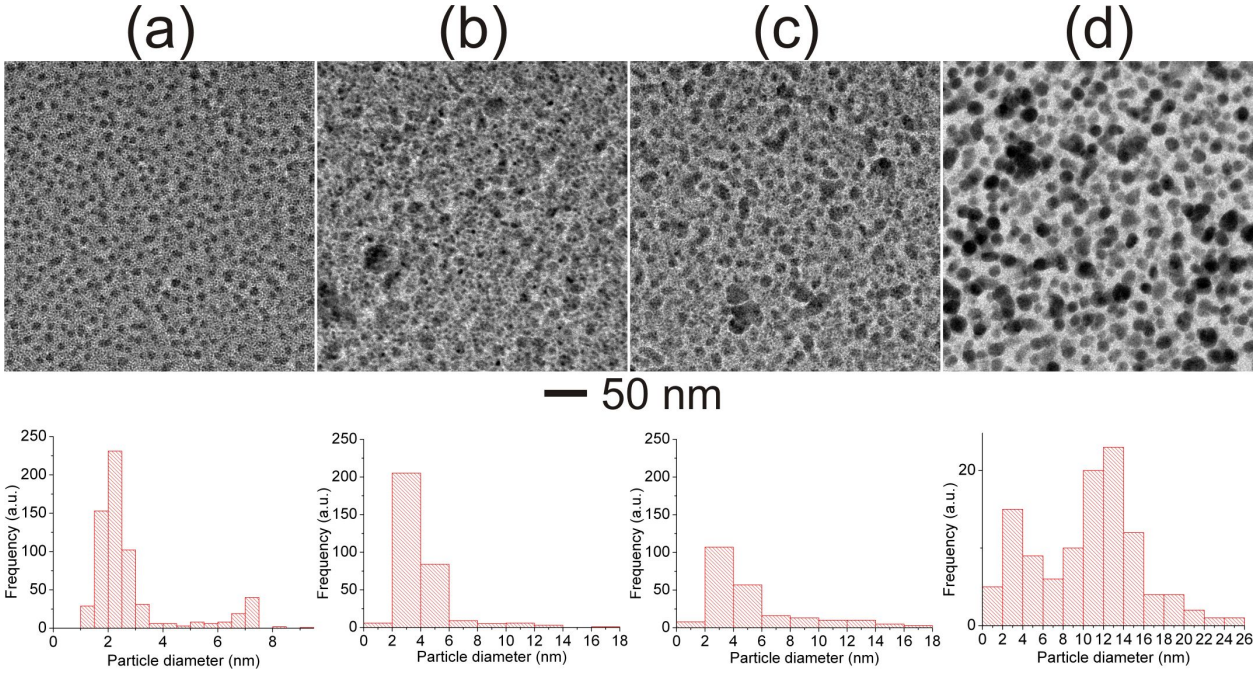

Figure 4.5: *TEM images and the respective particle size distributions of the 15 % Ag–TiO_2 nanocomposite (a) in pristine state and after irradiation at fluences (b)* 1×10^{12}*, (c)* 3×10^{12} *and (d)* 1×10^{13} *ions/cm^2.*

Particle size distributions were calculated by drawing lines across the smallest diameter of the nanoparticles from the representative TEM images with same area. In Fig. 4.5(b), at the fluence of 1×10^{12} ions/cm^2, there is an increase in the particle size compared to the smaller nanoparticles in the pristine sample (Fig. 4.5(b)) through the process of nucleation and growth. This is also accompanied by the reduction in the number of nanoparticles. At

even higher fluence of 3×10^{12} and 1×10^{13} ions/cm^2, there is growth of larger nanoparticles in cost of the smaller ones where particle coarsening is observed. Nearly uniform nanoparticles with diameter $\sim$ 12 nm have been formed with an associated decrease in the number of nanoparticles (from the particle size distribution) for the highest ion fluence (Fig. 4.5(d)). This decrease is due to the phenomenon of dissolution and re–precipitation. Nanoparticle synthesis using physical vapor deposition originally results in the formation of nanoparticles with a bimodal particle size distribution as discussed in Fig. 4.3. This depends on the MVF. For a particular metal fraction, the obtained size of nanoparticles is fixed. At this metal fraction, the size of nanoparticles remains fixed and can further be enlarged by heat treatment. This indicates a possibility to increase the nanoparticle size by ion fluence from 100 MeV Ag^{8+} SHI beam.

4.1.2.2 Changes in the matrix

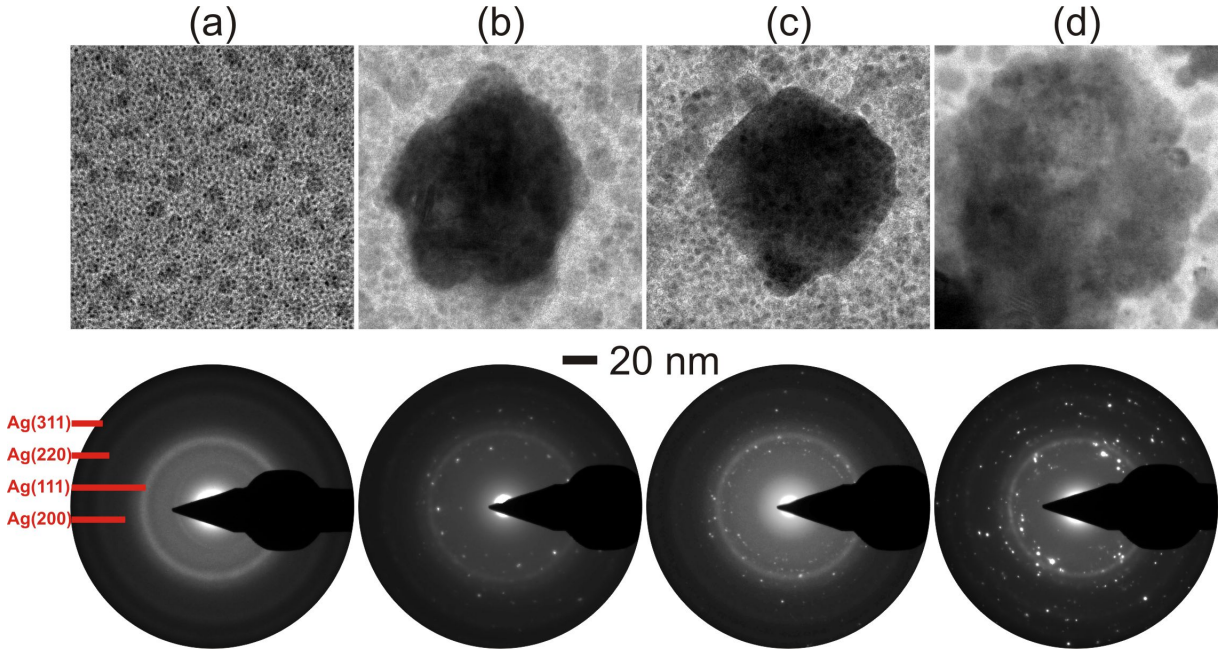

Figure 4.6: *TEM images with the associated SAED patterns of the 15 % Ag–TiO_2 nanocomposite (a) before and after irradiation at different fluences of (b)* 1×10^{12}*, (c)* 3×10^{12} *and (d)* 1×10^{13} *ions/cm^2 showing the changes in the matrix.*

On irradiation with 100 MeV Ag^{8+} ion beam at various fluences of 1×10^{12}, 3×10^{12} and 1×10^{13} ions/cm^2 changes in the particle morphologies have been observed. In this

section, investigations for the modification of the matrix are reported.

Transmission electron microscopy investigation of pristine Ag–TiO_2 nanocomposite system, clearly confirm the amorphous nature of TiO_2 matrix with Ag nanoparticles in the crystalline phase. The typical TEM micrographs of the nanocomposites with 15 % Ag are shown in Fig. 4.6 with the corresponding SAED patterns.

At all MVFs, similar behaviour was observed. Detailed analysis using SAED studies and EDX analysis in nanoprobe mode confirmed the formation of crystalline TiO phase. The detailed structural emergence of TiO in the Ag–TiO_2 nanocomposite thin film system induced by SHI will be discussed in detail in the following paragraphs.

On SHI irradiation of the nanocomposites with 13 % Ag, the formation of a large single crystalline TiO has been observed at a particular fluence of 3×10^{12} ions/cm^2 (Fig. 4.7). The formed crystals are of the order of nearly 400 nm in size (Fig. 4.7) and have similar d–spacings as reported in literature by Bartkowski et al. [173] for TiO. Relatively very few reports about the formation of TiO nanostructures through various methods are seen in literature [174, 175].

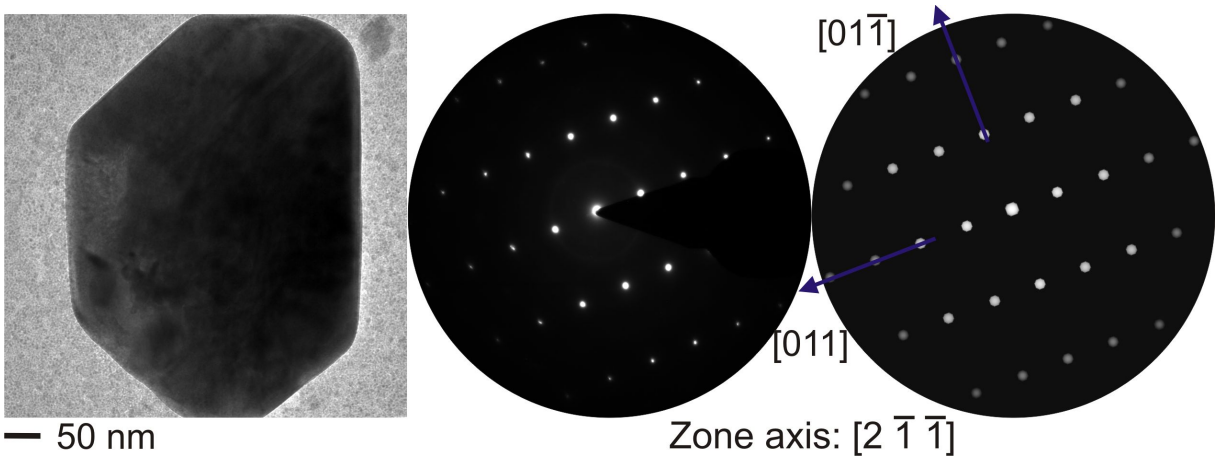

Figure 4.7: *TEM micrograph of the TiO crystals that are formed at the fluence of* 3×10^{12} *ions/cm*^{2} *with the associated experimental (center) and simulated (right) SAED patterns showing clearly the single crystalline nature in the zone axis of [2* $\bar{1}$ $\bar{1}$*]. SAED pattern simulations were done using the the software JEMS [176].*

The formation of TiO nanostructures in the Ag–TiO_2 nanocomposites is only possible by SHI irradiation but not possible by conventional heating experiments. A comparative

study involving the in–situ heating of the Ag–TiO_2 nanocomposites in the TEM confirms the absence of the formation of TiO as will be discussed later in section 4.3. Despite many attempts towards the synthesis of TiO thin films for microelectronics and sensoric applications have been carried out [177]. But less reports towards the synthesis of nanostructured TiO have been published. When compared to the films of TiO, enhancement of the nitrogen dioxide sensing would be due to the increased surface area resulting from the nanostructures of TiO. The observation that the precipitation of the TiO phase takes place only for a specific fluence is rather unique.

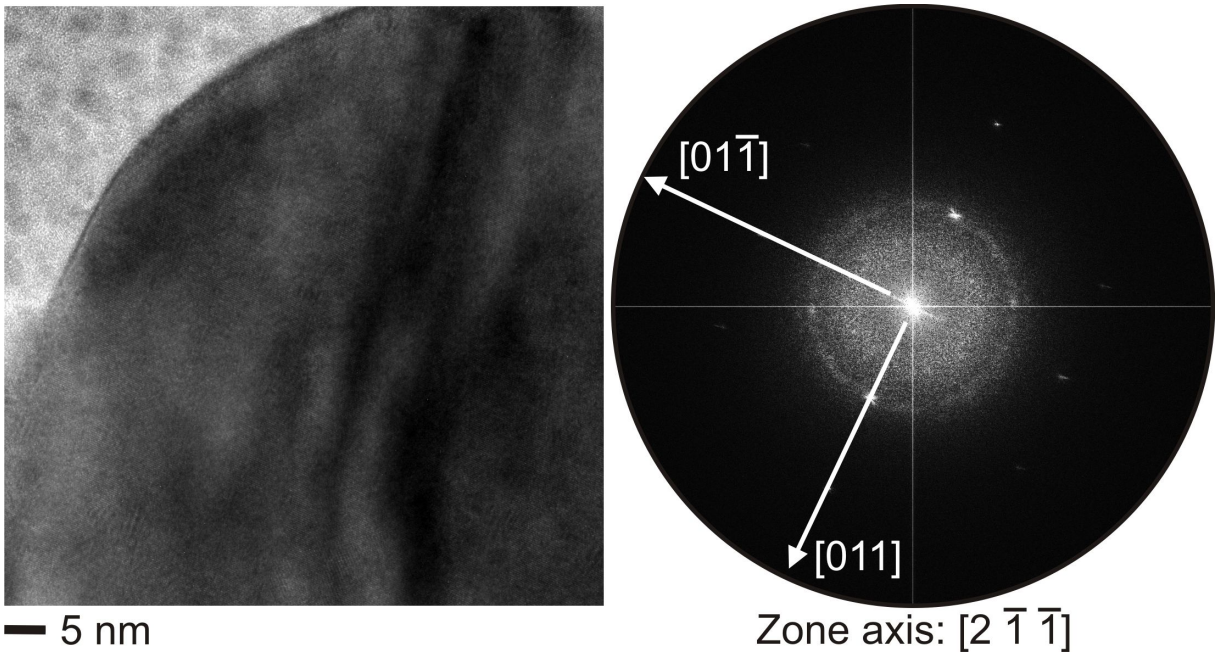

Figure 4.8: *The HRTEM micrograph of the formed TiO phase showing the lattice fringes and the associated FFT showing the zone axis orientation of [2 $\bar{1}$ $\bar{1}$].*

SAED studies together with the HRTEM and EDX confirm the formation of TiO. From the SAED patterns, one can clearly see the [2 $\bar{1}$ $\bar{1}$] zone axis of the TiO phase which agrees with the simulated results of the TiO by using the JEMS software [176]. The difference of the intensities in the SAED pattern can be attributed to the thickness of the formed TiO phase. Similar to the SAED pattern in Fig. 4.7, the HRTEM micrograph depicts the lattice fringes. The fast Fourier transformation (FFT) of the HRTEM micrograph yield an FFT pattern (Fig. 4.8) which corresponds to the SAED pattern in Fig. 4.7.

The HRTEM image clearly show the lattice fringes of the TiO crystals in the Ag–

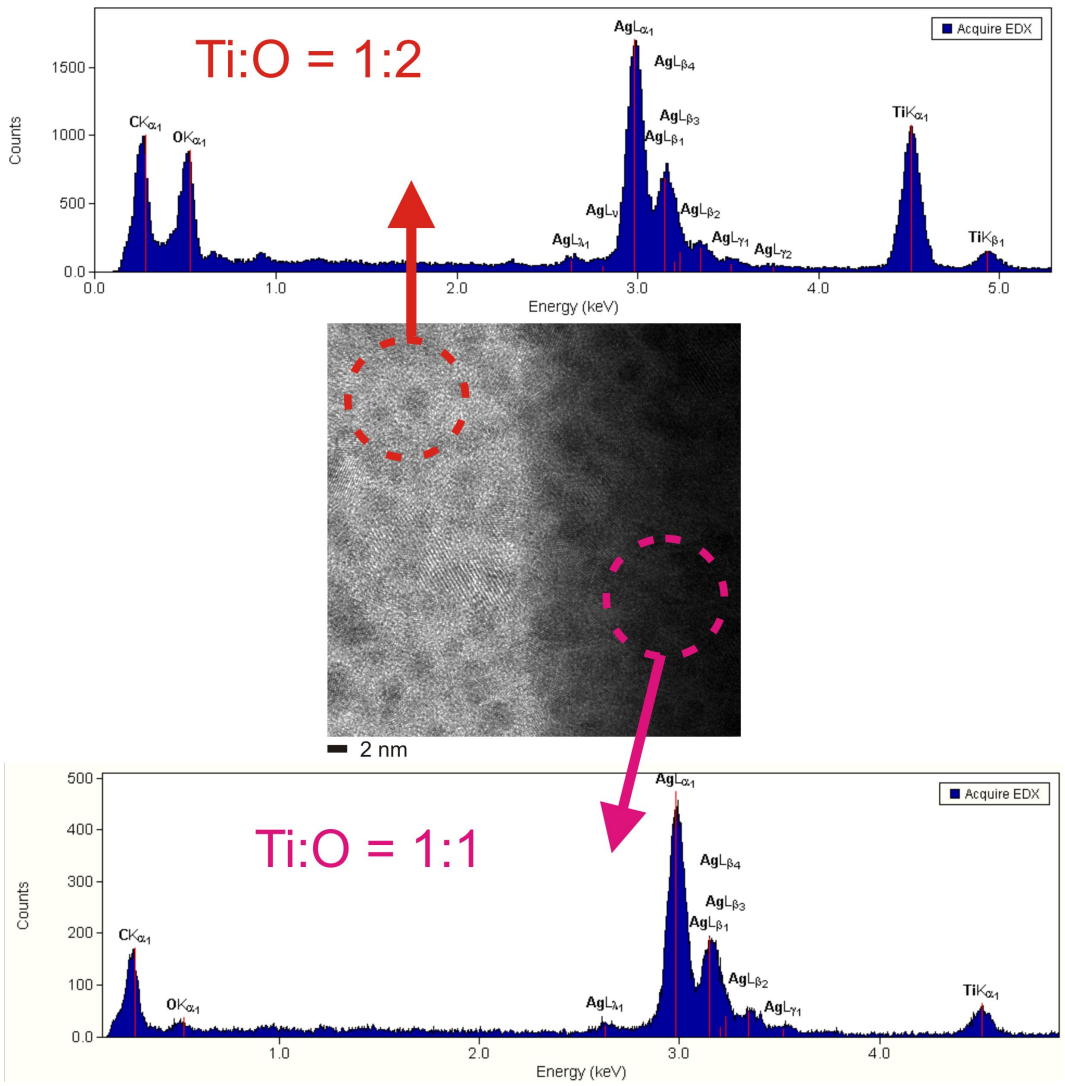

Figure 4.9: *TEM nanoprobe EDX analysis on the TiO crystal and the matrix confirming the ratio of Ti:O in both the areas to be 1:1 and 1:2 respectively.*

TiO_2 nanocomposite thin films. In spite of the well known problems of the light elements' quantification by EDX, test measurements on distinct samples (e.g., amorphous TiO_2) point to a sufficient reliability of the setup for a semi–quantitative interpretation. Hence, the EDX–nanoprobe analysis of the transmission electron microscope (Fig. 4.9) confirms that the ratio of Ti:O in the nanocomposite is 1:2 and that it is 1:1 in the nanocrystal. Interestingly, the desired equimolar ratio of Ti and O is well adjusted even on the nanoscale.

Usually, physical effects like the formation of carbonaceous clusters or excessive free volume, or the mass density, spin density and conductivity enhancement in the case of

irradiated insulating polymers [178] sets in above a certain critical energy density thresholds in the order of 0.03 to 3 eV/Å. Thereafter these reach saturation values at typically 10 to 1000 times higher energy densities. Hence the fact that, in the present case the phase formation briefly shows up and then vanishes again with increasing fluence can only be understood by the interaction of two different counteracting mechanisms evolving at different fluences. This can be also seen from the Fig. 4.10 where at lower fluences, one observes the tendency towards the formation of TiO, with larger unaffected area. At higher fluences, one can see the destruction of the evolved TiO phase into fragments.

Similar fluence dependence was reported by Bacmeister et al. [179] where they found this effect for gas permeation through irradiated polymers. In this effect, at a low SHI fluence of 4×10^{10} ions/cm^2 the gas diffusion coefficient rose to a value twice a that of the pristine material. On a slight increase in the fluence to 6×10^{10} ions/cm^2, the coefficient dropped to a value drastically below that of the pristine. Similar results were also observed for electron irradiated materials. The decrease of the coefficient was explained by a three–phase model [180] that assumed that gases in irradiated materials diffuse through both the pristine bulk and the tracks. Individual ion impacts lead to the behavior that the ion tracks act as zones of enhanced diffusivity. Multiple ion hits lead to volume compaction and hence to a reduction of the diffusion along the tracks. This makes it highly probable that we deal here with the counter play between "hit" and "no–hit", "single–hit" and "multiple–hit" processes.

On assuming that the TiO phase emerges only within individual tracks and is destroyed again upon multiple hits, then the probability to find such a track at a given projectile fluence Φ_t (also the areal track density) on a given target unit area with cross–section $\sigma_t = \pi(r_t)^2$ is W_1.

$$W_1 = exp(-\xi). \tag{4.1}$$

where $\xi = 4P$ and $P = \Phi_t \sigma_t$.

The formation of the TiO phase at an optimum fluence of about 3×10^{11} ions/cm^2 signifies that the σ_t for this process is of the order of 3×10^{-12} ions/cm^2. Hence, the

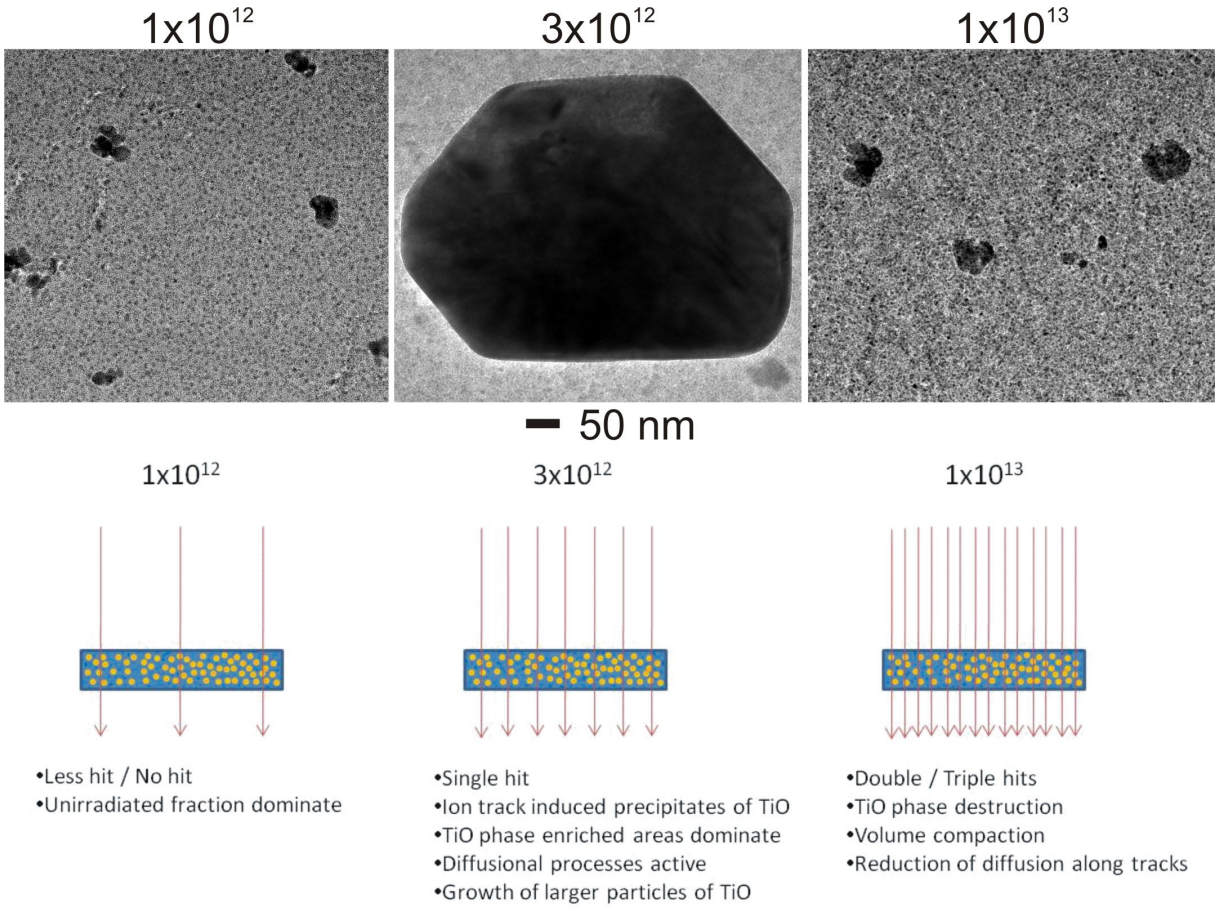

Figure 4.10: *The effect of different fluences on this nanocomposites system showing effect of the variation of fluence on the formation of single crystalline TiO is shown with a supporting model about the formation of TiO only at a particular fluence.*

effective ion track radius for this effect is in the order of nearly 6 nm (r_1). With increasing fluence, the chance that a given target area is hit twice increases, with the corresponding probability being given by [181]:

$$W_2 = \xi exp(-1.185\xi). \tag{4.2}$$

Riedel et al. [182] give the correlation for the areal fraction of overlapping tracks as:

$$P_2 = 4Pexp(-6.645P). \tag{4.3}$$

with P = $\Phi_t \pi (r_t)^2$ being the total area covered with tracks without taking the track over-

lapping into account.

According to the suggested model, this signifies that for the lowest values of $P = \Phi_t \sigma_t$, no TiO phase is seen, as the unaffected areal fraction still dominates. On increasing $\Phi_t \sigma_t$, TiO phase enriched areas emerge due to the appearance of individual ion tracks. When this areal fraction (corresponding to the areal fraction of individual tracks) reaches its maximum, already first pixels with double and triple overlapping tracks show up in the target. According to this model, the emergence of a double or multiple hits signify phase destruction, the further increase in fluence leads to the destruction of that previously created TiO phase as can be clearly seen from the schematic of Fig. 4.10.

As the track populations follow Poisson distributions for the probabilities of i–fold ion track overlapping with $i \geq 0$ (i = 0: no track, i = 1: individual tracks, i > 2: ion track overlapping), the transition zones between "no hit", "single hit" and "multiple hit" areas in dependence of the fluence (consequently also the transition regimes between the existence and non–existence of the TiO phase) are relatively broad. However, additional diffusional processes, depending on the diffusion and kinetics of the TiO clusters in the TiO_2 matrix, in the presence of a transient localized high temperature, tend to sharpen these transitions, e.g., by dissolution of too small or too dispersed TiO phase clusters on the one hand, and on the other hand by enabling the small ion track–induced precipitates to grow to the large TiO clusters which were observed in the TEM images.

In addition to this, reflections corresponding to the Anatase form of crystalline TiO_2 have also been observed at fluences of 3×10^{12} and 1×10^{13} ions/cm^2. This can be attributed to the transient local increase in the temperature during SHI irradiation.

4.1.3 Optical properties

In this work, the optical properties of the noble metal based nanocomposites were determined by the collective oscillations of the metal's conduction electrons with respect to the positive ion background, known as SPR, as already discussed in the chapter 2. For noble metal nanoparticles, the resonance occurs in the visible region of electromagnetic spectrum which

enables them as the potential candidates for optical and sensor applications. The SPR frequency not only depends on the size, shape and size distribution of the nanoparticles [35,101,102] but also on the dielectric constant of the medium [98,99] and the inter–particle spacing [98,107]. The decrease in the inter–particle spacing leads to the coupling of plasmons which results in SPR broadening.

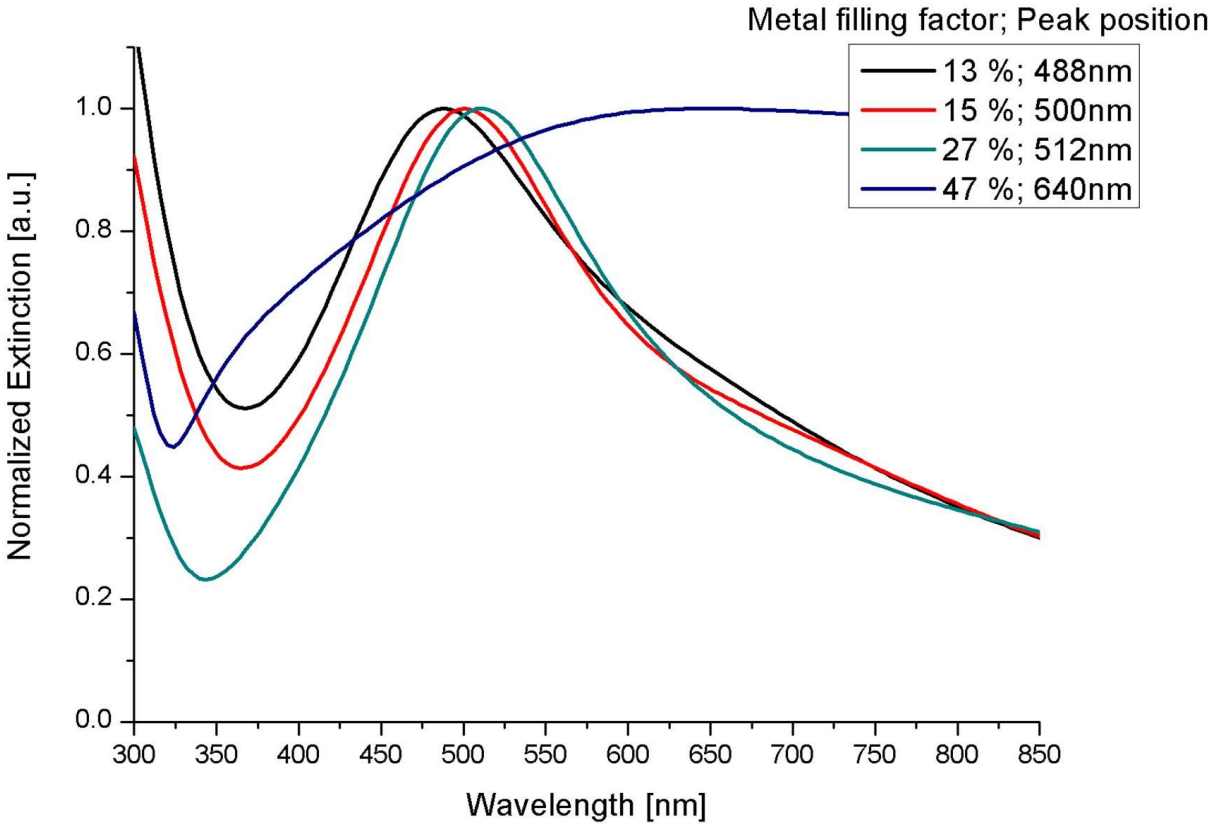

Figure 4.11: *Optical extinction spectra of the Ag–TiO_2 nanocomposites with different MVFs from 13 % Ag to 47 % Ag in the visible regime showing the red shift in the SPR from 488 nm to 640 nm.*

In Ag–TiO_2 nanocomposites, when tuning the MVF from 13 % to 47 % Ag, the SPR peak shows a red shift (Fig. 4.11) from 488 nm to 640 nm. Both the size and the interparticle distances play a major role in determining the optical properties of these nanocomposite thin films [35,98,101,102,107]. The SPR spectrum of the nanocomposite with 15 % Ag, shows a peak at 500 nm (Fig. 4.12) with an additional shoulder peak.

On peak deconvolution of the SPR spectrum with a Gauss fit from 15 % Ag nanocomposite, a prominent peak at around 498 nm and a shoulder peak at around 630 nm (Fig. 4.12) is seen. The near field interactions between closely spaced metal nanoparticles result in

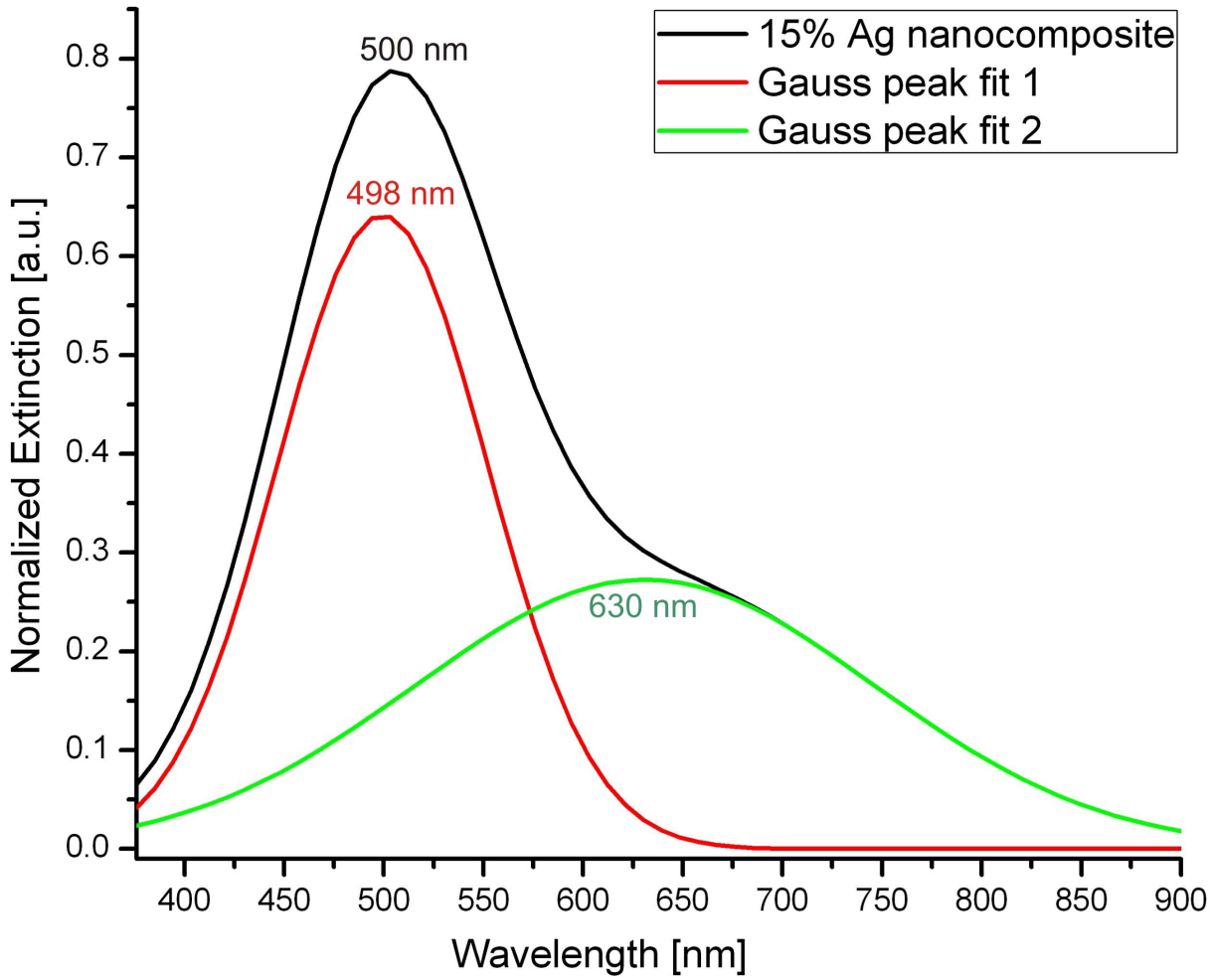

Figure 4.12: *Optical extinction spectra of the Ag–TiO_2 nanocomposites with 15 % Ag MVF. Gauss peak fit showing the deconvoluted peaks at 498 nm and 630 nm.*

properties that are absent in the case of individual nanoparticles [183]. When two plasmon–resonant particles are close, the plasmon modes in the individual nanoparticles can interact, leading to resonances from the coupled system [184]. Similar to the case of the equal intensity double plasmon resonance [100], in the present case, a near electromagnetic field coupling from the lateral–to–surface and perpendicular–to–surface directions between two metallic surfaces placed at short distance presents a large change compared to an isolated surface [185]. The relaxation or damping frequency or parameter is related to the mean free path of the conduction electrons and the velocity of electrons at the Fermi energy. The most important parameter affecting the damping parameter is the particle size [186]. However, in this case since the particle size on the surface is larger, the damping is more radiative in

nature, which leads to further red–shift and broadening of the resonance. As the theoretical treatments predict a red–shift and broadening of the corresponding peaks upon interaction between plasmon resonances in different particles [187], the results in this case agree with the strong coupling of plasmon resonances. Thus, segregation influences the properties of the nanoparticles thereby affecting the nanocomposite. The driving force for the surface segregations are reduction in surface free energy and bulk elastic strain energy as well as the variation in the particle size. The increase in the MVF has also an effect on the increase in the cluster size with an associated decrease in the interparticle distance, which leads to a shift in the SPR to higher wavelengths, thus tuning the SPR. At higher MVFs of 47 % Ag, the decrease in the interparticle spacing results in a SPR broadening as can be seen in Fig. 4.11.

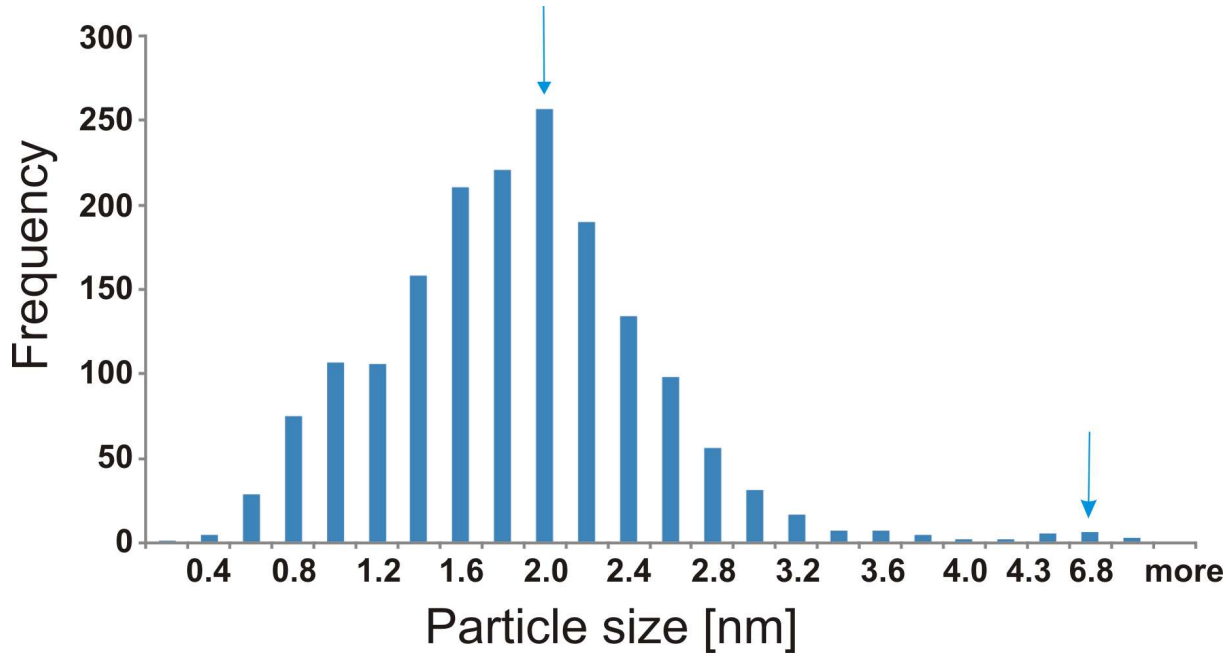

Figure 4.13: *Particle size distribution of the nanocomposite in Fig. 4.2 showing clearly the two particle sizes.*

Thus, from the 3D nanostructure of the nanocomposite thin films obtained by electron tomography (Fig. 4.3), the optical extinction and the peak deconvolution (Fig. 4.12), it can be concluded that the lateral and perpendicular coupling between large nanoparticles and small nanoparticles gives rise to the SPR resonances at 630 nm and 498 nm. This can also be observed from the particle size distribution of the TEM image (Fig. 4.13). The ability to control the exact position of nanoparticles within a dielectric matrix facilitates the tailoring

of the resulting properties of the nanocomposite and remains a pivotal parameter.

4.1.3.1 SHI induced changes in the optical properties

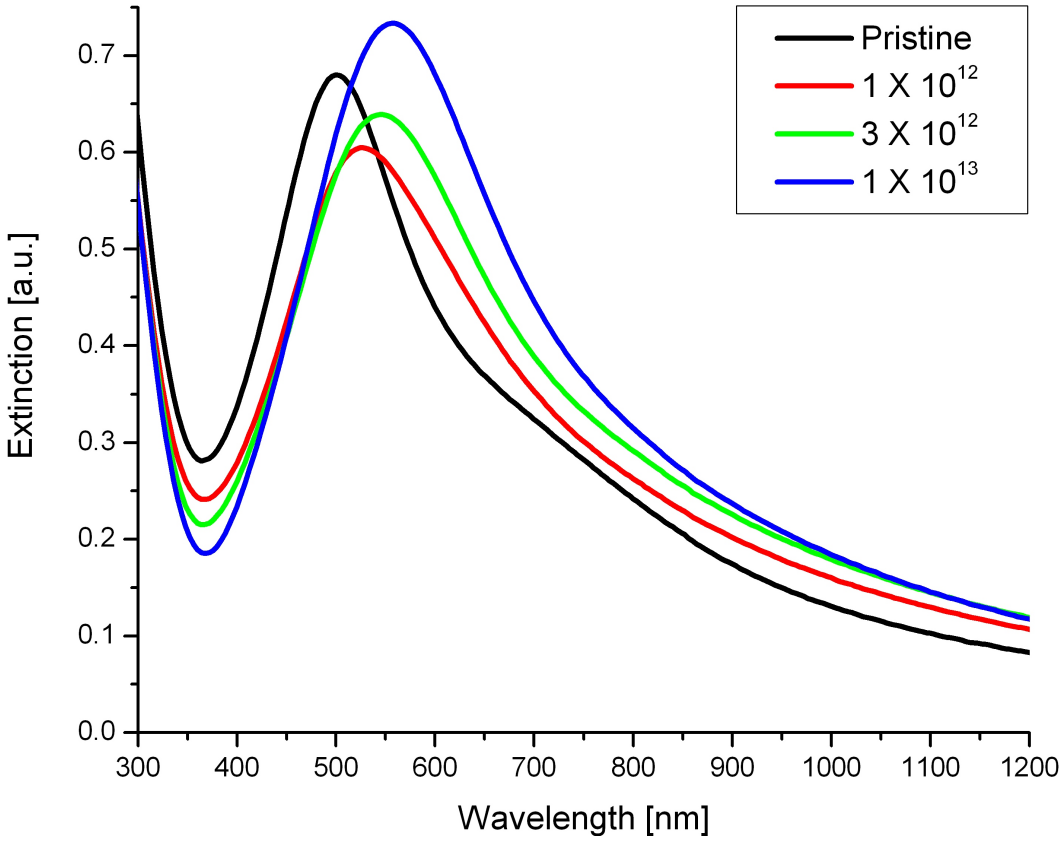

Figure 4.14: *15 % Ag nanocomposite before and after irradiation at different fluences.*

On irradiation with the 100 MeV Ag^{8+} ion beam at various fluences of 1×10^{12}, 3×10^{12} and 1×10^{13} ions/cm^2 changes in the optical spectrum like narrowing of the SPR peak, along with associated changes in the particle morphologies have been observed. Since the observed changes in the optical spectra are similar at different MVFs, only MVF of 15 % has been depicted here.

The changes in the optical extinction spectrum of the nanocomposites of Ag–TiO_2 with 15 % Ag on irradiation can be seen in the Fig. 4.14. The red shift in the SPR can be attributed to the changes in the matrix properties along with the associated narrowing of the size distribution. The shift of the SPR from 465 nm to 550 nm can be clearly seen, thus the ion beam fluence can be used as a tool in order to tune the SPR. The resulting

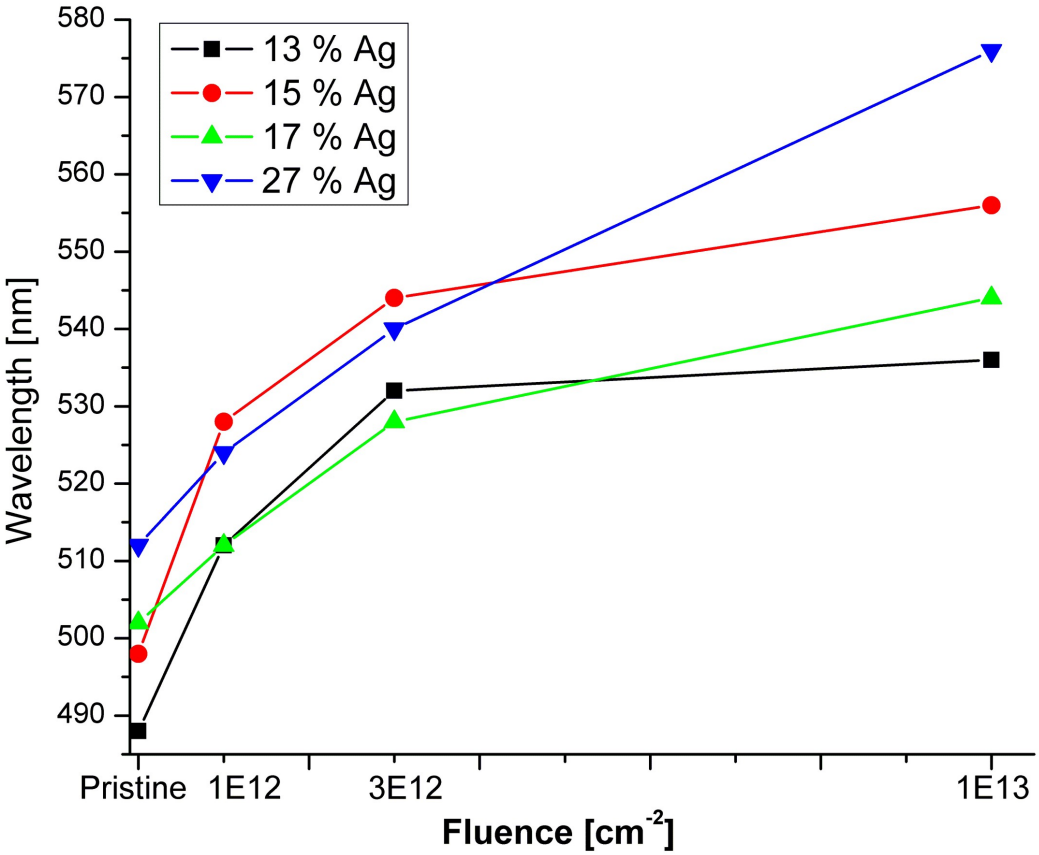

Figure 4.15: *Plot showing the change in the SPR peak maximum with respect to fluences of* 1×10^{12}, 3×10^{12} *and* 1×10^{13} *ions/cm*^{2} *for 13 %, 15 %, 17 % and 27 % MVFs in the Ag–TiO*$_2$ *nanocomposite system.*

shift in the plasmon resonance can be a result of interplay of many factors. Firstly, as the particle diameter increases to about 12 nm, there is a corresponding shift of the SPR towards higher wavelengths. From the experimental calculations in [188] (page 147), for a medium with a refractive index of 1.4, an increase in the particle radius from ∼6 to ∼12.5 nm yields a red shift in the SPR of about 8 nm. The refractive index is a key feature in optical applications [6, 99, 189–191]. The effect of the changes in the refractive index of the embedding matrix is also important, as for Ag nanoparticles with particle diameter of about 10 nm, Quinten [188](pp200) has shown a red shift of 8 nm in the SPR peak. On the other hand, for Ag nanoparticles, Mock et al. [190] have suggested a 1.6 nm red shift for every increase of 0.01 in the refractive index. Amorphous TiO_2, crystalline TiO_2 with Anatase sturucture and TiO have refractive indicies of 2.05 [140], 2.54 [192] and 2.27 [193].

In our case, the transistion of the matrix from amorphous TiO_2 to TiO + amorphous TiO_2 or TiO and nanocrystalline TiO_2 leads to an associated change in the refractive index of the nanocomposites. Hence, there exists an interplay between the associated change in the refractive index, the particle size distribution in the resulting red shift from 465 nm to 550 nm. This can be clearly seen by the plot between the ion fluence and the SPR peak maxima for different MVFs (Fig. 4.15).

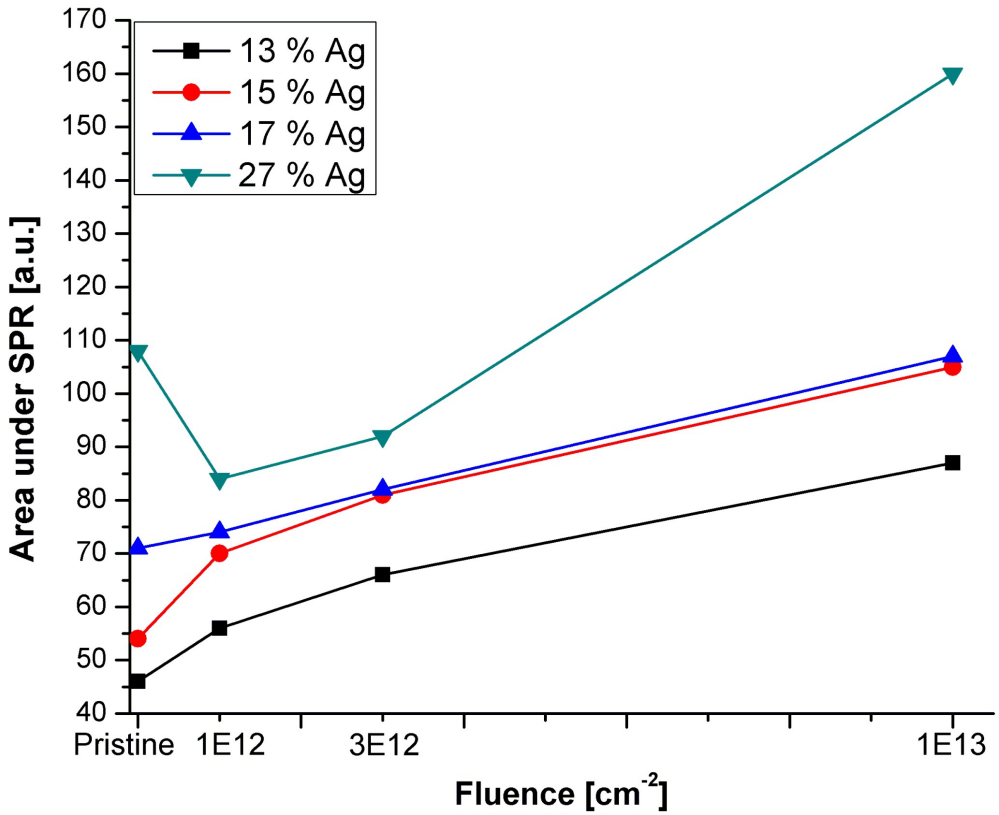

Figure 4.16: *Plot showing the change in the area under the SPR peak vs the ion fluence for 13 %, 15 %, 17 % and 27 % MVFs at different fluences of* 1×10^{12}, 3×10^{12} *and* 1×10^{13} *ions/cm*^{2} *in the Ag–*TiO_2 *nanocomposite system.*

Additionally, different MVFs follow a similar trend of the SPR shift towards higher fluences. At a constant MVF, the area under the plasmon peak is a measure of particle size distribution [194]. A plot showing the area under the SPR vs the fluence indicates a trend in the particle size distribution. Hence, in Fig. 4.16, the increasing trend of all the MVFs at different fluences confirms the results obtained from TEM images (Fig. 4.5).

4.1.4 Antibacterial properties

In the recent years, silver embedded in different matrices have become quite important because of the prospective applications such as in imaging, biosensing, biodiagnostics and optical filters, as well as antimicrobial, catalytic and photocatalytic processes [18, 45, 50–52, 122, 164, 195, 196]. Apart from the excellent optical properties of the silver based nanoparticles and the Ag–TiO_2 nanocomposites (Fig. 4.11), the silver ions released from the silver based nanoparticles are known to inhibit bacterial growth thus showing them to be as good antimicrobial agents [122,197]. TiO_2 itself is known to be antibacterial, however, this requires UV light irradiation [198]. Here it has been shown that by incorporating Ag nanoparticles, the nanocomposite exhibits antibacterial activity even in the dark. The experimental results of the synthesis, characterization of the nanocomposites, the release of silver and their antibacterial properties based on bacteriostatic (growth inhibition) impact are presented in the following sections. For the measurement of the antibacterial properties cultures of Bacillus megaterium ATCC1458 (B.megaterium), Staphylococcus aureus ATCC6538 (S.aureus), Staphylococcus epidermidis ATCC 155 (S.epidermidis) were used. Also, the bacteriostatic impact, i.e., the time dependent bacterial growth of Escherichia Coli (E.Coli) SAR 18 on these Ag–TiO_2 nanocomposites deposited onto the POM substrates, was studied by using the fluorescence microscopy. Additionally, silver ion release studies, i.e., the relative change in intensity of the signal of Ag with respect to the time, has also been studied at different MVFs.

4.1.4.1 Bacteriostatic impact from fluorescence microscopic studies

The bacteriostatic impact of these nanocomposite coatings was evaluated as a function of time with Escherichia coli SAR 18 (E.Coli). The bacterial growth of E. coli SAR 18 on these coatings on different time scales of 1 hr, 6 hrs and 24 hrs has been monitored through fluorescence microscopic studies thus studying the bacteriostatic impact.

The bactericidal effect of 15 % Ag nanocomposites was evaluated by means of determining the time course of bacterial growth of E.Coli on the nanocomposites. To study the

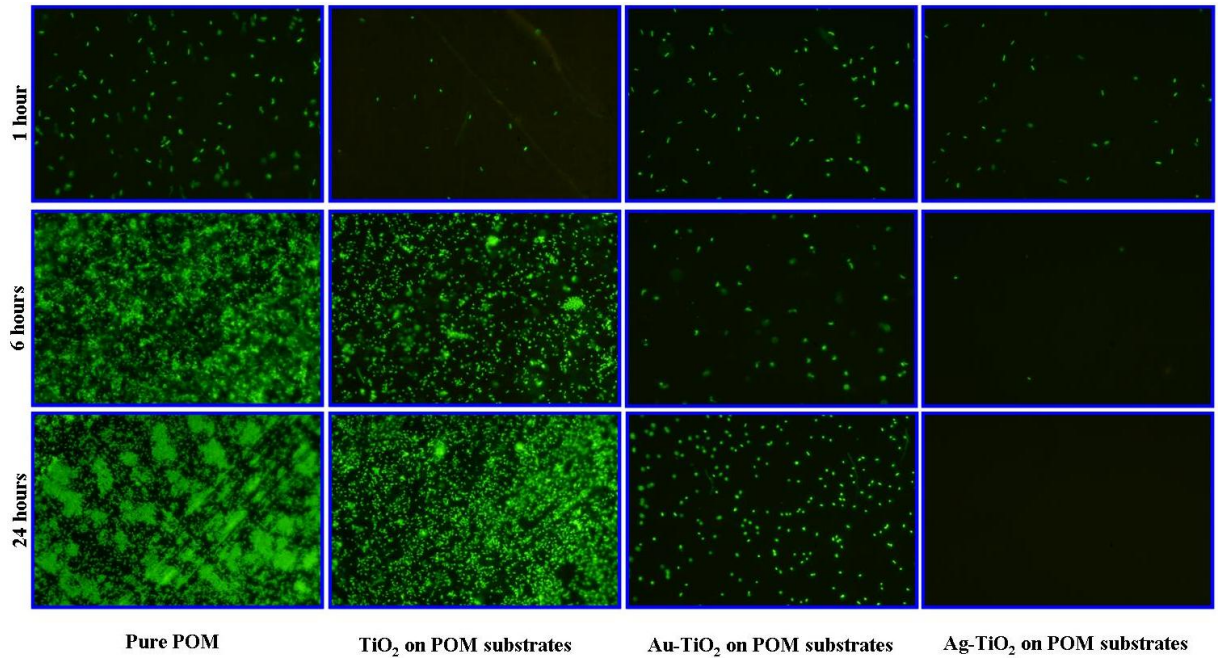

Figure 4.17: *Fluorescence microscopy images from the growth of E.Coli SAR18 on the substrates with coatings of TiO_2, Ag–TiO_2 (15 % Ag), Au–TiO_2 and without coatings, with respect to time scale on POM substrates. The glowing color in the images represents the bacteria grown in the respective areas.*

antibacterial effect on its surface we used an approach that aims at direct visualization of bacterial surface growth by microscopy of test specimen. Significant inhibition of the growth of E.Coli could be noted over the observed time period (1–24 hrs) as shown in Fig. 4.17. To compare and remove the effects from the POM substrates, the bacterial growth studies were performed on the uncoated substrate as well. Pure TiO_2 and Au–TiO_2 nanocomposites have also been examined. From the Fig. 4.17, the glowing of the bacteria grown can be seen on the POM substrates with pure TiO_2. As one can clearly observe, the growth of bacteria is not significant in the Ag–TiO_2 nanocomposites. This retardation of the growth of E.coli SAR 18 bacteria has been found to be maximum on the substrates coated with Ag–TiO_2 nanocomposites making these coatings better than the other coatings. Since pure TiO_2 is also antibacterial in nature when activated by UV–light, here the effect is shown in the absence of UV–light [159].

4.1.4.2 Antibacterial effect from modified conventional disc diffusion method

Different bacteria need different minimal concentrations of silver ions to show a significant antibacterial effect. Bacillus megatherium ATCC1458, Staphylococcus aureus ATCC6538 and Staphylococcus epidermidis ATCC 155 were used as test bacteria for the antibacterial studies by using the modified conventional disc diffusion method at different MVFs. These bacteria have been chosen because of the typical problems caused by these bacteria in medical environments. The results shown in Table 4.18, clearly demonstrate the antibacterial effect of MVFs from 26 %–47 % Ag, to be dependent on the growth medium. Furthermore, the table 4.18 shows enhancement of growth inhibition with increasing MVFs of the nanocomposites.

Silver volume fraction in Ag-TiO_2	B.megatherium ATCC14581	St.aureus ATCC6538	St.epidermidis ATCC 155
26% Ag	negative	negative	negative
31% Ag	1	1	1
44% Ag	2	1.5	1
47% Ag	2	2	2

Figure 4.18: *The tabular results from the modified conventional disc diffusion method showing the effect of MVF from 26 % Ag to 47 % Ag. The corresponding inhibition zone is in mm.*

The "negative" results from the table 4.18 for MVF– 26 % do not say that the nanocomposite is not antibacterial in nature but rather that the response in the form of the diameter of the transparent ring around the nanocomposite is smaller than 1 mm. For nanocomposites with lower MVF, one can clearly observe the antibacterial behavior through the fluorescence microscopic technique.

Two different approaches were used for the antibacterial testing of the nanocomposites. The direct visualization of the bacterial growth is a very sensitive method of antibacterial analysis compared to the modified conventional disc–diffusion method. The later method uses the response in the form of Ag diffusion through the Agar medium and the former method uses the growth of bacteria directly on the surface. The application of these nanocomposites is a necessary criteria towards the appropriate testing conditions for these nanocomposites, i.e., if larger liquid environment is used during application, then the

modified-conventional disc diffusion method would serve as a good alternative because of the usage of higher MVF. On the other hand, if the application involves the growth on surfaces, then the florescence microscopy is a better alternative. The aim of this work was to demonstrate the antibacterial effect of this nanocomposites. Further detailed antimicrobial analysis of the nanocomposites is a detailed work which has to be performed by varying the MVF and at lower MVFs.

4.1.4.3 Silver ion release

Bacteria can survive on its host surface for a long period of time, thus increasing the chance of transmission to food, liquids and human skin [122]. Surfaces coated with the optimal Ag–TiO_2 based nanocomposite should show a maximum antibacterial effect, thus decreasing the chance of transmission of these bacteria. Previously, detergent solutions being bactericidal to S.aureus were studied, but this allowed the survival but not multiplication of E.Coli [199]. In our case, with our Ag–TiO_2 coatings, we have the possibility of antibacterial and bactericidal properties from the same material to different types of bacteria. Furthermore, infections related with intravascular devices, prosthetic joints, catheters, etc. are frequently associated with S. epidermidis. Generally, S.epidermidis contaminates the patient–care equipment and environmental surfaces, possibly explaining the high incidence of this species in the hospital setting. Thus, if coated with Ag–TiO_2, corresponding surfaces provide antibacterial efficacy. At this point, one also needs to consider many other factors like the cytotoxicity and biocompatibility of these materials. These nanocomposites are functional as they have been proved to be antibacterial through the bacteriostatic and antibacterial studies.

Since the silver ion release is the key parameter involved in the antibacterial activity [122] of the Ag based nanocomposites, studies towards this have been carried out. when considering the optical properties of the nanocomposites, the area under the SPR peak represents the MVF of the nanoparticles. Thus one way to study the Ag ion release can be done by by UV–Vis/NIR spectroscopy.

By studying the decrease in the area under the SPR curves, in turn, a decrease in the amount of silver in the composite can be understood. In the previous sections, Fig. 4.11

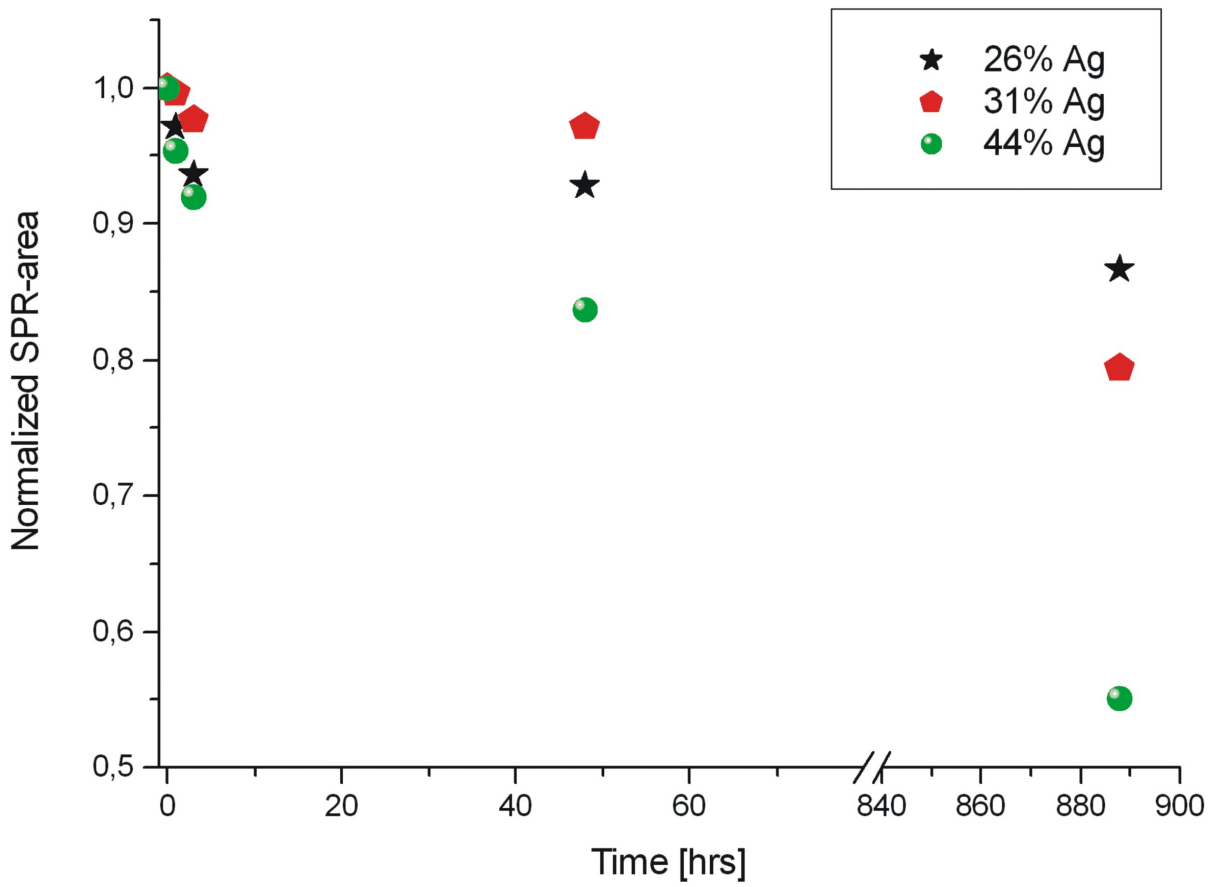

Figure 4.19: *Decrease in the amount of Ag in the Ag-TiO_2 nanocomposites with varying volume fraction from 26 % Ag to 44 % Ag by using the phenomenon of SPR with respect to time.*

shows the change in the SPR with respect to the MVF. Here, Fig. 4.19 shows a correlation between the MVF and the change in the area under the SPR for different time. Two of the MVFs, i.e., 26 % and 31 % are below percolation and 44 % is above percolation (Fig. 4.1). From the area under the SPR over time, i.e., from 0 to 888 hrs, one can clearly see a decrease in the amount of silver. Here, there are two different scales for rate of decrease. At lower time scales, i.e., until 48 hrs the rate of decrease is proportional to the MVF. Faster diffusion in the initial stages results from the significant release in the amount of silver ions. These results until 48 hrs from the area under the SPR were also confirmed by the XPS studies as shown in Fig. 4.20 until 48 hrs. The silver ion release behavior is generally controlled by the diffusion from the bulk to the surface.

The XPS studies of the Ag ion release from the surface in deionized water were carried out on samples with MVFs ranging from 26 % to 44 %. As the method is highly surface

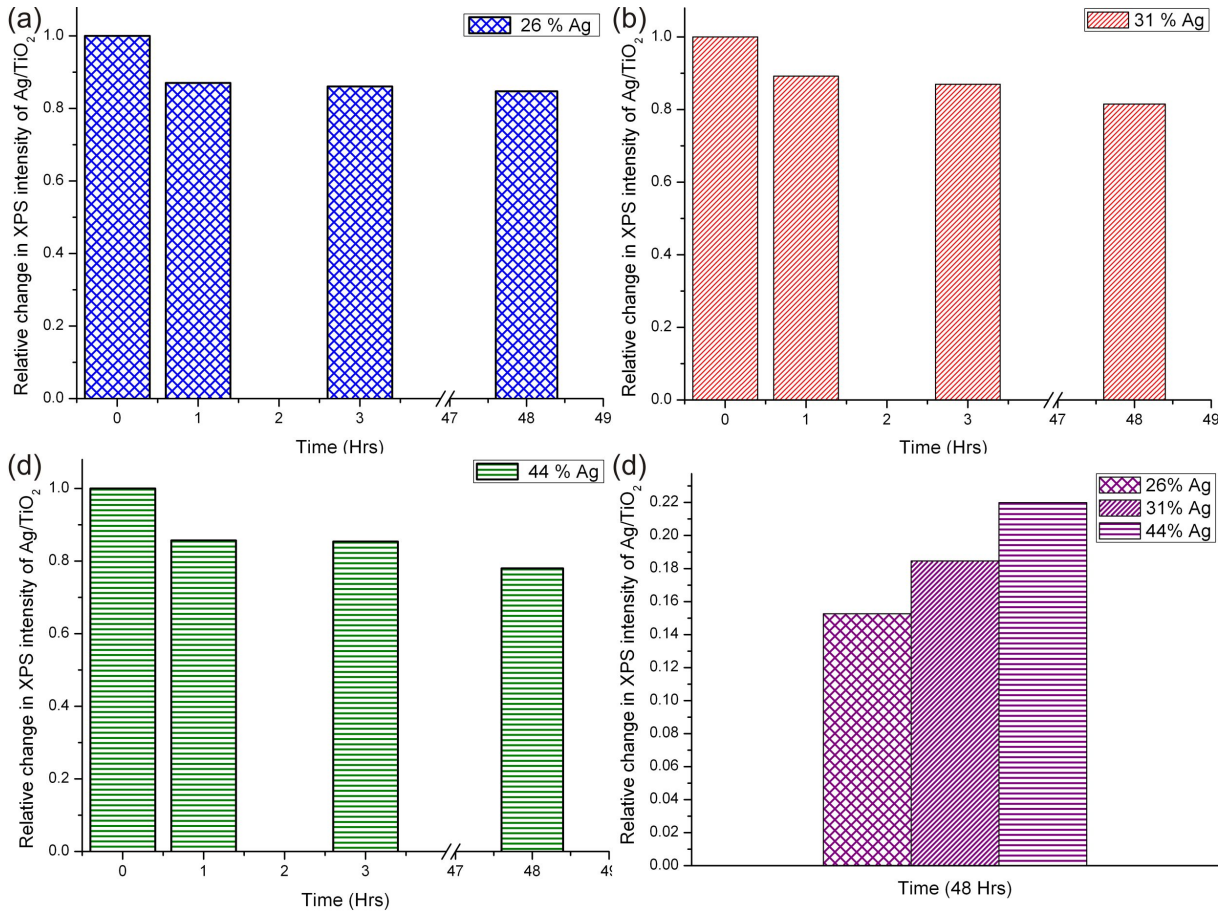

Figure 4.20: *The decrease in the amount of Ag in the Ag–TiO_2 nanocomposites with varying MVF from 26 % Ag to 44 % Ag evaluated by the change in XPS intensity ratio of Ag/TiO_2 with respect to time(a), (b), (c) and (d) depicts the relative change in the concentration of Ag/TiO_2 ($\Delta C/C$, where C is the intensity of Ag/TiO_2) from the XPS signal after 48 hours showing an increase in the concentration of Ag correlating with the results from the modified conventional disc diffusion method.*

sensitive, conclusions about the surface concentration changes of the samples can be made as discussed in chapter 2. By varying the time the samples are kept in water upto 48 hours, the decrease in the amount of silver on the surface was determined from the decrease in the XPS intensity ratio of Ag/TiO_2 as shown in Fig. 4.20. A similar trend was followed by all samples with different MVFs until 48 hrs. These results also correlate with the data obtained through the other methods with different bacteria.

At higher time scales in Fig. 4.19 there is enhanced Ag ion release for the sample with MVF 44 % when compared to the 26 % and the 31 % MVFs. Above the percolation threshold,

there is easy supply of Ag ions from the bulk to the surface. This supply enhancement is due to the percolated network and the possibility for the Ag ion release from the new silver surface availiable through the previously created channels through the Ag ions diffused.

Engineering the silver ion release (an important parameter for the antibacterial activity) through the tuning of the TiO_2 barrier plays a pivotal role in order to obtain a user defined antibacterial activity for a thin film nanocomposite which has to be further dealt in detail.

4.1.4.4 SHI induced modification of the Ag ion release

SHI irradiation causes the formation of ion tracks which results in the variation of the transport properties [178, 200]. As a result, the transient melting along the ion trajectories may lead to a redistribution of the Ag nanoparticles. Because of this redistribution, these ion trajectories might act as tracks for the release of the silver ions. Also, the redistribution of Ag nanoparticles after SHI irradiation also contributes to the silver ion release from the surface. This can be observed from the case of nanocomposites with 27 % Ag. Enhancement of the silver ion release after SHI irradiation with 1×10^{12} ions/cm^2 has been observed when compared to the pristine sample as can be seen in the Fig. 4.21.

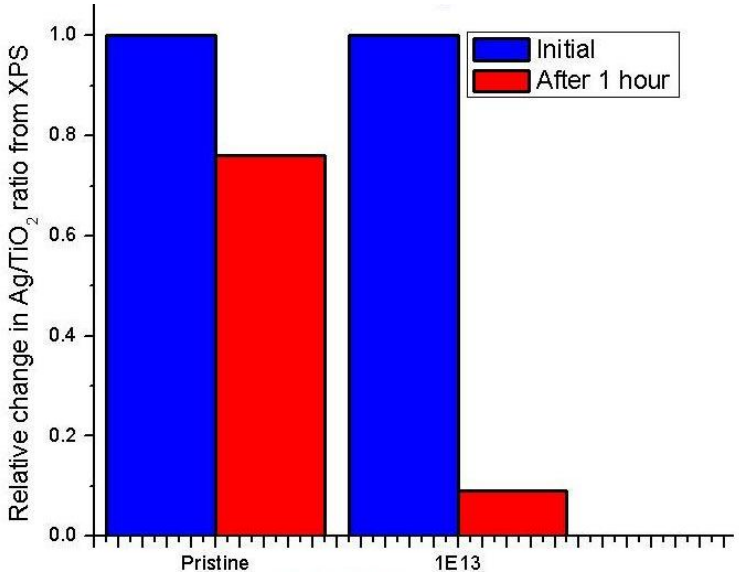

Figure 4.21: *Enhanced release of silver ions after SHI irradiation at a fluence of* 1×10^{13} *ions/cm*^{2} *when compared to the pristine sample.*

The enhancement in the silver ion release after irradiation from the surface might be due to the fact that the ion trajectories after irradiation provide better silver ion release.

4.2 Au–TiO_2 nanocomposites

In this work, the Au–TiO_2 nanocomposite thin films with varying MVFs have been prepared in the same way as the Ag–TiO_2 nanocomposites and are also subsequently subjected to SHI irradiation. Studies about the particle morphologies, the effect of SHI on the TiO_2 matrix and the associated optical properties at different MVFs have been carried out. In the following sections we discuss the respective studies.

4.2.1 Morphology

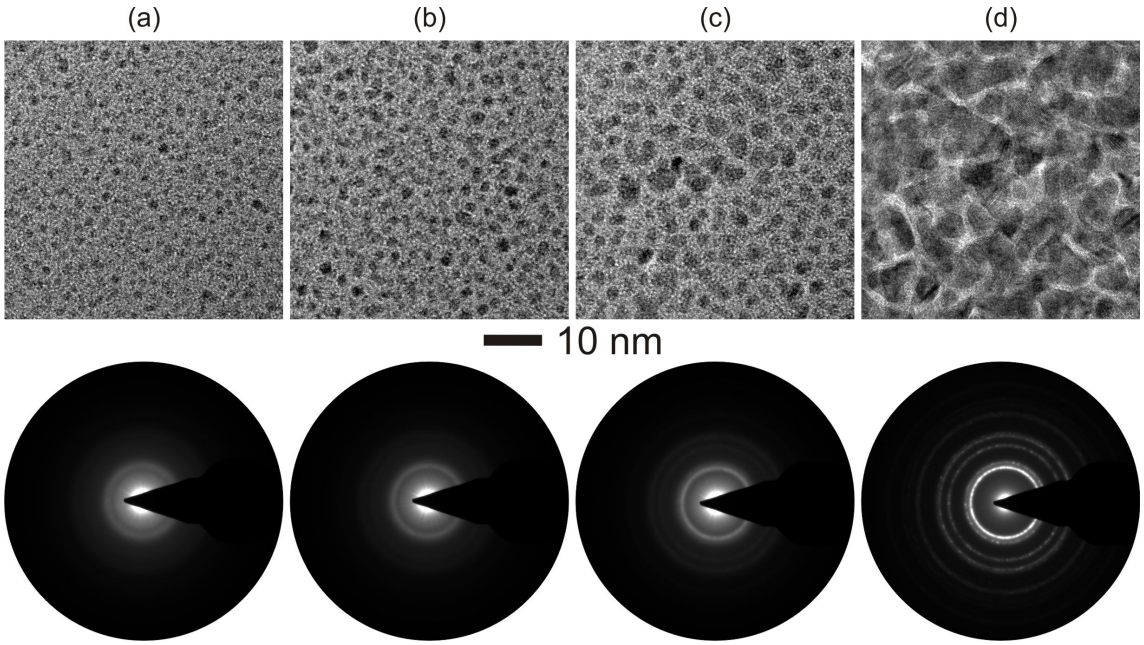

Figure 4.22: *Transmission electron microscopy images of Au–TiO_2 nanocomposites with MVFs of (a) 7 % (b) 11 % (b) 13 % (b) 50 % Au and associated selected area electron diffraction patterns (SAED) showing the crystalline nature of Au nanoparticles.*

The morphology of the nanocomposites have been studied by using transmission electron microscopy (Philips Tecnai F 30 G^2). Also, HRTEM, SAED and electron tomographic

studies have been carried out.

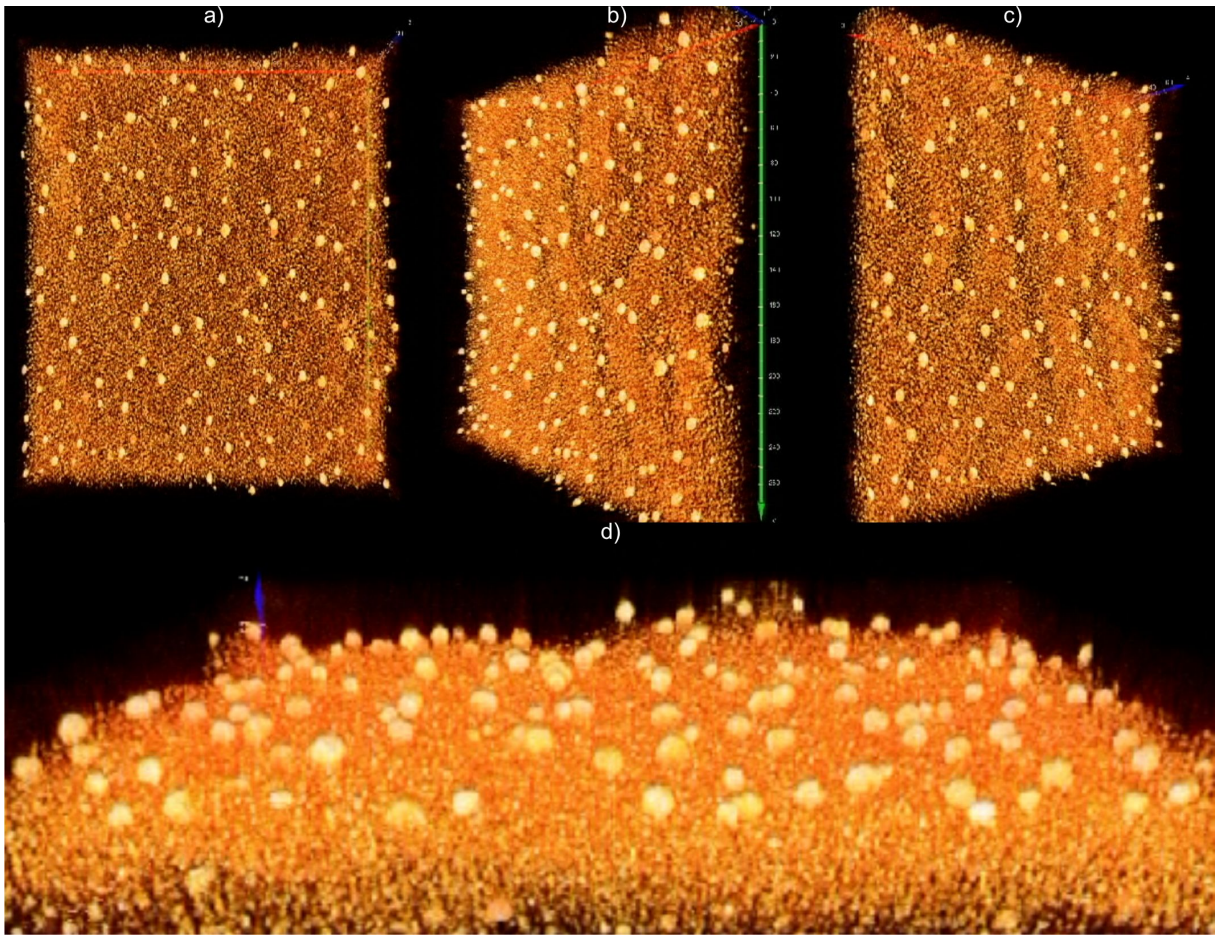

Figure 4.23: *Electron tomographic volume rendering depicting different orientations showing the large Au nanoparticles on the surface with smaller Au nanoparticles in the 15 % MVF Au–TiO_2 nanocomposite thin film.*

In the bright field TEM images of Fig. 4.22 the Au nanoparticles appear with a dark contrast in the bright TiO_2 matrix. The changes in the MVF can be seen from these TEM micrographs (Fig. 4.22), with a variation from 7 % to 50 % Au in the Au–TiO_2 nanocomposites. On careful observation of the Fig. 4.22, two different sizes of nanoparticles can be noticed, both large nanoparticles and small nanoparticles can be noticed.

Similar to the case of Ag–TiO_2 nanocomposites (Fig. 4.4), here the bimodal particle size distribution is observed. On conducting the 3D electron tomographic studies, the volume rendering confirmed the presence of large particles on the surface in this case also, as observed from the Fig. 4.23 in different orientations.

4.2.2 SHI irradiation

4.2.2.1 Variations in particle size

The morphology of the Au–TiO_2 nanocomposites play a pivotal role in regard to their functional properties. In this work, the nanocomposites with different MVFs (7 %, 9 %, 11 %, 15 % Au), were subjected to SHI irradiation with 100 MeV Ag^{8+} ions at various fluences of 1×10^{12}, 3×10^{12} and 1×10^{13} ions/cm^2. Since a similar tendency was observed for the different MVFs, only the 15 % Au MVF will be presented in the following sections.

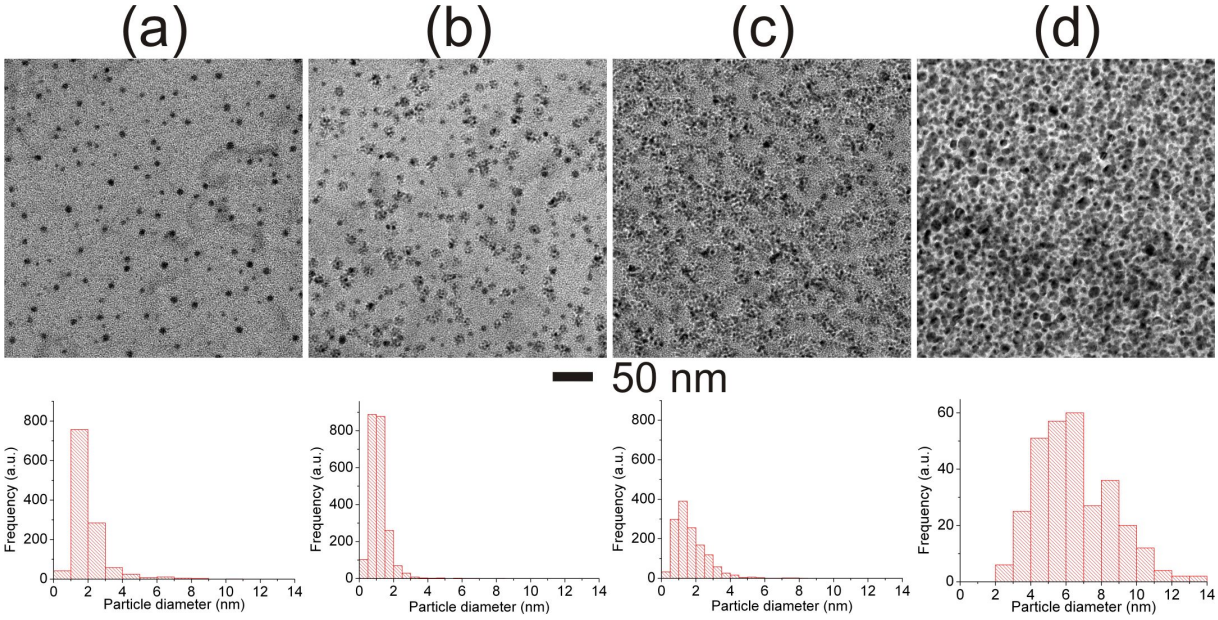

Figure 4.24: *TEM images and the respective particle size distributions of the 15 % Au–TiO_2 nanocomposite (a) before and after SHI irradiation with 100 MeV Ag^{8+} ions at fluences of (b)* 1×10^{12}*, (c)* 3×10^{12} *and (d)* 1×10^{13} *ions/cm^2.*

For the Au–TiO_2 nanocomposites, from the TEM studies, one identifies a trend of particle size growth. In the pristine nanocomposite film, there are nanoparticles as well as metal atoms throughout the film. During SHI irradiation, enormous amount of energy (few keV/nm) is deposited into the nanocomposite thin film. This initiates the phenomenon of nucleation and growth. As can be seen from the TEM micrographs and the corresponding particle size distributions (Fig. 4.24), an increase in the particle size initially at a fluence of 1×10^{12} ions/cm^2 is evident. Upon an increase in the fluence by three times, further growth

of particles continues. This particle coarsening is due to ostwald ripening. which can be seen from the particle size distribution of Fig. 4.24(b) and (c). Also, right from 1×10^{12} ions/cm^2 to 1×10^{13} ions/cm^2, there is a reduction in the average number of nanoparticles. Further increase in the fluence by three times leads to a significant particle coarsening ($\sim$7 nm), i.e., at a fluence of 1×10^{13} ions/cm^2 with an associated decrease in the average number of nanoparticles due to the dissolution and re–precipitation phenomena. According to the energy deposited by the change in the fluence, the amount of dissolution varies [178, 200]. At the fluence of 1×10^{13} ions/cm^2, an increase in the particle diameter to $\sim$7 nm is due to the intensive transient melting and re–precipitation. An explanation for the observed change is due to the SHI induced ripening of small Ag nanoparticles during SHI irradiation. Nanocomposite synthesis using co–sputtering at a particular MVF originally resulted in the formation of nanoparticles with a bimodal particle size distribution as discussed in Fig. 4.23. For a particular MVF, the obtained size of nanoparticles was fixed. Thus, the SHI irradiation indicated a possibility of controlled increase of the nanoparticle size by ion fluence from 100 MeV Ag^{8+} SHI beam.

4.2.2.2 Changes in the matrix

As in the case of the Ag–TiO_2 nanocomposites, there is also ion beam induced crystallization of the matrix leading to the formation of precipitates of TiO in the Au–TiO_2 nanocomposites.

However, unlike in the case of Ag–TiO_2 system, large single crystalline TiO precipitates could not be observed. In the Fig. 4.25(c) one can observe the smaller fractions of TiO distributed in the nanocomposites. The condition for the optimum formation of the larger nanostructures of TiO still remains unknown in this case. The MVF, the type of the metal, the ion fluence and the type of ion beam remain vital parameters towards nanostructuring the nanocomposites. Hence, additional experiments with a broader variation of the ion fluence are required to achieve the condition where nanostructuring occurs, i.e., large single crystalline particles of TiO are formed. Additionally, as in the case of the Ag–TiO_2 nanocomposites, right from an ion fluence of 3×10^{12} ions/cm^2, one can observe the formation of TiO_2 with Anatase structure. Together with the changes in the matrix, as the

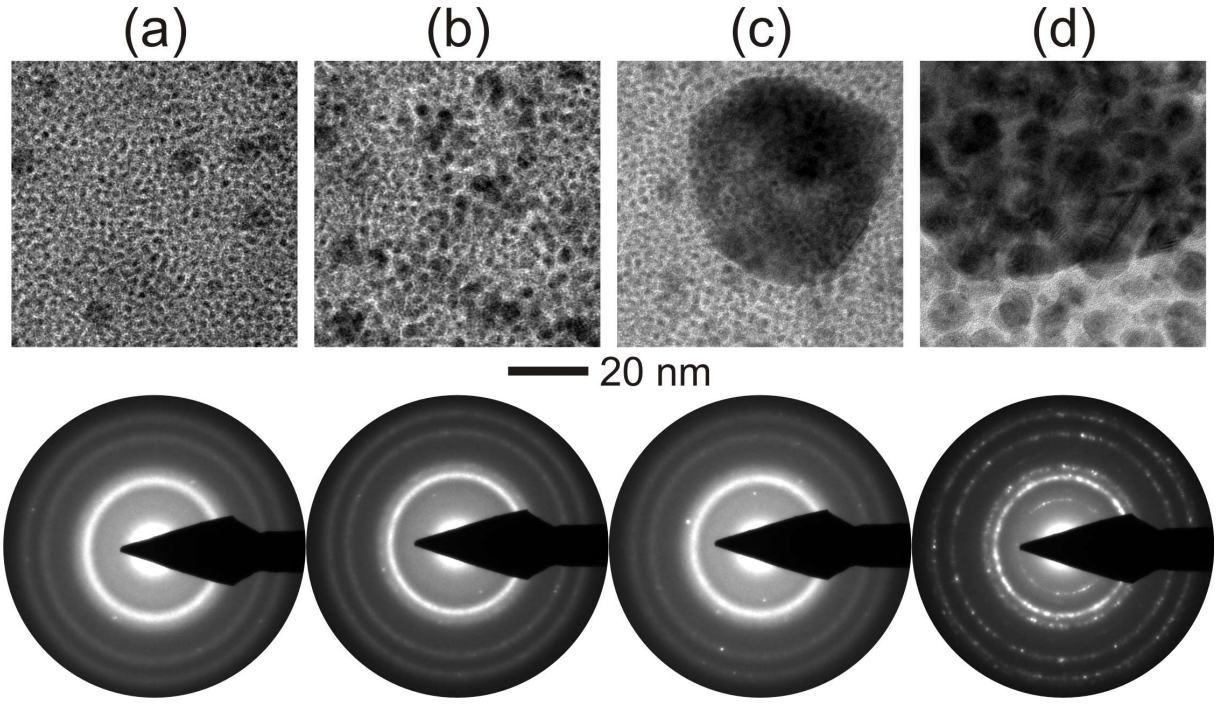

Figure 4.25: *TEM images depicting the changes in the matrix of the 15 % Au–TiO_2 nanocomposite (a) before and after SHI irradiation at at fluences of (b)* 1×10^{12}*, (c)* 3×10^{12} *and (c)* 1×10^{13} *ions/cm*^{2}*.*

particle morphologies play a major role in determining the optical properties, in the next section we discuss the optical properties of these nanocomposites.

4.2.3 Optical properties

In the case of Au–TiO_2 nanocomposites, the change in the MVF from 7 % Au to 15 % Au has resulted in the SPR shift from 572 nm to 584 nm (Fig. 4.26).

From the experimental calculations in Au colloids by [188] (page 147), for a medium with a refractive index of 1.4, a red shift in the SPR of about 12 nm is a result of an increase in the particle radius from ∼13 nm to ∼27 nm. The red shift of 12 nm clearly depicts the change in the particle size with respect to the MVF. Hence in our case, the red shift in SPR can be regarded to be resulting from an interplay of effect of change in the particle size and the plasmon coupling phenomena. This change in the optical absorption is related to the MVF of the nanocomposites and is also in agreement with the results obtained from the

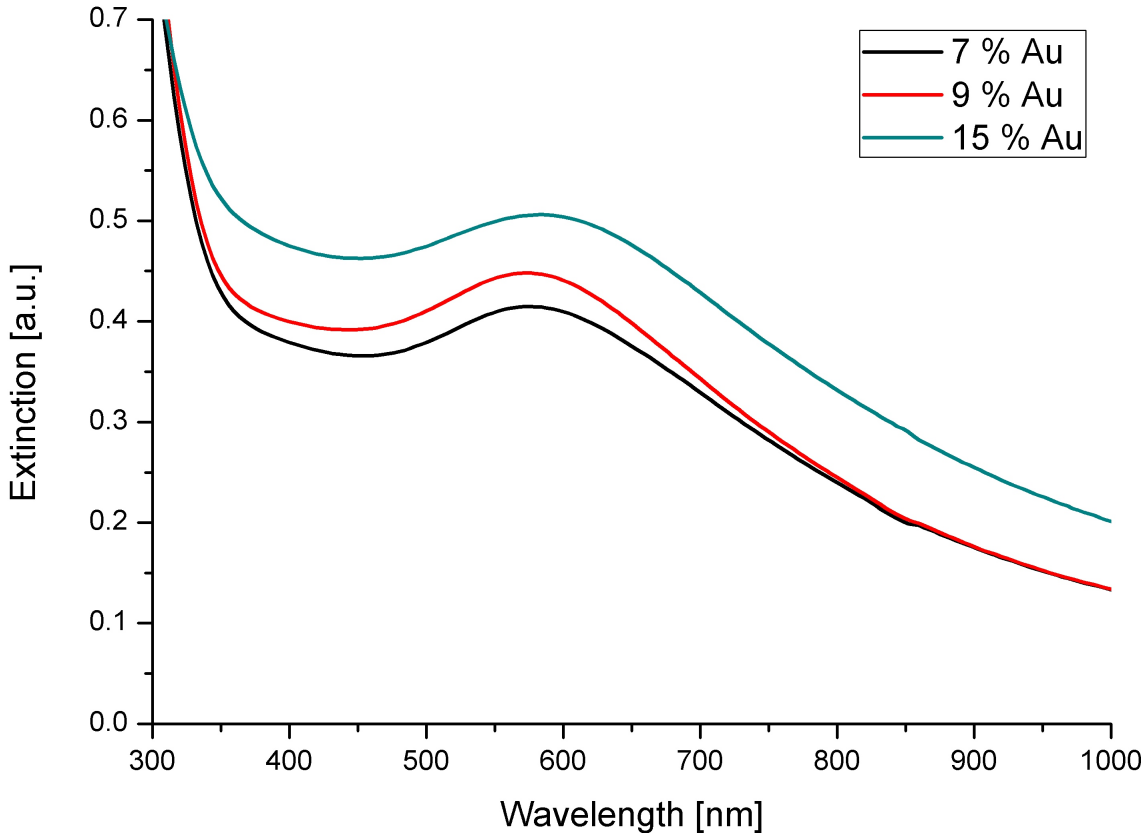

Figure 4.26: *SPR resonance with a variation in the MVF from 7 % to 15 % Au*

transmission electron microscopy (Fig. 4.22).

4.2.3.1 SHI induced changes in the optical properties

The changes in the extinction spectra for the Au–TiO_2 nanocomposites with varying MVFs after irradiation at different fluences follow a similar trend. In order to compare with the Ag based nanocomposites, the MVF of 15 % will discussed here.

In comparison with the SPR from the Ag–TiO_2 nanocomposites with the same MVF (Fig. 4.12), the SPR from the Au–TiO_2 nanocomposites is broad and does not show signs of having a shoulder peak (Fig. 4.27). Although the size of both the large and the small nanoparticles plays a major role in determining the SPR, the observation of a shoulder peak in Ag–TiO_2 nanocomposites only at a particular MVF could be because of the optimum coupling between the plasmons. Similarly, in the present Au–TiO_2, no optimum coupling

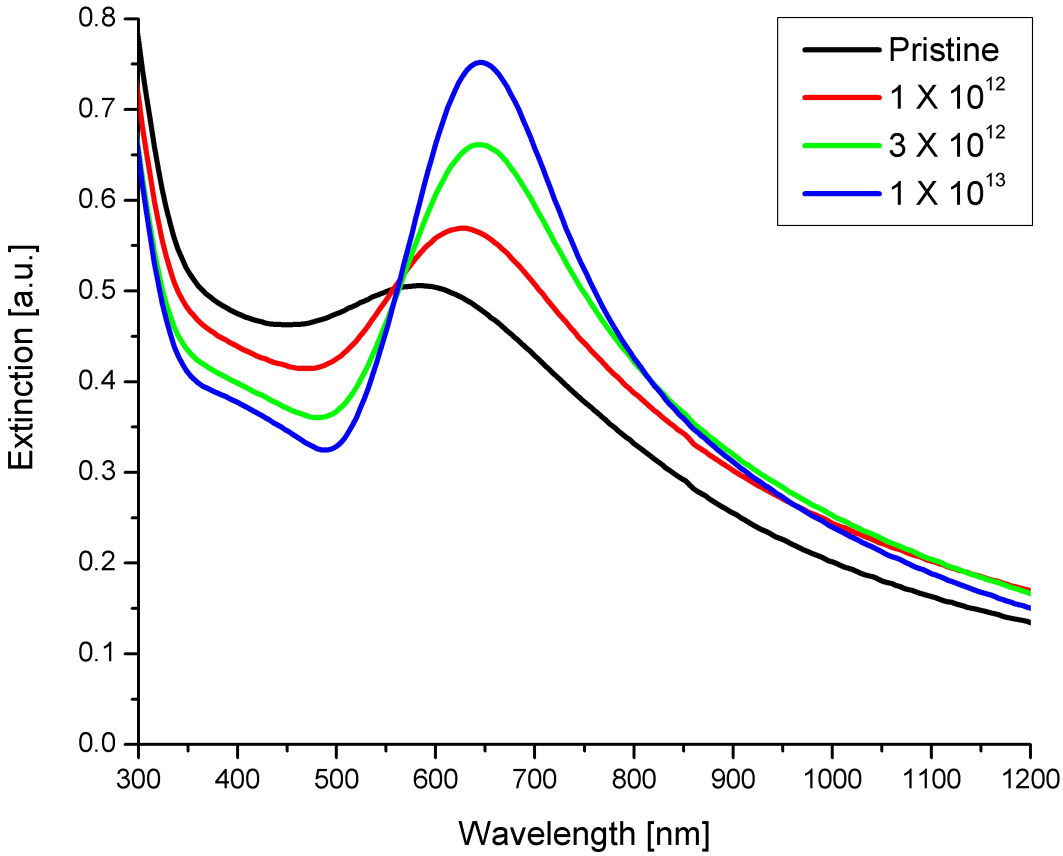

Figure 4.27: *15 % Au nanocomposite before and after SHI irradiation at fluences of* 1×10^{12}, 3×10^{12} *and* 1×10^{13} *ions/cm*^{2}.

resulting a significant shoulder peak was observed.

From the extinction spectra (Fig. 4.27) of the nanocomposites irradiated at fluences of 1×10^{12}, 3×10^{12} and 1×10^{13} ions/cm^2, there is a clear evidence of the narrowing of the SPR peak with a red shift, i.e., 584 nm to 648 nm and an associated reduction in the FWHM and increase in the area under the SPR. Thus, through the variation of the ion beam fluence, the tuning of the SPR frequency from 584 nm to 648 nm in the Au–TiO_2 nanocomposites with 15 % Au by SHI irradiation is evident. The combined effect of the morphology of the nanoparticles and the changes in the matrix are observed from the changes in the optical properties. This effect cannot be separately attributed to a particular contribution.

By SHI irradiation, according to the variation of the SHI fluence and MVF, the SPR frequency shows a red shift from 572 nm to 648 nm in the Au–TiO_2 nanocomposites. This change in the optical extinction spectra of the Au–TiO_2 nanocomposites can be seen in a

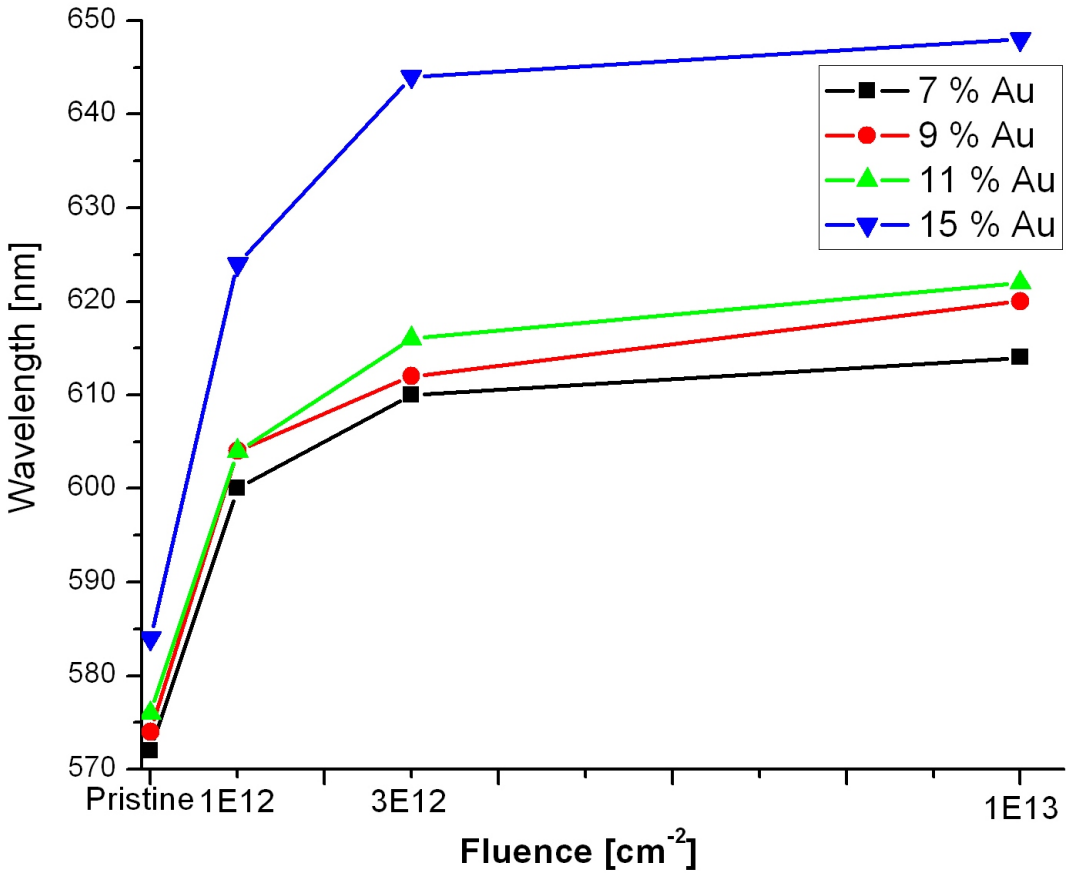

Figure 4.28: *Plot showing the change in the SPR peak maximum with respect to the ion fluence for 7 %, 9 %, 11 % and 15 % MVFs in the Au–TiO_2 nanocomposite system.*

consolidate form in the plot of the ion fluence vs the SPR peak maxima for different MVFs in Fig. 4.28. Additionally, one can clearly observe that different MVFs follow a similar red shift of SPR towards higher fluences. This red shift in the SPR can be attributed to the changes in the matrix properties along with the associated narrowing of the size distribution. The interplay between the associated change in the refractive index and the size distribution of the Au nanoparticles determines the optical properties of these nanocomposites. Since the area under the SPR peak signifies the total density of the nanoparticles, a plot showing the area under the SPR vs the SHI fluence indicates the trend of the particle density at different fluences. Hence, in Fig. 4.29, the increasing trend is in agreement with the results obtained through the transmission electron microscopy.

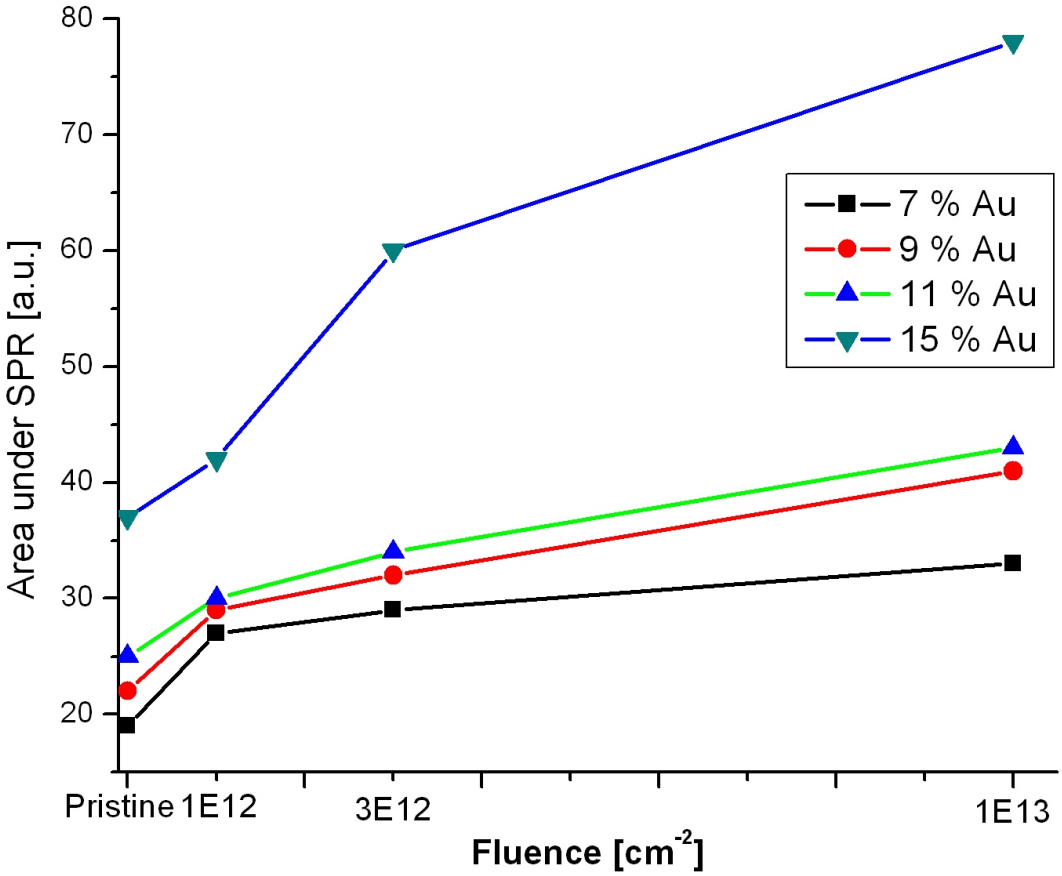

Figure 4.29: *Plot showing the change in the area under the SPR peak vs the ion fluence for 7 %, 9 %, 11 % and 15 % MVFs in the Au–TiO_2 nanocomposite system.*

4.3 In–situ heating of the nanocomposites

Both the matrix and the size of the nanoparticles decide the functionality of the nanocomposites. Temperature is one of the most important factors which affects the size of the nanoparticles and the structure of the host matrix in the nanocomposites [58]. The melting point of free nanoparticles is size dependent and is much lower than the bulk melting temperature (Au = 1064 °C, Ag = 962 °C and TiO_2 = 1640 °C) [201]. Although the particle coarsening and the mechanism is known [202], we study the effect of temperature on the nanocomposite morphology as a whole, i.e., nanoparticle in a host matrix. In this work we applied in–situ TEM heating to have a comparative study with the SHI irradiation in regard to the particle morphologies and the changes in the matrix. In both the cases, an in–situ heating holder as described in chapter 3 has been used to heat the nanocomposites up to

500 °C at a heating rate of 5 °C per minute. At intermediate temperatures, imaging and associated SAED patterns were taken.

4.3.1 Au–TiO_2 nanocomposites

The effect of temperature on the nanocomposites of Au–TiO_2 have been studied by in–situ heating. During the process, at intermediate temperatures of 100 °C, 200 °C, 300 °C, 400 °C

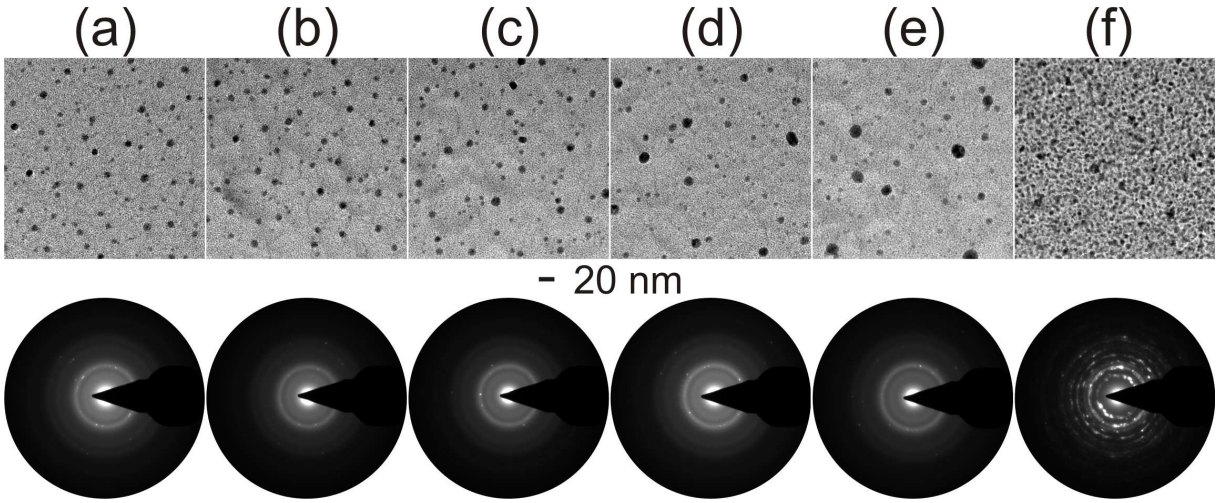

***Figure 4.30*:** *In–situ heating of the 11 % MVF Au–TiO_2 nanocomposites at (a) room temperature (b) 100 °C(c) 200 °C, (d) 300 °C, (e) 400 °Cand (f) 500 °C (total time 3 hrs).*

and 500 °C imaging and SAED patterns were recorded. At room temperature as already discussed, the bimodal particle size distribution is observed. Until the temperature of 400 °C, there is a growth of the large nanoparticles with an accompanied decrease in their number. Additionally, the marginal decrease in the number of smaller nanoparticles is also observed.

Generally, the driving force for the Ostwald ripening or particle coarsening is the surface energy reduction experienced as the surface area of the new nanoparticle is less than that of the sum of the surface areas of the original two nanoparticles. However, this driving force decreases with increasing nanoparticle size. During the particle coarsening process, the nanoparticles tend towards a more stable structure displacing the defects and releasing internal stresses. Particle coarsening in the case of the large nanoparticles on the surface is through surface diffusion. For the small nanoparticles in the matrix, volume diffusion occurs. In both the cases the kinetics are different, but cannot be separately observed.

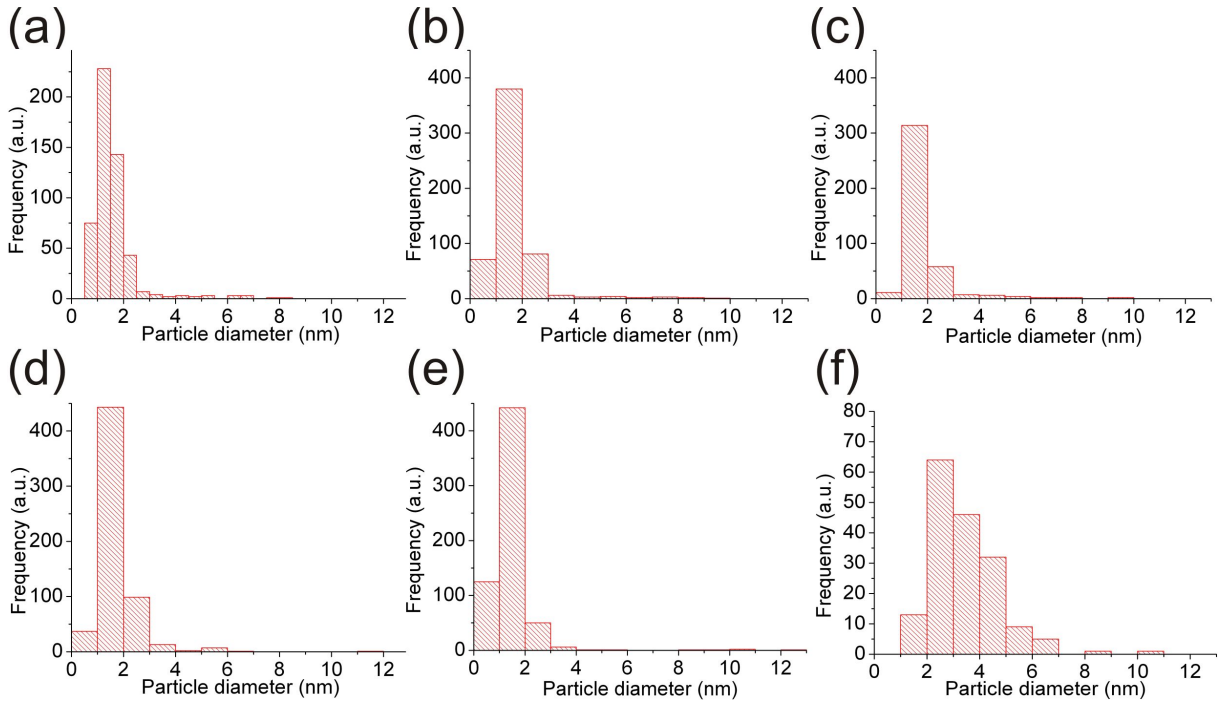

Figure 4.31: *Particle size distribution of the Au–TiO_2 nanocomposite in Fig. 4.30 at (a) room temperature (b) 100 °C(c) 200 °C, (d) 300 °C, (e) 400 °Cand (f) 500 °C (total time 3 hrs).*

The particle size distribution of the TEM micrographs in Fig. 4.30 are shown in Fig. 4.31. Marginal nanoparticle growth is evident from the particle size distributions in Fig. 4.31 from room temperature to 500 °C. The diffuse intensities from in the SAED patterns at 300 °C correspond to the reflections from Anatase form of crystalline TiO_2. These reflections become clearly visible at 500 °C with the development of ring pattern from these reflections. This remains the same even after cooling to the room temperature. The change in the particle size distribution resulting from the change in the structure of the matrix is also evident as the kinetics for the particle coarsening differ in the crystalline matrix. Thus, Au nanoparticle coarsening and the transformation of the matrix from the initially amorphous TiO_2 into crystalline TiO_2 with Anatase structure takes place during in–situ heating. Similar changes were also observed in the case of the Ag–TiO_2 nanocomposites as will be discussed in the next sub–section.

4.3.2 Ag–TiO_2 nanocomposites

The variation in the morphology of Ag nanoparticles in the Ag–TiO_2 nanocomposites upon in–situ heating is shown in Fig. 4.32, where at intermediate temperatures of 150 °C, 300 °C, 400 °C and 500 °C, imaging and associated SAED patterns were collected. At room temperature, as already discussed (section 4.1.1), bimodal particle size distribution is observed.

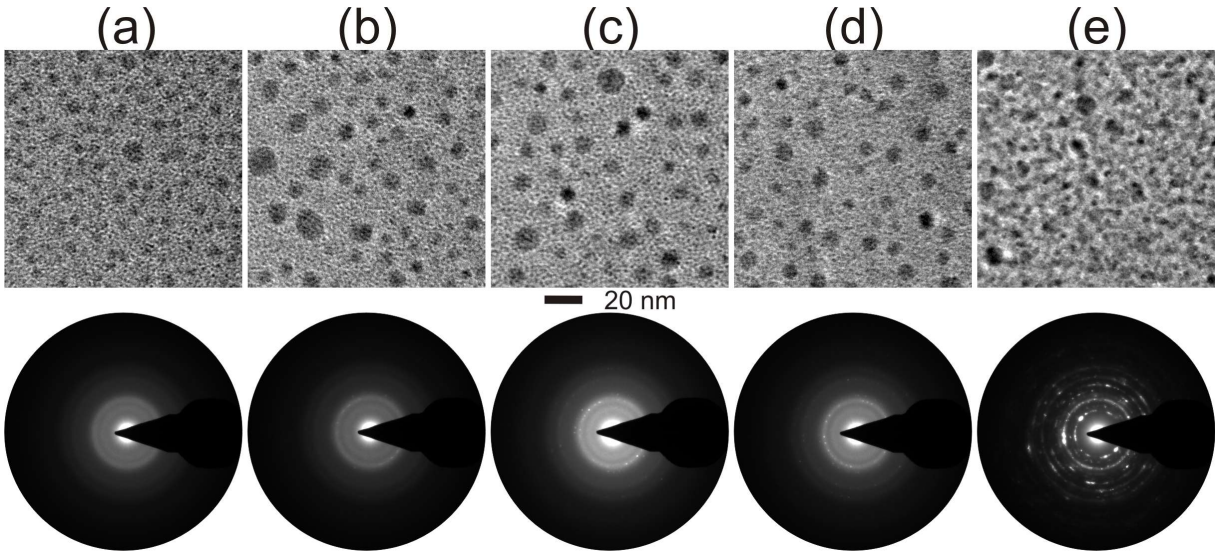

Figure 4.32: *In–situ heating of the Ag–TiO_2 nanocomposites at (a) room temperature (b) 150 °C, (c) 300 °C, (d) 400 °C and (e) 500 °C (total time 3 hrs).*

On in–situ heating, from room temperature to 500 °C, there is an increase in the size of the nanoparticles due to Ostwald ripening, similar to the case of the Au–TiO_2 nanocomposites. Additionally, evidence for the changes in the matrix at 500 °C is also observed through the SAED patterns. Although signatures for the change in the matrix are evident right from 300 °C through the diffuse intensities corresponding to the reflections from the Anatase form of TiO_2, at 500 °C these appear as ring patterns confirming the crystallization of TiO_2 into Anatase type. The sharp transition in the particle size(Fig. 4.32(e)) is a result of the crystallization of TiO_2 inducing a change in the kinetics of the ongoing diffusion processes. Thus similar results as in the case of Au–TiO_2 system were also observed in this case.

4.3.3 In–situ heating vs SHI irradiation

Both the processes of in–situ heating and SHI irradiation are carried out in ultra high vacuum conditions. In contrast to the SHI irradiation, during in–situ heating, as one approaches 500 °C, from the selected area diffraction studies, there is a transformation of the amorphous TiO_2 matrix into a crystalline Anatase–type, but no nanostructures of TiO have been observed. Hence only through SHI irradiation, one can obtain the formation of TiO nanostructures either in the form of large crystals or fragments in the nanocomposites. In both the cases of Au and Ag nanoparticles in TiO_2, upon irradiation, nanoparticles with very small size tend to dissolve and re–precipitate with other nanoparticles in order to minimize the total surface free energy. Since the interparticle spacing between the smaller nanoparticles is very small, they might agglomerate to form larger nanoparticles. The location of the nanoparticles, thereby the morphology of the nanocomposites is pivotal to understand the observations, which involves a number of tomographic experiments. In the case of SHI irradiation, the change in the particle size is higher than that is observed through in–situ heating. The other possible way to understand the results from SHI irradiation is that the SHI creates a molten zone as expected from the thermal spike model [82], transiently (for picoseconds) of a few nm in which the atoms from the surface region of the particles desorbed and diffuse in the matrix. The creation of a cylindrical zone (referred to as ion track) following the passage of ion in insulting matrix and the formation of ion track is well known and has been explained by thermal spike and Coulomb explosion model [26]. In the region where the interparticle distance is very small, the particles agglomerate to form bigger particles by diffusion of small clusters as can be seen from both the systems of Ag–TiO_2 and Au–TiO_2. In earlier work, Biswas et al. [203] studied the effect of SHI irradiation on Au and Ag polymer nanocomposites depicting the coalescence of nanoparticles with SHI irradiation. In this work, tuning the SPR without varying the MVF is possible by using the SHI irradiation. It has been shown that by using Ag (13 % to 27 %) and Au (7 % to 15 %) based nanocomposites with a TiO_2 matrix along with SHI irradiation, it is possible to tune the SPR from 485 nm to 687 nm.

Chapter 5

Polymer based nanocomposites

Metal nanoparticles embedded in polymer matrices have been a subject of extensive research due to their potential applications [11]. Development of nanocomposites in which the SPR is tunable has also attracted sustained interest [39, 51, 96, 204]. A detailed understanding of their optical properties is of interest from both fundamental and technological point of view. The development of techniques for the synthesis of monodisperse nanoparticles of desired size and size distribution has been a major challenge over the years. Several physical and chemical techniques are used to prepare metal nanoparticles embedded in various dielectric matrices such as ion implantation [205], co–sputtering [65], sol–gel approach [206], spin–coating [207], co–evaporation [50], cluster deposition [208], flame synthesis [209], and other chemical synthesis methods [12, 210]. This chapter deals with the synthesis and characterization of noble metal (Ag and Au) nanoparticles embedded in a PTFE matrix using co–sputtering from two independent sources. Also, multi–layered nanocomposites and the studies pertaining to the respective irradiation are carried out and discussed.

5.1 Synthesis of Ag-PTFE nanocomposites

As discussed in the section 3.1.1, nanocomposite coatings were prepared by co–sputtering of PTFE and silver from two different magnetron sources simultaneously in a home–made

deposition chamber under high vacuum (10^{-7} mbar) conditions. The thickness of the coating was measured by a surface profilometer (Dektak 8000). The films were deposited on a silicon wafer, TEM grid and glass substrates and their thickness was maintained approximately below 35 nm (section 3.1.1). The MVF was determined by using an EDX (section 3.2.1.1). The morphology of the nanoparticles has been studied with a transmission electron microscope, Philips–CM30 (section 3.6). Optical extinction studies were carried out by using the UV–Vis/NIR spectrophotometer (Perkin Elmer Lambda 900) as discussed in section 3.14. After sputtering the polymer is highly crosslinked, the structural description of the cross–linked polymer was discussed in previous doctoral works from the group [211,212]. Ag co–sputtered with Teflon does not wet the polymer surface around but forms three–dimensional clusters (Fig. 2.1.2). Through the process of co–sputtering, when the MVF is increased, an interplay between the particle morphology and the interparticle spacing exists. Fig. 5.1 shows that the average particle size increases from ∼4 nm to ∼14 nm with an increase in the MVF from 9 % to 33 %.

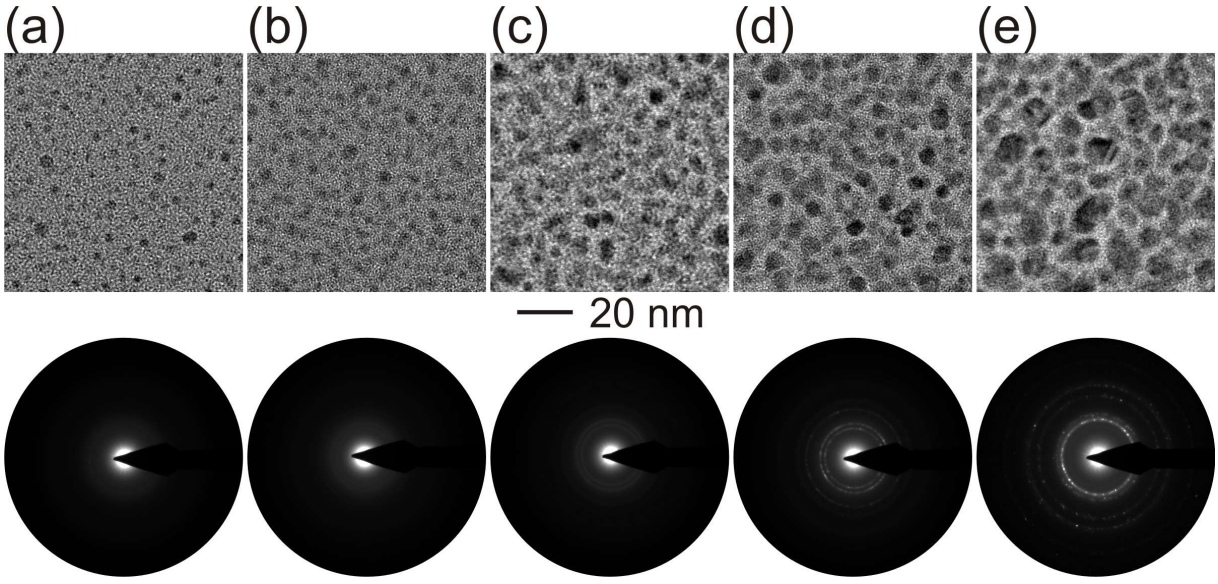

***Figure 5.1*:** *TEM images showing the increase in MVF (a)9 % (b)14 % (c)21 % (d)26 % to (e)33 %. One can observe the increase in particle size and decrease in the interparticle spacing.*

5.2 SHI induced modification of PTFE based nanocomposites

The study of ion irradiation of nanocomposite systems provides a unique opportunity to understand the physics of ion interaction with nano–dimensional systems. In this work the Ag–PTFE nanocomposites were subjected to irradiation with Ag^{8+} ions. The corresponding simulations from SRIM based on the ion energy with respect to the electronic energy loss is shown in the Fig. 5.2 [92].

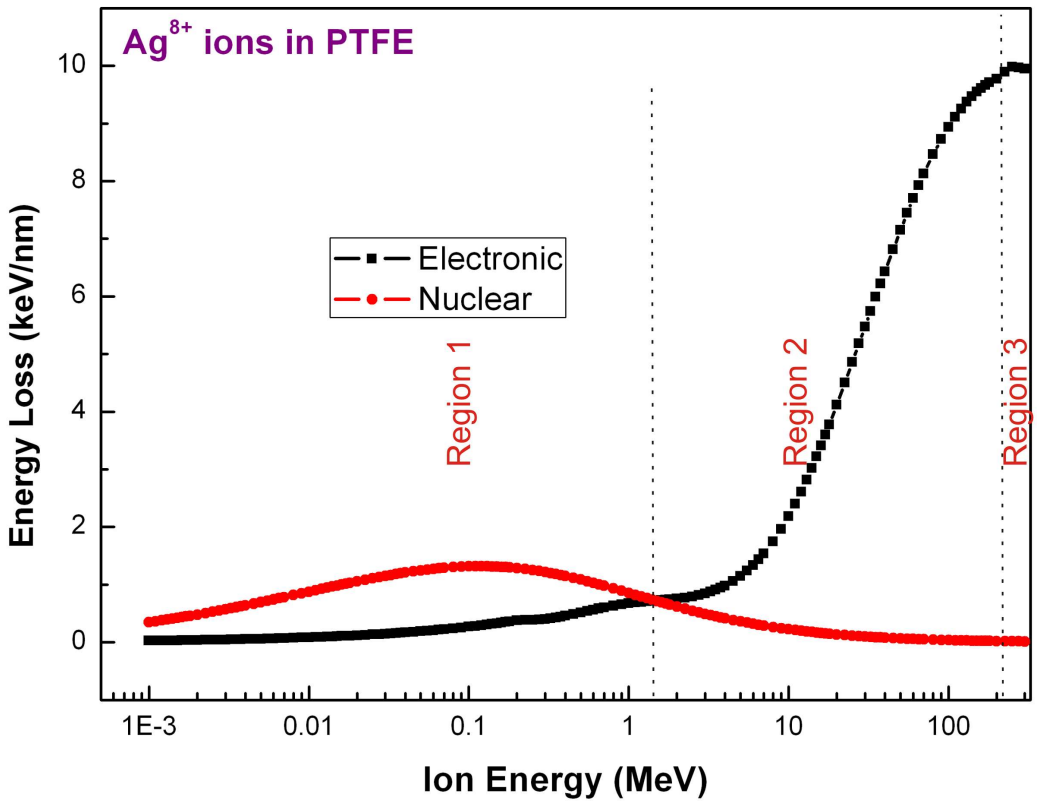

Figure 5.2: *SRIM simulation showing the plot of electronic energy loss vs ion energy for Ag ions in PTFE [92].*

The variation of the energy loss of the ions respective to the energy of the ions is shown in Fig. 5.2. The stopping power consists of two components, (i) nuclear, region I (section 2.2.2.1) and (ii) electronic stopping power, region II + III (section 2.2.2.2). At low energies (1 keV/nucleon), the nuclear energy loss predominates. At higher energies

(1 MeV/nucleon), where the velocity of the ions is comparable with the Bohr velocity of the orbital electrons, the Ag^{8+} ions interact with the electrons of the target atoms resulting in the ionization of the target atoms and/or transfer of electrons to higher energetic states (inelastic collision). Since the mass of the ions is much higher than the mass of the electrons, the initial direction of the ions in the solid remains almost unchanged. In the case of nanocomposite system, at high MVF, since the stopping power of metals is very high, the energy loss will be much more when compared with the low MVF and pure PTFE systems.

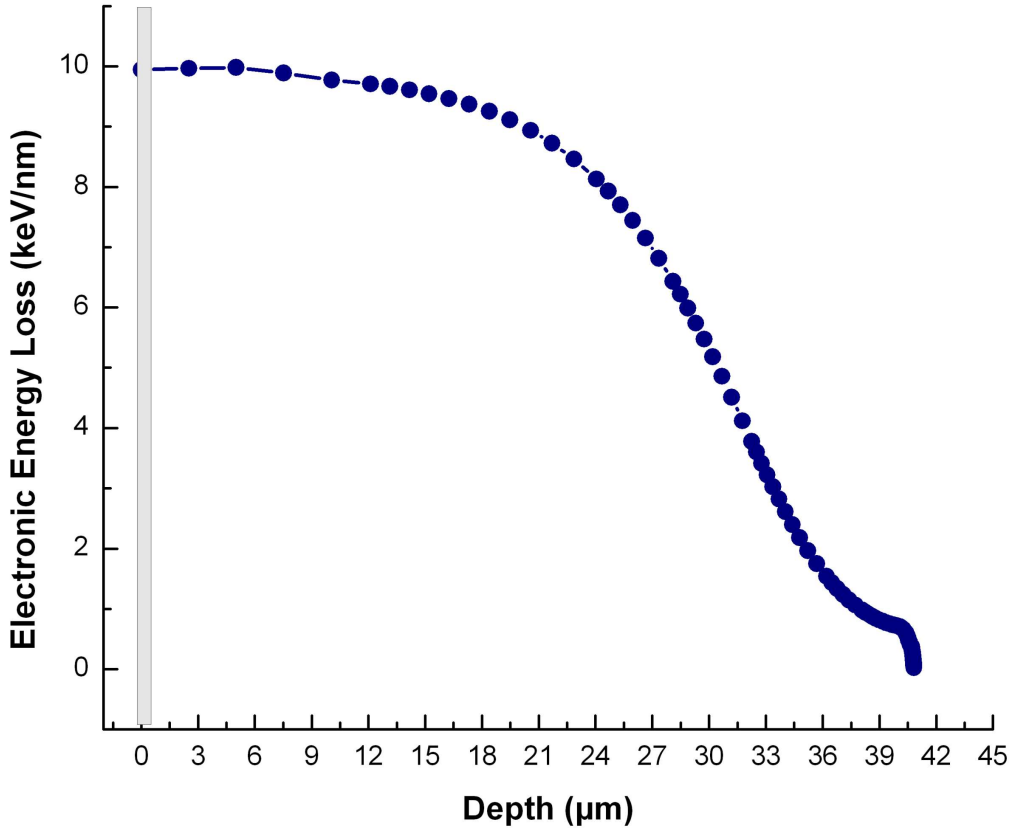

Figure 5.3: *S_e versus depth plot for 100MeV Ag^{8+} ions in PTFE. The grey region depicts the sample thickness used in this work [92].*

The variation of energy loss versus penetration depth for 100 MeV Ag^{8+} ions in PTFE is shown in Fig. 5.3. The energy loss phenomenon is statistical in nature as the collisions between projectile ions and target atoms are random. All ions penetrating the solid do not have the same penetration depth, but there is a distribution along its path called longitudinal straggling. Since each successive collision of projectile ion with target atoms leads to a deviation from its straight line path resulting in a straggling in lateral direction called lateral

straggling. The projectile ions continuously lose energy and finally come to a stop, which is called as projected range or penetration depth.

Nanoparticle synthesis using physical vapor deposition results in the formation of nanoparticles with a certain size depending on the MVF. For a particular MVF, the obtained size of the nanoparticles is fixed. At this MVF, the size of nanoparticles can further be enlarged by heat treatment. Here, the SHI beam irradiation is used as a tool to tune the particle size for a given MVF based on the SHI fluence. The effect of SHI irradiation on the size and size distribution of Ag nanoparticles embedded in a PTFE matrix and the resulting changes in the optical properties were studied. Indications of a marginal reduction in the size of nanoparticles by ion fluence from 100 MeV Ag^{8+} ions have been observed. Thin nanocomposite films on glass and TEM grids were irradiated by 100 MeV Ag^{8+} ions at a fluence of 3×10^{11}, 6×10^{11} and 1×10^{12} ions/cm^2 delivered from the 15UD Pelletron accelerator at IUAC. The UV–visible absorption spectra of pristine and irradiated films were recorded using a UV–Vis spectrophotometer. The microstructural morphology of the films that were deposited on carbon coated copper TEM grids were investigated with a transmission electron microscope, Philips CM30.

Fig. 5.4 shows the optical extinction spectra of the pristine and irradiated Ag–PTFE nanocomposite films. The SPR band at 420 nm in case of the pristine sample (a) is a clear signature of formation of Ag nanoparticles during sputtering (section 2.3). As these nanocomposite films are irradiated with 100 MeV Ag^{8+} ions, the SPR peak broadens and a red shift is observed. With increasing ion fluence, the broadening and the shift of the SPR peak becomes prominent. An increase in full width at half maximum (FWHM) and a red shift of 10 nm from 420 nm to 430 nm are observed after irradiation up to a fluence of 1×10^{12} ions/cm^2. The broadening in SPR absorption band after ion irradiation indicates a reduction in the nanoparticle size and a change in the number density of the nanoparticles. One explanation for the observed red shift is due to the morphological changes in the nanocomposites and also due to modifications in the polymer matrix induced by ion irradiation.

Transmission electron micrographs of the pristine and irradiated samples are shown in

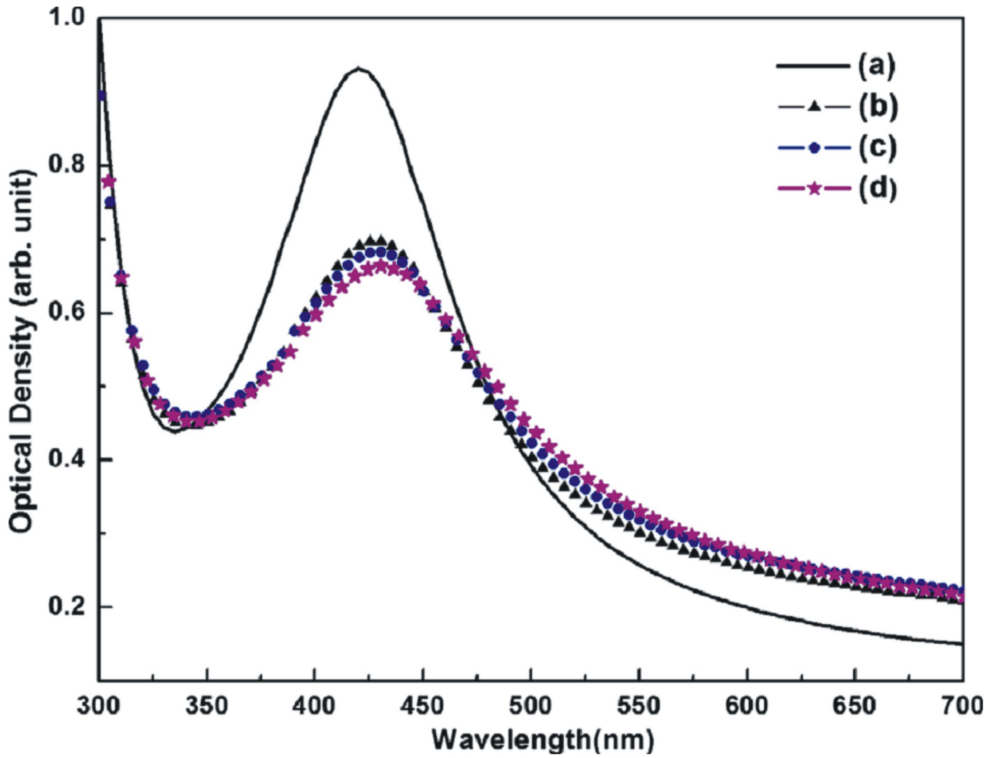

Figure 5.4: *Extinction spectra (a) for pristine and (b)to(d) for irradiated samples at fluences of* 3×10^{11}, 6×10^{11} *and* 1×10^{12} *ions/cm*^{2} *respectively, delivered by 15UD Pelletron accelerator at IUAC.*

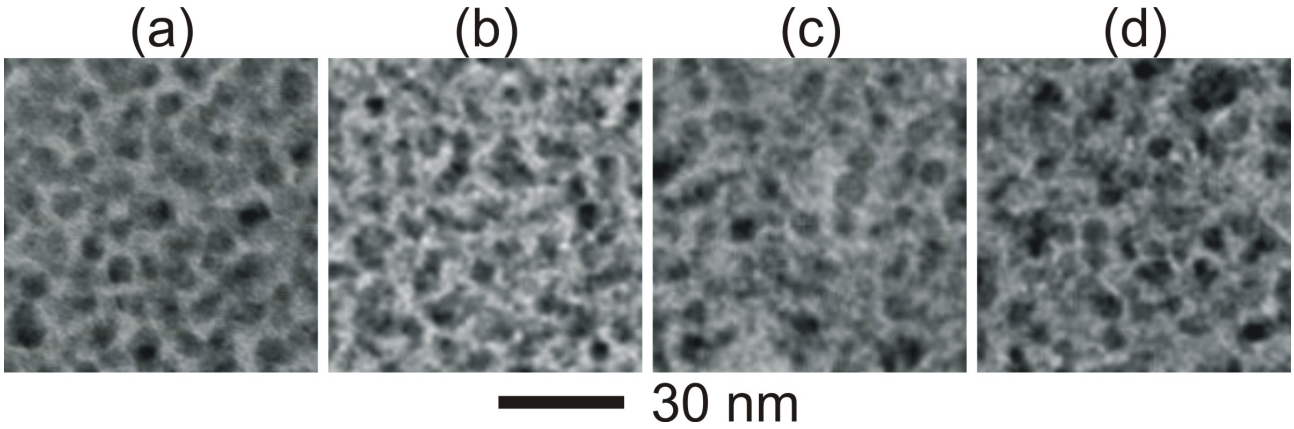

Figure 5.5: *Transmission electron micrographs of (a) pristine and irradiated samples at fluences of (b)* 3×10^{11}, *(c)* 6×10^{11} *and (d)* 1×10^{12} *ions/cm*^{2}.

Fig. 5.5. The average particle diameter (D) of nanoparticles in case of the as–deposited film is about 4.4 nm (Fig. 5.5a). A marginal decrease in the nanoparticle size from 4.4 nm to 3.3 nm is observed after irradiation at a fluence of 1×10^{12} ions/cm^2 from the corresponding size distribution in Fig. 5.6. Particle size distribution were calculated by drawing lines across

the smallest diameter of the nanoparticles from the representative TEM images. It has been observed that the sizes of the nanoparticles marginally decrease with increasing ion fluence. The presence of some larger Ag nanoparticles can also be seen (Fig. 5.5(c) and 5.5(d)) after irradiation. One explanation for the observed change is due to the agglomeration of a few small Ag nanoparticles during ion irradiation. The passage of SHIs deposits the electronic energy into the Ag-PTFE system. The pristine film has particles with a certain size distribution along with some Ag atoms in the atomic state itself. Similar to the diffusion of clusters and atomic species within the ion track [213], the diffusion of some Ag atoms and smaller particles to bigger particles leads to ripening of Ag nanoparticles around the ion path due to thermal spike produced by the ions for a transient duration of time. In case of Figs. 5.4(c) and (d), the contribution of the larger Ag nanoparticles to SPR have to be ignored as their number is relatively less than their counterparts. Marginal decrease of the particle size is observed through SHI irradiation using ion fluence as the controlling parameter.

As the ions pass through matter, they lose their energy by electronic (S_e) excitations (inelastic collisions) and nuclear (S_n) collisions (elastic collisions). S_e is dominant at higher energies of irradiating ions, i.e., when the velocity is comparable to the Bohr velocity, like in the present case. The energy that is lost by the irradiating ion (100 MeV Ag^{8+}) is absorbed by the Ag–Teflon nanocomposite matrix, which leads to a change of its properties. The irradiating ions deposit an energy of $S_e = 12.2$ keV/nm in the nanocomposite film through in–elastic collisions, as estimated from the SRIM simulations [92]. With such a high energy deposited in the system, the surface atoms of the Ag nanoparticles can gain sufficient energy higher than their binding energy with the nanoparticles, resulting in migration of surface atoms, which leads to the dissolution of the nanoparticles. Particles with very small size can agglomerate with other nanoparticles in order to minimize their surface free energy. Both the process of migration of atomic species from nanoparticles and Ostwald ripening can result in the observed size distribution (Fig. 5.6). The other possible way is that the ion creates a molten zone as expected from the thermal spike model [87], transiently (picoseconds) of a few nm in which the atoms from the surface region of the particles desorb and diffuse in the matrix. The creation of a cylindrical zone following the passage of the ions in the PTFE matrix and the formation of ion track is well known and has been explained

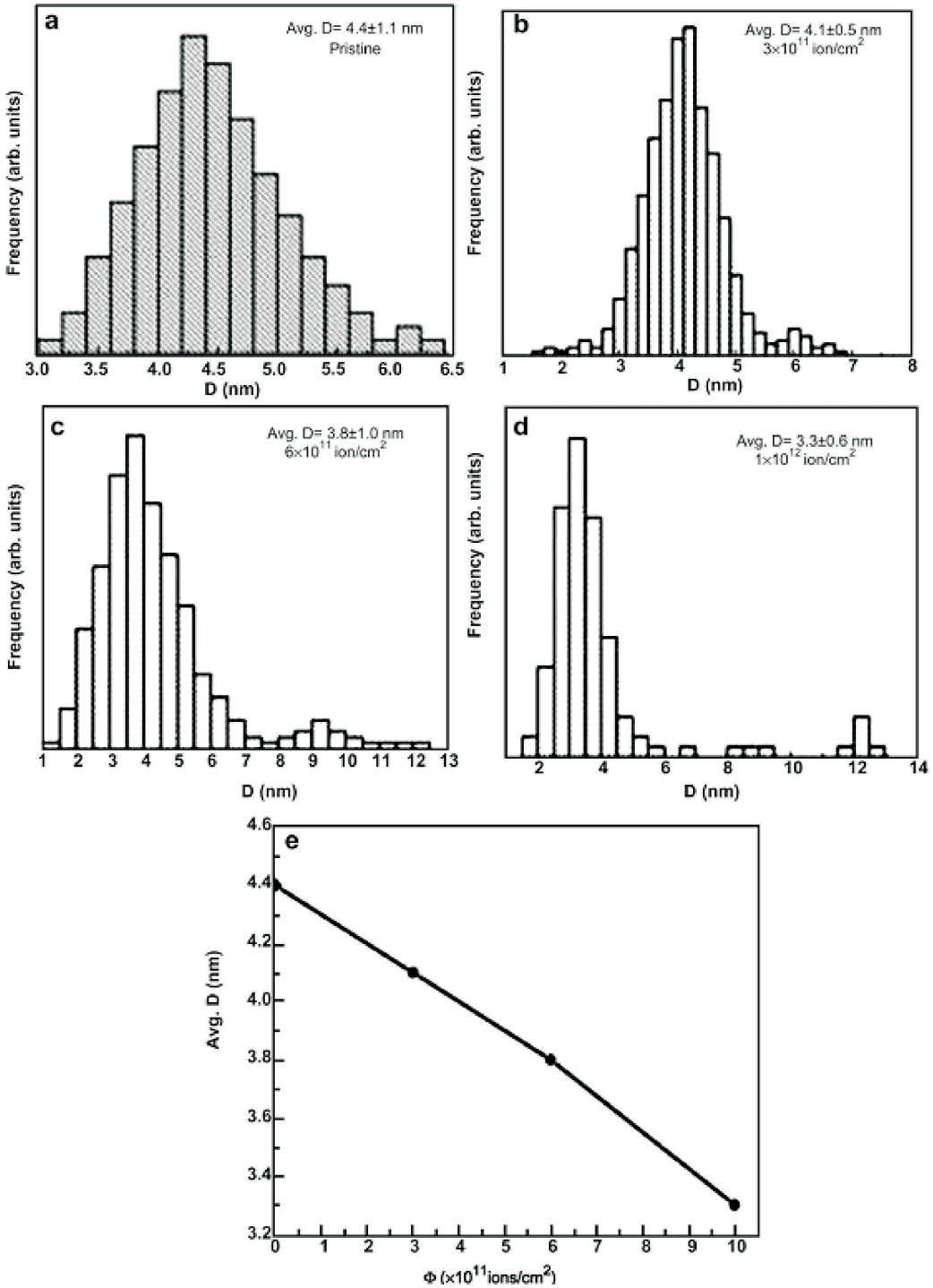

***Figure 5.6*:** *Size distribution Ag nanoparticles before and after ion irradiation. (a) Pristine and irradiated samples at fluences of (b)* 3×10^{11}*, (c)* 6×10^{11} *and (d)* 1×10^{12} *ions/cm*^{2} *respectively. (e) shows the variation of particle size D, with ion fluence.*

by the thermal spike and Coulomb explosion models [82, 90]. In the region where the interparticle distance is very small, the particles can agglomerate to form a bigger particles by diffusion of small clusters [213]. The increase in FWHM in optical absorption spectra (Fig. 5.4) of the irradiated nanocomposites reveals the marginal changes in the size which is in agreement with the microstructural results from the TEM (Fig. 5.6). This occurs because of the large electronic energy (12.5 keV/nm) deposited into the nanocomposite system by SHI irradiation. Since it is well known from the theoretical calculations [35, 214], that the SPR peak position strongly depends on the shape and the size of the nanoparticles as well as on the refractive index of the surrounding matrix, this SPR shift after ion irradiation can be accounted from an interplay of SPR from the dissoluted small and the agglomerated large Ag nanoparticles, the changes in matrix and the modification of the chemical interface surrounding the nanoparticles or a combination of the aforementioned factors (Fig. 5.4.

The study of the particle size distribution from the TEM micrographs of the pristine and irradiated samples show that there is a marginal decrease in particle size by varying the ion beam parameters. Additionally, SHI irradiation causes stoichiometric changes in the polymer, which results in changing the dielectric properties of the polymer matrix. Polymer matrices are very sensitive to ion irradiation, because on irradiation with energetic ions structural modifications occur [81, 215]. Lighter elements like hydrogen may evaporate resulting in an increase in film density, which leads to changes in the refractive index of the polymer. Evolution of gases takes place through these cylindrical zones (paths of the ions) referred to as ion tracks in the polymer [216]. The passage of ions through the polymer causes electronic excitation of constituent atoms, followed by breaking of bonds of the type C–C and C–F in PTFE. Thus an incident ion along its path releases a number of fluorocarbons and fluorine as observed by Prakash et al. [217]. The reactions occur within the ion tracks created in PTFE by the ions passing through the system. Due to emission of fluorine and fluorine–rich fluorocarbons from PTFE, it turns into a carbon rich structure. This suggests that evolution of various fluorocarbons and loss of fluorine with increasing fluence leads to graphitization and carbonization [217]. In the case of Ag–PTFE system, at higher fluences of 3×10^{12} ions/cm^2, in low magnification TEM images, one can observe the carbon rich amorphized regions that are the result of the SHI irradiation at high fluences(Fig. 5.7). This

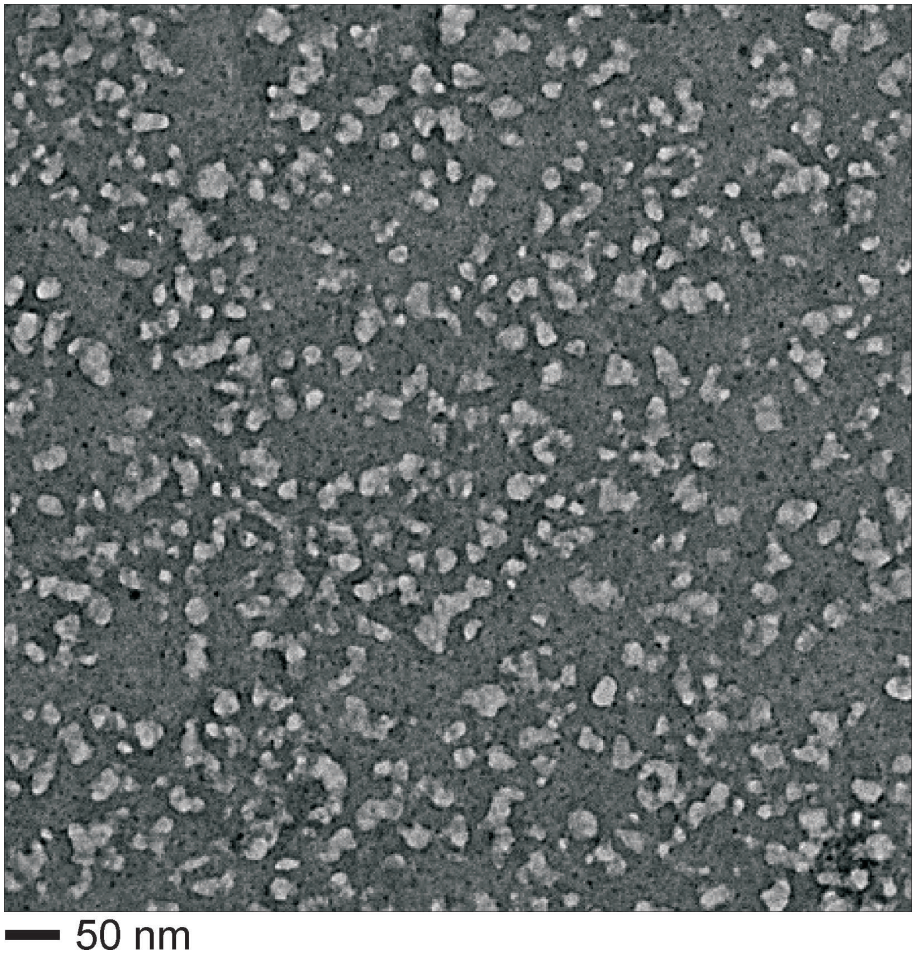

***Figure 5.7*:** *SHI irradiation induced changes in the PTFE matrix of the nanocomposite along the ion tracks.*

might be as a result of the carbonization along the ion tracks as has been reported previously in different polymer matrices [33, 213]. The aggregation and the densification of carbon rich areas along the ion path might be a result of independent and simultaneous diffusion processes taking place in the transient molten state of the latent tracks. It is known that the electronic energy loss of typically a few keV/nm is adequate to create columnar defects in polymers [81, 82]. Hence, it is expected that each incident ion will create a columnar defect in the entire thickness of the polymer layer [81, 200]. According to the study by Mock et al. [190], in Ag nanoparticles, 1.6 nm red shift per 0.01 increase in refractive index. Hence, SHI irradiation leads to carbonization of the matrix, which also contribute to an alteration in the plasmonic properties of nanocomposites.

5.3 Synthesis and properties of bimetallic nanocomposites based on sandwich geometry

When two metals are combined, the optical properties are governed by a combination of the properties (dielectric functions) of both metals. Such a combination strongly depends on the arrangement of the metallic clusters in that geometry. This can be either an alloy [218], a perfect or a quasi core–shell [219–221] or a geometry based effect. Bimetallic nanoparticles of various metallic combinations fabricated by various wet chemical and physical deposition techniques have been studied by several groups [103,222–225] with a focus on the study of the optical properties or on their catalytic or biological applications. In all cases the interaction of the metals plays a vital role in optical nanocomposites for the creation of equal intensity double plasmon resonance (EIDPR). In this context, silver and gold have attained a huge interest. A combined advantage of the chemical stability from gold and a higher signal–noise ratio from silver results in tuning the optical response to form two clearly separated plasmon peaks which is a challenge for the demanding applications like sensors based on surface plasmon resonance [226]. However, such an effect of double plasmon resonance is difficult in the case of Au and Ag because of their nearly identical bulk lattice constants and the resulting mutual miscibility [227]. As a result, an optical response shows the absence of double plasmon peaks so that one peak or seemingly two peaks is shown in the extinction spectra by most of the researchers [218, 220], due to difficulties in the synthesis [220]. In spite of the results from Mulvaney et al. [223] and Link et al. [103] on the generation of two plasmon absorption bands, mostly, one of the absorption bands is in the form of a shoulder peak. Also, Ung et al. [98], studied the optical properties of Au particles based on varying the shell thickness by chemical routes achieving a change in the single plasmonic peak for disordered Au particle films. In addition Malikova et al. [228], studied the effect of layer–by–layer assembly with the mixed particles of gold and the associated interparticle interactions.

Here, a strategy based on vapor phase deposition methods to develop well separated plasmon peaks (i.e., EIDPR) using arrangements of nanoparticles in sandwich geometry for

engineering the plasmon resonance. The excitation and decay of the plasmon responses is controlled by the plasmon sequences based on the geometric effect; the amount of metals at a fixed separation distance and varying the separation thickness at fixed amount of metal. In this case, vapor phase tandem deposition was employed to synthesize quasi two–dimensional nanocomposites of Teflon AF–Ag and Teflon AF–Au. Distinct double plasmon resonance absorption maxima were obtained from such sandwich structures. The evolved systems are capable to engineer the double plasmon resonance by tailoring the amount of metallic nanoclusters and the dielectric separation layer at different wavelengths, originating from two optically active layers. The approach used here to prepare the sandwich structures involves four consecutive steps: evaporation of Teflon AF (TAF), deposition of metallic particles of one type, second evaporation of TAF and finally the deposition of metallic particles of another type, using vapor phase evaporation.

In sandwich geometry as shown in Fig. 5.8(a), three cases were studied: firstly by sandwiching Au and varying the amount of Ag on top; secondly by sandwiching Ag and varying the amount of Au on top; and thirdly by keeping the amount of Ag and Au constant and varying the dielectric barrier thickness (TAF). In the first case, 0.6 nm of Au has been sandwiched between 3.3 nm of TAF layers, followed by varying the amount of Ag on the top from 0.6 nm to 1.8 nm. In the second case, 0.6 nm of Ag has been sandwiched between 3.3 nm of TAF layers, followed by varying the amount of Au on the top from 0.6 nm to 2.7 nm. Thirdly, on the 3.3 nm TAF, keeping the 0.6 nm of Ag and 2.7 nm of Au as constant, the dielectric barrier layer thickness in between the metallic clusters was varied from 1 nm to 6.6 nm.

Near–field interactions between closely spaced metal nanoparticles resulted in fascinating properties, absent in the case of individual nanoparticles [183]. When two plasmon resonant particles are brought close, the plasmon modes in the individual nanoparticles can interact, leading to resonances from the coupled system [184]. A near electromagnetic field between two metallic surfaces placed at a short distance presents a large change compared to an isolated surface, which appears promising for applications such as nanosensors and surface enhanced Raman spectroscopy (SERS) for molecular detection [229].

Most of the research was directed towards the investigation of lateral–to–surface dimensions [230]. However, it is more interesting to investigate the perpendicular–to–surface direction, a type which is well known for the dipole/surface interaction [231]. Additionally, tailoring the separation between the nanoclusters in the Z–direction of the sandwich geometry could be very useful for applications in nanooptics like SERS [232], nanosensors based on surface plasmon resonance (SPR) [233] and nanocapacitors [234, 235] where the polymer as a dielectric barrier would determine the effective capacitance of the system [220].

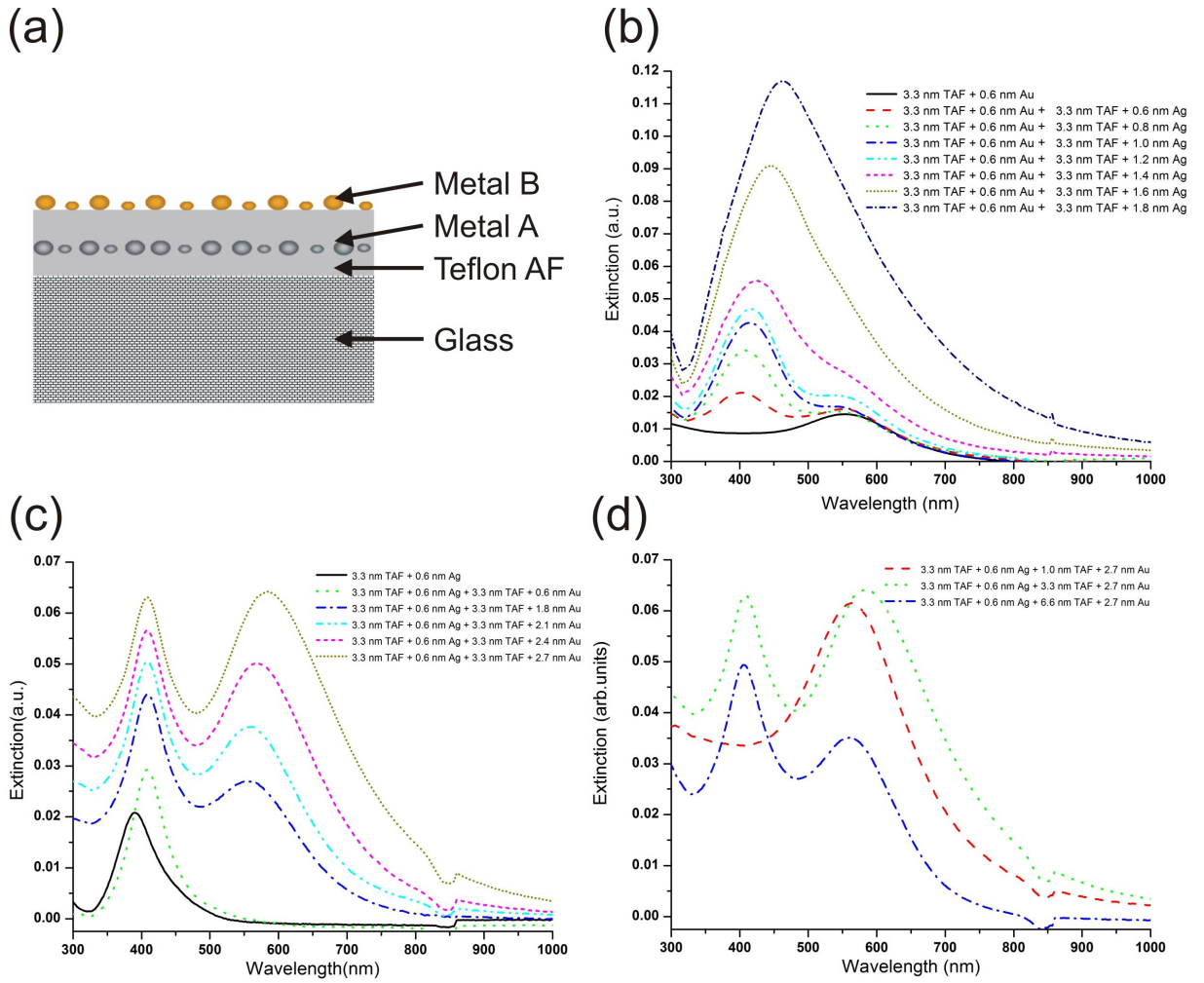

Figure 5.8: *(a) sketch of the sandwich structure. The extinction spectra (b) showing the increase in the amount of Ag on a sandwich of 0.6 nm Au sandwiched between 3.3 nm of Teflon AF, (c) showing the increase in the amount of Au on a sandwich of 0.6 nm Ag sandwiched between 3.3 nm of Teflon AF and (d) showing the increase in the amount of Teflon AF sandwich layer, from 3.3 nm to 10 nm, between 0.6 nm of Ag and 2.7 nm of Au.*

The optical properties of the geometry in Fig. 5.8(b), where Au (0.6 nm) is sandwiched and the amount of Ag is varied, are shown in Fig.5.8(b). Initially a particle plasmon peak (PPP) maximum from the sandwiched Au at 550 nm is observed. On deposition of 0.6 nm of Ag, an Ag PPP develops at 402 nm. Further increasing the amount of Ag, increases the red–shift of the Ag PPP and its intensity, which is accompanied by submergence of the sandwiched Au PPP. Additional increase of the amount of Ag leads to a further shift, broadening of the PPP and quasi–disappearance of the Au PPP shoulder, as shown in Fig. 5.8(b). Increasing the amount of Ag in turn nucleates additional Ag on the top of already deposited Ag nanoclusters (nucleation sites), which leads to the increase in the size of the nanoclusters, and thus the red–shift of the plasmon peak.

However, interesting results are observed in the opposite case shown in Fig. 5.8(c). The PPP maximum from the sandwiched Ag is at 390 nm. The initial deposition of Au causes the development of a shoulder Au PPP. Further increasing the Au amount, we notice the clear development of the PPP of Au with a shift from 556 nm to 584 nm. Similar to the case of Au sandwich, the newly deposited Au nucleate on the already existing Au nanoparticles which leads to the increase in the size of the nanoclusters and thus the red–shift of the plasmon peak. This size dependence effect is shown by the TEM images in Fig. 5.9.

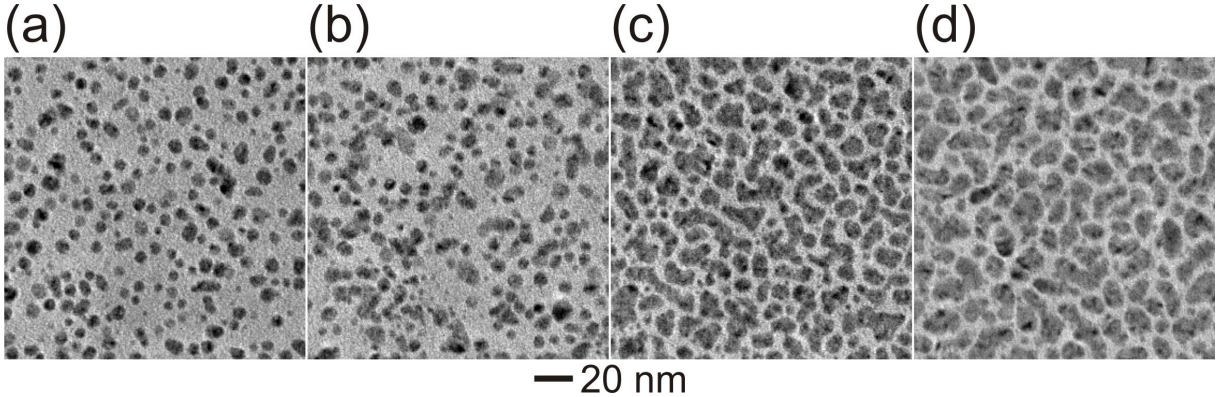

***Figure 5.9*:** *TEM images of 0.6 nm of Au sandwiched between 3.3 nm of Teflon AF and (a) 0.6 nm gold, (b) 1.8 nm gold, (c) 2.1 nm gold and (d) 2.4 nm gold on the top. The amount of Ag and Au are also confirmed by the attenuation in the signal from XPS studies.*

Surprisingly, the development of the Au PPP does not affect the Ag PPP, but rather results in equal intensity double plasmon resonance [100]. In addition, the TEM images in

Fig. 5.9(a) and (b) show the presence of nanoparticles. Differences between the Au and Ag cannot be observed from the diffraction patterns through the differences in the d–spacings as they have similar d–values. On increasing the amount of metallic content at the top, the possibility to distinguish between them becomes difficult because of percolation.

It is well known that the position of particle plasmons in bimetallic materials has a great influence on the overall plasmonic properties. In this work, we believe that the intensity increase and the broadening are not only determined by the well known factors like size and shape effects, but also accompanied by the submerged Au PPR and its decay. The damping of the plasmon resonance is thus determined by the energy relaxation time. The energy relaxation of a plasmon oscillation is composed of a non–radiative decay channel and radiative decay channel. It is well established that the decay channel of a surface plasmon resonance from a metallic nanoparticle is size dependent. In the case of size in the range 5 nm $<$ D $<$ 30 nm, plasmon decay is due to the non–radiative processes whereas by D $>$ 30 nm radiative processes are dominant [236]. A strong damping of the plasmon resonance for gold nanoparticles is determined theoretically and experimentally to be in the range between 500 nm and 700 nm, whereas for silver nanoparticles it is between 320 nm and 630 nm, with a decay time of 2–4fs [237]. In this regime there is a competition between the plasmon excitation and d–sp interband (Au = 500 nm, Ag = 320 nm) absorption preventing efficient plasmon oscillation. In our result, as observed in the case of Ag sandwich geometry, the plasmon peak from the sandwiched Ag occurs at $\lambda = 390$ nm and remains at a constant position far away from the competition between the plasmon excitation and d–sp interband of gold nanoparticles. Increasing the amount of Au (Fig. 5.9) leads to an increase in the particle size and also the plasmon shifts away from the interband transition towards higher wavelengths. However, as the particle size increases (as observed in Fig. 5.9(c) and (d)), the damping is more radiative in nature, which leads to further red–shift and broadening of the dipole resonance. In this context the red–shift from the Au nanoclusters does not have an impact on the Ag peak position in the optical spectrum, but rather on its intensity, as seen in Fig. 5.8(c). This is because the Ag peak position is at much lower wavelengths than the broadening Au peak resonance as well as its interband transition, which in this case cannot engulf the Ag peak during its red–shift, but rather give a persistent Ag particle

plasmon resonance with increasing intensity by its decay. In the Au sandwich geometry, an increase in the amount of Ag causes a plasmon shift towards higher wavelengths onto the Au interband transition and its plasmon peak position. Also, here a competition exists between the Au plasmon with its interband and the Ag plasmon. Due to the higher intensity plasmon resonance of Ag nanoparticles as compared to that of Au nanoparticles, the decay of the Au plasmon peak is accelerated, which leads to the engulfing of the Au plasmon resonance and a broad single peak.

Indeed, in addition to the geometry and EIDPR, the results clearly show a plasmon sequence effect and visualize a positive or negative role for the decay. Based on this simple strategy and using the aforementioned effects, the creation of EIDPR became plausible. In this context, the separation distance between the two metals will play an important role on the EIDPR behavior. Such effects are distance dependent, as shown in the case of Maier et al. [183], where the lateral distance between two nanoparticles plays a vital role in the optical properties. In our case, one expects the similar behavior, but in the Z–direction. Holland et al. [231] has shown in earlier studies the presence of a critical thickness of a dielectric separation layer for optimum coupling by perpendicular dipolesurface interaction. In analogy, we test this observation in our case. In this case, the amount of Au and Ag are fixed and the thickness of the dielectric barrier is varied. The optical responses, as shown in Fig. 5.8(d), were found to vary with the thickness of the sandwiched dielectric layer, indicating the critical thickness of 3.3 nm of the dielectric layer for optimum EIDPR. In case of 1 nm separation we observed the formation of a single peak which exhibits the same behavior as that in the case without the separation, because of the mixing of the two metallic materials. Indeed an interesting feature in Fig. 5.8(d) is that, by increasing the thickness of Teflon AF from 3.3 nm to 6.6 nm, the extinction intensity decreases along with a blue–shift of the gold plasmonic peak.

It is well known that the intrinsic intensity and confinement of plasmon fields at the surface of noble metal fields is maximum at the nanoparticle surface and decays exponentially away from it. For instance, it was found that a plane wave impinging on a 20 nm diameter Ag particle is strongly "focused" into the particle, leading to a large electric field

density in a 10 nm region around the particle [4]. In this case the Teflon AF thickness is varied within this range where field enhancement is expected, as it was below 10 nm. A qualitative explanation could be established by considering the all layers as one layer. Hence, increasing the TAF thickness is like increasing the amount of dielectric material when compared to the metal part "diluted effect". Accordingly, a reduction in the intensity of the plasmonic response accompanied by a blue–shift is observed. However, this needs more work to fully understand the underlying mechanisms. The tandem deposition procedure employed here, along with the sandwich geometry, allows the analysis of the changes in the optical properties, as well as the selection of the stage at which the procedure should be stopped to achieve the EIDPR. Strong changes in the optical properties occur when the plasmon frequency of one particle is near the plasmon frequency of another particle type, as a result of the dipole–dipole coupling/decoupling. In resonant conditions, when another particle is nearby, upon polarization additional forces act on both the particles [238]. In this case we show how plasmon decay can be used beneficially. The most salient features of these spectra are that special features show up at specific wavelengths, which corresponds to the plasmon resonances of the coupled system under consideration. A dipole moment oriented towards the cluster surfaces is able to create oscillating charges of dipolar origin in the clusters, which drive a strong enhancement [183]. Proximity to nearby metallic surfaces increases the local field and modifies the excitation. In other words, the transfer of energy by coupling/decoupling is possible by the plasma oscillation energy [230].

Chapter 6

Summary

Nanocomposite thin film coatings with a wide range of MVFs were prepared by co–sputtering of TiO_2/Teflon and Ag/Au from two different magnetron sources simultaneously in a home–made deposition chamber under high vacuum (10^{-7} mbar) conditions. Two different types of host materials a polymeric and a ceramic were studied in this work. Morphology, optical and antibacterial properties of these nanocomposites were studied.

The formation of metallic nanoparticles upon vapor phase co–deposition of a metal and a dielectric matrix component can be understood in terms of the high cohesive energy of the metal and the low metal-matrix interaction energy which lead to high metal atom mobility on the growing composite surface and metal aggregation whenever metal atoms encounter each other or a metal cluster. This process, however, never leads to a bimodal distribution of the cluster size and suggests that the larger clusters to be located at the surface. This is opposite to the behavior of Ag and other metal clusters on polymers where surface segregation has never been reported and even embedding of clusters deposited on the surface was seen upon annealing above the surface glass transition temperature. Embedding is favorable for the metal clusters on the polymer because the high surface energy of the metal clusters can be reduced if they are surrounded by the polymer. Elastic distortions do not play any role in the polymer matrix above the softening temperature. In the case of Ag clusters on TiO_2, segregation of the clusters on the surface also provides a fast pathway for Ostwald ripening without any restrictions by elastic distortions at least for those clusters

which are in direct contact with the surface.

Due to the drawbacks of cross–sectional TEM (section 3.2.1.2), the necessity of having information from the third dimension became rather important. Additionally, when analyzing only CTEM images, the MVF cannot be properly related with the TEM images. As the morphology of the nanocomposites plays a pivotal role in understanding the functional properties of the nanocomposite thin films, advanced transmission electron microscopic investigation pertaining to the geometrical arrangement of the nanoparticles in the host matrix were carried out in the case of Ag–TiO_2 and Au–TiO_2 nanocomposites leading to the mechanism for the formation of larger nanoparticles in the Ag–TiO_2 system. The 3D images of the two systems clearly show that the large nanoparticles are on the top surface and the smaller nanoparticles are embedded in the matrix of TiO_2. The morphology of the nanocomposite thin film was explained by a two step model involving the formation of small nanoparticles during vacuum phase deposition or on the growing surface and after the deposition process, the formation of larger particles through particle coarsening by Ostwald ripening [172] and surface segregation. Hence, it was shown that only MVF is not enough to understand the properties, because of the bimodal particle size distribution.

Strong relation exists between the optical properties and the microstructure of the nanocomposites. The position, intensity and width of the SPR are understood to be function of the MVF, particle size, shape, distribution, interparticle separation, the type of metal and the surrounding dielectric medium. In the case of Au–TiO_2 nanocomposites, the change in the MVF from 7 % to 15 % Au has resulted in the SPR shift from 572 nm to 584 nm and in Ag–TiO_2 nanocomposites from 13 % to 47 % Ag, resulted a red shift from 488 nm to 640 nm which corresponds to an increasing particle size and a decrease in interparticle distance from the TEM analysis. On peak deconvolution of the SPR spectrum with a Gauss fit from 15 % Ag nanocomposite, a prominent peak at around 498 nm and a shoulder peak at around 630 nm was observed. Similar to the case of the equal intensity double plasmon resonance [100] and as the theoretical treatments predict a red–shift and broadening of the corresponding peaks upon interaction between plasmon resonances in different particles [187], the results were explained with regard to the strong coupling of plasmon resonances.

Thus, from the 3D nanostructure of the nanocomposite thin films obtained by electron tomography, the optical extinction and the peak deconvolution, it can be concluded that the lateral and perpendicular plasmon coupling between the larger nanoparticles and the smaller nanoparticles give rise to the SPR resonances at 630 nm and 498 nm.

Special attention was laid on the SHI irradiation of the nanocomposites. On SHI irradiation with the 100 MeV Ag^{8+} ion beam at fluences of 1×10^{12}, 3×10^{12} and 1×10^{13} ions/cm^2 changes in the optical spectrum like narrowing of the SPR peak, along with associated changes in the particle morphologies have been observed. Thus, through the variation of the ion beam fluence and the MVF, a red shift of the SPR was observed from 572 nm to 648 nm (Au–TiO_2) and 487 nm to 577 nm (Ag–TiO_2). As the particle diameter increases to about 12 nm, there is a corresponding shift of the SPR towards higher wavelengths in agreement to the experimental calculations by Quinten [188] (page 147). The SHI irradiation of the 13 % Ag nanocomposite resulted in the formation of a large single crystalline TiO at a particular fluence of 3×10^{12} ions/cm^2 which was confirmed by SAED studies together with the HRTEM and EDX analysis. The TiO phase formation with increasing fluence was understood by the interaction of two different counteracting mechanisms, where at lower fluences, the tendency towards the formation of TiO existed with the larger unaffected areas. At higher fluences, the destruction of the evolved TiO phase into fragments was evident. This served as an evidence for the counter play between "hit" and "no–hit", "single–hit" and "multiple–hit" processes. A comparative study involving the in–situ heating of the Ag–TiO_2 nanocomposites in the TEM confirms the absence of the formation of TiO. The refractive index is a key parameter in optical properties which have been altered due to SHI irradiation. Amorphous TiO_2, crystalline TiO_2 with Anatase structure and TiO have different refractive indices of 2.05 [140], 2.54 [192] and 2.27 [193]. Hence, an interplay between the associated change in the refractive index and the particle size distribution in the resulting red shift from 465 nm to 550 nm existed. All the studied MVFs followed a similar trend of the SPR shift towards higher fluences. Thus the nanostructuring of the nanocomposites was possible by SHI irradiation.

Changes of the microstructure of the composite film upon annealing allowed to demon-

strate the absence of the formation of TiO but rather only the crystallization of the TiO_2. As it was suggested that the shift in SPR depends on the original microstructure, the annealing temperatures and duration of the annealing [129], in–situ annealing studies confirmed the changes in the microstructure of the Ag–TiO_2 and Au–TiO_2 nanocomposites. The change in the morphology was attributed to Ostwald ripening phenomena which led to particle coarsening and also the changes in the structure of the matrix. In contrast to the SHI irradiation under non–equilibrium conditions, during in–situ heating, there is a transformation of the amorphous TiO_2 matrix into a crystalline TiO_2 with Anatase–type structure. No evidence towards the formation of TiO nanostructures were observed. Also, the change in the particle size is higher in the case of SHI irradiation than that through in–situ heating. Hence through in–situ heating, the nanostructuring of the nanocomposites by the formation of TiO nanostructures is not possible, but rather crystallization of the matrix occurs with marginal particle size increase.

Functionality of the nanocomposites in terms of their antibacterial properties were studied. In this study cultures of B.megaterium, S.aureus, S.epidermidis and E.Coli were used to study the effect on the Ag–TiO_2 nanocomposites. The retardation of the growth of E.coli cultures was found to be maximum on the substrates coated with Ag–TiO_2 nanocomposites than the TiO_2 and the Au–TiO_2 substrates. In this work, two different approaches were used for the antibacterial testing of the nanocomposites. The direct visualization of the bacterial growth was a sensitive method of antibacterial analysis compared to the modified conventional disc–diffusion method. Additionally, silver ion release studies were carried out at different MVFs by using XPS and UV-Vis/NIR spectroscopies. Enhancement of the silver ion release after SHI irradiation at a fluence of 1×10^{12} ions/cm^2 was observed to the fact that the ion trajectories after irradiation provide better silver ion release.

PTFE based nanocomposites with Ag/Au nanoparticles with varying MVF have been also prepared using the process of co–sputtering. The growth of metallic nanoclusters in PTFE is due to the differences in their cohesive energies. Through the process of co–sputtering, on increasing the MVF, an interplay between the particle morphology and the interparticle spacing was observed. SHI irradiation of metal nanoparticles embedded in

PTFE matrix was necessary to understand the role of matrix after ion irradiation. Thin films of Ag–PTFE nanocomposites on glass and TEM grids were subjected to irradiation with 100 MeV Ag^{8+} ions at fluences of 3×10^{11}, 6×10^{11} and 1×10^{12} ions/cm^2 delivered by the Pelletron accelerator at IUAC. The results from the optical and TEM studies show that there is a marginal dissolution of Ag nanoparticles along with a slight agglomeration of nanoparticles after SHI irradiation. At higher fluences of 3×10^{12} ions/cm^2, carbon rich areas were observed, which were the result of the carbonization along the ion tracks as has been reported previously in different polymer matrices [33, 213, 216] and in PTFE matrix [217]. This also contributes to the alteration in the plasmonic properties of the PTFE based nanocomposites.

In bimetallic nanocomposites based on sandwich geometry, the changes in the particle plasmon spectra of sandwiched Au nanoclusters as a result of the presence of Ag nanoclusters in their vicinity and vice versa was studied. Also, the optimum dielectric barrier thickness for the observation of EIDPR was reported [100]. This allows tuning of the double PP resonances by tailoring the dielectric separation, in contrast to an earlier reported difficult experimental procedure [220]. The dipole-dipole coupling was found to be strongest for a TAF spacing of 3.3 nm. The layer thickness is confirmed by XPS studies through the attenuation of the silver signal from XPS spectra. The present geometrical way of tuning provides a unique means of tailoring the plasmon resonance with high accuracy. This plasmon tuning obtained through thickness control is much superior to that obtained through particle size control and also one of its kind in tuning the EIDPR. These results also indicate that the EIDPR occurs at critical coupling levels, a fact suggesting that the experimental geometry used in experiments at hand may offer new directions for investigations of surface enhanced optical properties involving double plasmon resonances from nanoclusters. Engineering of the plasmon decay and implementation of various functions to the present structures are further to be investigated.

Chapter 7

Outlook

Generally, the fabrication of optical filters and components is done by vacuum deposition techniques and they require an array of sophisticated equipment: a high vacuum chamber, very pure deposition materials, a means of evaporating these materials, thermal control, a mechanism for monitoring the thickness of the materials deposited and many characterization techniques. The development of these nanomaterials and the devices which exploit them require effective integrated relationships from the physics, chemistry and biological point of views. Considering the results from the 3D electron tomography, apart from the work towards the noble metal–polymer system, many unraveled systems still exist. The systems of noble metals in different hosts like Al_2O_3, ITO, MgO, SiN, TiN and ZrO_2 thin films prepared by the process of co–sputtering are still necessary to be investigated in depth in order to understand the particle size distribution in different matrices with varying cohesive energies as they offer interesting applications [239–241]. The important questions which arise are the geometrical arrangement of the nanoparticles in the host matrix, thereby the morphology of the nanocomposite and their functional properties are tailored. Not only does the nanocomposite have the properties from the matrix but also additional functionalities from the nanoparticles and their arrangement in the host thereby can be altered according to the applicational requirement.

Transmission electron tomography allows to reconstruct the 3D morphology of the specimen with a nanometer resolution. It appears thus well–suited to the study of nanocom-

posite thin films and is currently applied to various fields of nanotechnology. Since the catalytic, electronic and optical properties of nanocomposite thin films strongly depend on their size, distribution and shape, the determination of their exact 3D morphology is of importance in order to understand and control their physical properties.

From the results obtained by using the SHI irradiation, the changes in the matrix crystallinity has induced changes in the refractive index, which would be extremely useful to derive a better understanding of the SHI irradiation by ellipsometry. Additional fine tuning the fluences and the MVFs in order to optimize the parameters required for nanostructuring by the formation of TiO would be much helpful. Additionally, the changes in the morphology of the nanoparticles on SHI irradiation is interesting to be study not only by using electron tomography but also by using the polarizing light where, e.g., the changes resulting from the elongation of the nanoparticles can be observed through the splitting in the SPR peak.

The encouraging results from the antibacterial studies from TiO_2 based nanocomposites need a further detailed study, i.e., towards the silver ion release behavior. The changes in the antibacterial properties of the nanocomposites resulting from the changes in the morphology of the nanocomposite is an interesting point to investigate. On the other hand, establishment of a possible mechanism towards the antibacterial activity of these Ag based nanocomposites is still necessary to be carried out. Despite the antibacterial properties, the cyto–compatibility of these coatings would be really interesting to study. The growth of defined cells on the nanocomposites with quiet less MVFs would be interesting to understand the effect of these nanocomposites. Cyto–compatibility would be certainly dependent on the morphology of the nanocomposite coatings, but to establish a relationship between the MVF and the cell growth would result in a boon to the medical community.

The properties of nanostructured materials in nature are extremely interesting like the bones, shells and teeth. These natural hybrid materials combine the strength of ceramics and the stretchability of polymers. Thereby, making the systems with combination of oxides and polymers are quiet interesting. Various efforts towards the creation of composites of oxides and polymers through wet chemistry are in progress. The use of oxides as filler materials in a polymer host is really interesting towards applications which demand flexibility, e.g.,

bendable, transparent electronics, sensors, long lasting bone and dental implants, etc. But the efforts through the application of vapor phase deposition techniques is not yet completely in practice. These nanocomposites also tend to exhibit huge changes in the optical properties resulting from the changes in the refractive index, which might be at a later stage enhanced by the use of the third component as noble metals. An interplay of optical properties resulting from the changes in the MVF and the refractive index is helpful to study. The optical and the antibacterial properties would not only be interesting but also a variety of functional properties making the materials multi–functional nanocomposites.

Advancement in the field of transmission electron microscopy has led towards the development of new filters with the capability of studying the electron energy loss spectroscopy. Studying the response of the nanocomposites with defined geometries would be quiet useful to compare the plasmons from light and electrons.

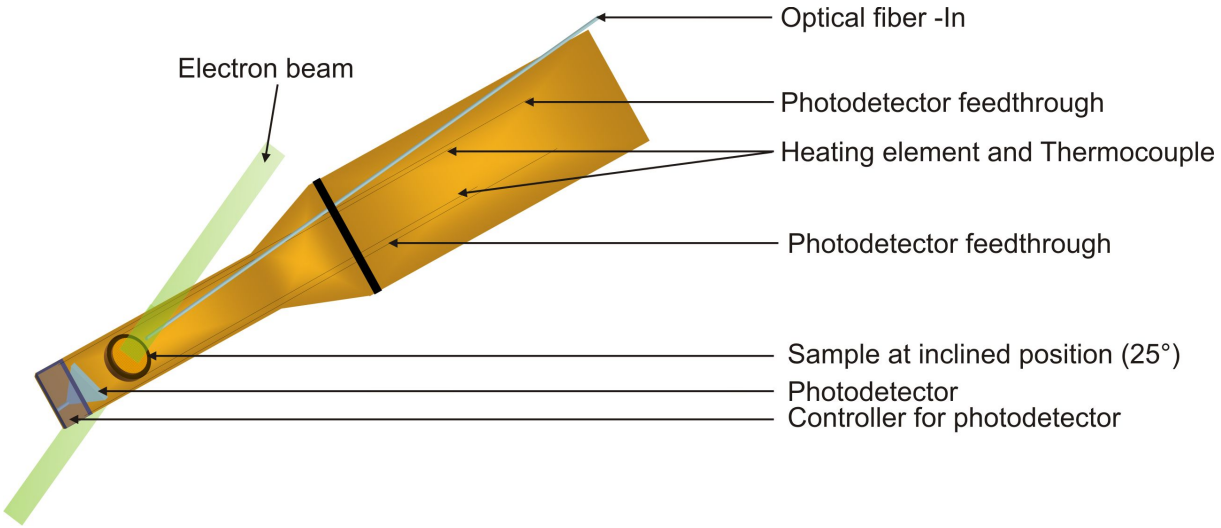

***Figure 7.1*:** *sketch of a optic sample holder with a possibility to measure the optical response from a localized area as a result of the change in the interparticle distance by in–situ heating.*

The possibility of constructing an optical sample holder for transmission electron microscope so that the sample holder has the ability to heat the samples accompanied with the possibility to define light at a localized and variable area. This gives the possibility to spectroscopically measure the response with the change in the interparticle distance as a result of the heating until the growth of the nanoparticle. Fig. 7.1 depicts a sketch of such a light holder. This gives the possibility to study in–situ, the interaction of light on a few

nanoparticles. Also, this gives the advantage to observe the changes in the structure of the nanoparticles under the electron beam through heating and simultaneously the response in the form of the particle plasmon resonance.

List of Figures

Bibliography

[1] Y. Xia and N. J. Halas, Shape-controlled synthesis and surface plasmonic properties of metallic nanostructures, *MRS Bulletin*, 30: pp. 338–348 (**2005**).

[2] B. Wiley, Y. Sun, J. Chen, H. Cang, Z. Y. Li, X. Li and Y. Xia, Shape-controlled synthesis of silver nanostructures, *MRS Bulletin*, 30: pp. 356–361 (**2005**).

[3] Z. Y. Li, N. P. Young, M. Di Vece, S. Palomba, R. E. Palmer, A. L. Bleloch, B. C. Curley, R. L. Johnston, J. Jiang and J. Yuan, Three-dimensional atomic-scale structure of size-selected gold nanoclusters., *Nature*, 451, 7174: pp. 46–48 (**2008**), ISSN 1476-4687, doi:10.1038/nature06470.

[4] A. Polman and H. Atwater, Plasmonics: Optics at the nanoscale, *Materials Today*, 8, 1: pp. 56–56 (**2005**), ISSN 13697021, doi:10.1016/S1369-7021(04)00685-6.

[5] C. B. Murray, S. Sun, H. Doyle and T. Betley, Monodisperse 3d (Co , Ni , Fe) nanoparticles and their assembly into nanoparticle superlattices, *MRS Bulletin*, , December: pp. 985–991 (**2001**).

[6] W. Caseri, Nanocomposites of polymers and metals or semiconductors: Historical background and optical properties, *Macromolecular Rapid Communications*, 21, 11: pp. 705–722 (**2000**), ISSN 1022-1336, doi:10.1002/1521-3927(20000701)21:11<705::AID-MARC705>3.0.CO;2-3.

[7] B. Hvolbaek, T. V. W. Janssens, B. S. Clausen, H. Falsig, C. H. Christensen and J. K. Nerskov, Catalytic activity of Au nanoparticles, *Review Literature And Arts Of The Americas*, 2, 4: pp. 14–18 (**2007**).

[8] A. O. Govorov and H. H. Richardson, Generating heat with metal nanoparticles, *Nano Today*, 2, 1: pp. 30–38 (**2007**).

[9] F. X. Gu, R. Karnik, A. Z. Wang, F. Alexis, E. Levy-Nissenbaum, S. Hong, R. S. Langer and O. C. Farokhzad, Targeted nanoparticles for cancer therapy, *Nano Today*, 2, 3: pp. 14–21 (**2007**).

[10] M. Arruebo, R. Fernández-pacheco, M. R. Ibarra and J. Santamaría, Magnetic nanoparticles for drug delivery, *Nano Today*, 2, 3: pp. 22–32 (**2007**).

[11] F. Faupel, V. Zaporojtchenko, T. Strunskus and M. Elbahri, Metal-polymer nanocomposites for functional applications, *Advanced Engineering Materials*, 12, 12: pp. 1177–1190 (**2010**), ISSN 14381656, doi:10.1002/adem.201000231.

[12] R. Mezzenga and J. Ruokolainen, Nanocomposites: Nanoparticles in the right place., *Nature Materials*, 8, 12: pp. 926–8 (**2009**), ISSN 1476-1122, doi:10.1038/nmat2576.

[13] N. Cioffi, L. Torsi, N. Ditaranto, G. Tantillo, L. Ghibelli, L. Sabbatini, T. Bleve-zacheo, M. D'Alessio, P. G. Zambonin and E. Traversa, Copper nanoparticle/polymer composites with antifungal and bacteriostatic properties, *Chemistry of Materials*, 17, 21: pp. 5255–5262 (**2005**).

[14] J. Yu, J. Xiong, B. Cheng and S. Liu, Fabrication and characterization of AgâTiO2 multiphase nanocomposite thin films with enhanced photocatalytic activity, *Applied Catalysis B: Environmental*, 60, 3-4: pp. 211–221 (**2005**), ISSN 09263373, doi:10.1016/j.apcatb.2005.03.009.

[15] K. Matsubara and T. Tatsuma, Morphological changes and multicolor photochromism of Ag nanoparticles deposited on single–crystalline TiO2 surfaces, *Advanced Materials*, 19, 19: pp. 2802–2806 (**2007**), ISSN 09359648, doi:10.1002/adma.200602823.

[16] S.-h. Lee, *Photocatalytic nanocomposites based on TiO2 and carbon nanotubes*, Ph.D. thesis, University of Florida (**2004**).

[17] P. K. Stoimenov, R. L. Klinger, G. L. Marchin and K. J. Klabunde, Metal oxide nanoparticles as bactericidal agents, *Langmuir*, 18, 13: pp. 6679–6686 (**2002**).

[18] Y. Ohko, T. Tatsuma, T. Fujii, K. Naoi, C. Niwa, Y. Kubota and A. Fujishima, Multicolour photochromism of TiO2 films loaded with silver nanoparticles, *Nature Materials*, 2, 1: pp. 29–31 (**2003**), ISSN 1476-1122, doi:10.1038/nmat796.

[19] X. Chen and S. S. Mao, Titanium dioxide nanomaterials: synthesis, properties, modifications, and applications., *Chemical Reviews*, 107, 7: pp. 2891–2959 (**2007**), ISSN 0009-2665, doi:10.1021/cr0500535.

[20] J. Roiz, A. Oliver, E. Muñoz, L. Rodríguez Fernández and J. M. Hernández, Modification of the optical properties of Ag-implanted silica by annealing in two different atmospheres, *Journal of Applied Physics*, 95, 4: pp. 1783–1791 (**2004**), ISSN 00218979, doi:10.1063/1.1635653.

[21] M. Lee, I. Chang, P. Dobson and B. Cantor, Microstructural characterization of nanocomposite thin films of Ag-SiO2, Ag-ZnO and Ag-Si, *Materials Science and Engineering: A*, 179-180: pp. 545–551 (**1994**), ISSN 09215093, doi:10.1016/0921-5093(94)90264-X.

[22] C. Sella, M. Maaza, B. Pardo, F. Dunsteter, J. Martin and M. Saintecatherine, Microstructure and growth mechanism of Pt-Al2O3 co-sputtered nanocermet films studied by SAXS, TEM and AFM, *Physica A: Statistical and Theoretical Physics*, 241, 1-2: pp. 192–198 (**1997**), ISSN 03784371, doi:10.1016/S0378-4371(97)00082-4.

[23] S. Chen, P. Kuo, a. Sun, C. Chou, Y. Fang and T. Wu, Microstructure and magnetic properties of nanocomposite FePt/MgO and FePt/Ag films, *Journal of Magnetism and Magnetic Materials*, 304, 1: pp. e47–e49 (**2006**), ISSN 03048853, doi:10.1016/j.jmmm.2006.01.172.

[24] R. MiedziÅski, J. Ebothé, G. Kozlowski, J. Kasperczyk, I. Kityk, I. Fuks-Janczarek, K. Nouneh, M. Oyama, M. Matusiewicz and A. Reshak, Laser induced microrelief superstructure of Ag/ITO seed-mediated nanocomposites, *Superlattices and Microstructures*, 46, 4: pp. 637–644 (**2009**), ISSN 07496036, doi:10.1016/j.spmi.2009.04.006.

[25] V. Smentkowski, Trends in sputtering, *Progress in Surface Science*, 64, 1-2: pp. 1–58 (**2000**), ISSN 00796816, doi:10.1016/S0079-6816(99)00021-0.

[26] A. Krasheninnikov and K. Nordlund, Ion and electron irradiation-induced effects in nanostructured materials, *Journal of Applied Physics*, 107, 7: p. 071,301 (**2010**), ISSN 00218979, doi:10.1063/1.3318261.

[27] M. Shirai, K. Tsumori, M. Kutsuwada, K. Yasuda and S. Matsumura, Morphological change in FePt nanogranular thin films induced by swift heavy ion irradiation, *Nuclear Instruments and Methods in Physics Research Section B: Beam Interactions with Materials and Atoms*, 267, 10: pp. 1787–1791 (**2009**), ISSN 0168583X, doi:10.1016/j.nimb.2009.03.079.

[28] S. Klaumunzer, Ion hammering of silica colloids, *Nuclear Instruments and Methods in Physics Research Section B: Beam Interactions with Materials and Atoms*, 215, 3-4: pp. 345–352 (**2004**), ISSN 0168583X, doi:10.1016/j.nimb.2003.08.031.

[29] S. Klaumunzer, Modification of nanostructures by high-energy ion beams, *Nuclear Instruments and Methods in Physics Research Section B: Beam Interactions with Materials and Atoms*, 244, 1: pp. 1–7 (**2006**), ISSN 0168583X, doi:10.1016/j.nimb.2005.11.006.

[30] A. Gutzmann and S. Klaumünzer, Shape instability of amorphous materials during high-energy ion bombardment, *Nuclear Instruments and Methods in Physics Research Section B: Beam Interactions with Materials and Atoms*, 127-128: pp. 12–17 (**1997**), ISSN 0168583X, doi:10.1016/S0168-583X(96)00841-5.

[31] S. Roorda, T. van Dillen, A. Polman, C. Graf, A. van Blaaderen and B. J. Kooi, Aligned gold nanorods in silica made by ion irradiation of coreâshell colloidal particles, *Advanced Materials*, 16, 3: pp. 235–237 (**2004**), ISSN 0935-9648, doi:10.1002/adma.200305742.

[32] J. J. Penninkhof, C. Graf, T. van Dillen, a. M. Vredenberg, A. van Blaaderen and A. Polman, Angle-dependent extinction of anisotropic silica/Au core/shell colloids made via ion irradiation, *Advanced Materials*, 17, 12: pp. 1484–1488 (**2005**), ISSN 0935-9648, doi:10.1002/adma.200401742.

[33] A. Adla, H. Fuess and C. Trautmann, Characterization of heavy ion tracks in polymers by transmission electron microscopy, *Journal of Polymer Science Part B: Polymer Physics*, 41, 22: pp. 2892–2901 (**2003**), ISSN 0887-6266, doi:10.1002/polb.10614.

[34] A. Heilmann, *Polymer films with embedded metal nanoparticles*, Springer Verlag (**2003**), ISBN 978-3-540-43151-0.

[35] U. Kreibig and M. Vollmer, *Optical properties of metal clusters*, Springer Verlag (**1995**), ISBN 978-3-540-57836-9.

[36] P. K. Jain, X. Huang, I. H. El-Sayed and M. a. El-Sayed, Review of some interesting surface plasmon resonance-enhanced properties of noble metal nanoparticles and their applications to biosystems, *Plasmonics*, 2, 3: pp. 107–118 (**2007**), ISSN 1557-1955, doi:10.1007/s11468-007-9031-1.

[37] J. L. Elechiguerra, J. L. Burt, J. R. Morones, A. Camacho-Bragado, X. Gao, H. H. Lara and M. J. Yacaman, Interaction of silver nanoparticles with HIV-1, *Journal of Nanobiotechnology*, 3, 6: pp. 1–10 (**2005**), ISSN 1477-3155, doi: 10.1186/1477-3155-3-6.

[38] S. P. Fricker, Medical uses of gold compounds : Past, present and future, *Gold Bulletin*, 29, 2: pp. 53–60 (**1996**).

[39] L. Armelao, D. Barreca, G. Bottaro, a. Gasparotto, S. Gross, C. Maragno and E. Tondello, Recent trends on nanocomposites based on Cu, Ag and Au clusters: A closer look, *Coordination Chemistry Reviews*, 250, 11-12: pp. 1294–1314 (**2006**), ISSN 00108545, doi:10.1016/j.ccr.2005.12.003.

[40] P. Gould, Nanoparticles probe biosystems, *Materials Today*, 7, 2: pp. 36–43 (**2004**), ISSN 13697021, doi:10.1016/S1369-7021(04)00082-3.

[41] L. M. Liz-marz, Nanometals: formation and color, *Materials Today*, , February: pp. 26–31 (**2004**).

[42] C. S. Thaxton, N. L. Rosi and C. A. Mirkin, Optically and chemically encoded nanoparticle materials for DNA and protein detection, *MRS Bulletin*, 30: pp. 376–380 (**2005**).

[43] P. K. Jain, I. H. El-Sayed and M. A. El-Sayed, Au nanoparticles target cancer, *Nano Today*, 2, 1: pp. 18–29 (**2007**), doi:10.1016/S1748-0132(07)70016-6.

[44] H. Takele, A. Kulkarni, S. Jebril, V. S. K. Chakravadhanula, C. Hanisch, T. Strunskus, V. Zaporojtchenko and F. Faupel, Plasmonic properties of vapour-deposited polymer composites containing Ag nanoparticles and their changes upon annealing, *Journal of Physics D: Applied Physics*, 41, 12: p. 125,409 (**2008**).

[45] V. Zaporojtchenko, R. Podschun, U. Schürmann, A. Kulkarni and F. Faupel, Physico-chemical and antimicrobial properties of co-sputtered AgâAu/PTFE nanocomposite coatings, *Nanotechnology*, 17, 19: pp. 4904–4908 (**2006**), ISSN 0957-4484, doi: 10.1088/0957-4484/17/19/020.

[46] A. J. Betts, D. P. Dowling, M. L. McConnell and C. Pope, The influence of platinum on the performance of silverâplatinum anti-bacterial coatings, *Materials & Design*, 26, 3: pp. 217–222 (**2005**), ISSN 02613069, doi:10.1016/j.matdes.2004.02.006.

[47] J. Wang, J. Li, L. Ren, a. Zhao, P. Li, Y. Leng, H. Sun and N. Huang, Antibacterial activity of silver surface modified polyethylene terephthalate by filtered cathodic vacuum arc method, *Surface and Coatings Technology*, 201, 15: pp. 6893–6896 (**2007**), ISSN 02578972, doi:10.1016/j.surfcoat.2006.09.109.

[48] I. Chopra, The increasing use of silver-based products as antimicrobial agents: a useful development or a cause for concern ?, *The Journal of Antimicrobial Chemotherapy*, 59, 4: pp. 587–90 (**2007**), ISSN 0305-7453, doi:10.1093/jac/dkm006.

[49] J. Thiel, L. Pakstis, S. Buzby, M. Raffi, C. Ni, D. J. Pochan and S. I. Shah, Antibacterial properties of silver-doped titania., *Small*, 3, 5: pp. 799–803 (**2007**), ISSN 1613-6829, doi:10.1002/smll.200600481.

[50] H. Takele, H. Greve, C. Pochstein, V. Zaporojtchenko and F. Faupel, Plasmonic properties of Ag nanoclusters in various polymer matrices, *Nanotechnology*, 17, 14: pp. 3499–3505 (**2006**), ISSN 1361-6528, doi:10.1088/0957-4484/17/14/023.

[51] A. Biswas, O. C. Aktas, U. Schürmann, U. Saeed, V. Zaporojtchenko, F. Faupel and T. Strunskus, Tunable multiple plasmon resonance wavelengths response from mul-

ticomponent polymer-metal nanocomposite systems, *Applied Physics Letters*, 84, 14: pp. 2655–2657 (**2004**), ISSN 00036951, doi:10.1063/1.1697626.

[52] P. Falaras, I. M. Arabatzis, T. Stergiopoulos and M. C. Bernard, Enhanced activity of silver modified thin-film TiO2 photocatalysts, *International Journal of Photoenergy*, 5, 3: pp. 123–130 (**2003**), ISSN 1110-662X, doi:10.1155/S1110662X03000230.

[53] W. A. de Heer, The physics of simple metal clusters: Experimental aspects and simple models, *Rewiews of Modern Physics*, 65, 3: pp. 611–676 (**1993**).

[54] T. A. Dankovich and D. G. Gray, Bactericidal paper impregnated with silver nanoparticles for point-of-use water treatment, *Environmental Science & Technology* (**2011**), ISSN 1520-5851, doi:10.1021/es103302t.

[55] L. Armelao, D. Barreca, G. Bottaro, A. Gasparotto, C. Maccato, C. Maragno, E. Tondello, U. L. Štangar, M. Bergant and D. Mahne, Photocatalytic and antibacterial activity of TiO2 and Au/TiO2 nanosystems, *Nanotechnology*, 18, 37: p. 375,709 (**2007**), ISSN 0957-4484, doi:10.1088/0957-4484/18/37/375709.

[56] C. Wang, P. Zhang, L. Zheng, X. Xiao and Y. Rong, Influence of annealing on microstructure and magnetic transport of FeCo Al2O3 nanogranular films, *Thin Solid Films*, 516, 10: pp. 3422–3430 (**2008**), ISSN 00406090, doi:10.1016/j.tsf.2007.12.121.

[57] S. Arai, S. Tsukimoto and H. Saka, In-situ transmission electron microscope observation of melting of aluminum particles, *Microscopy and Microanalysis*, 4: pp. 264–268 (**1998**), ISSN 1435-8115.

[58] H. Saka, T. Kamino, S. Arai and K. Sasaki, In-situ heating transmission electron microscopy, *MRS Bulletin*, 33, February: pp. 93–100 (**2008**).

[59] N. Martin, C. Rousselot, D. Rondot, F. Palmino and R. Mercier, Microstructure modification of amorphous titanium oxide thin films during annealing treatment, *Thin Solid Films*, 300, 1-2: pp. 113–121 (**1997**), ISSN 00406090, doi:10.1016/S0040-6090(96)09510-7.

[60] L. Tröger, H. Hünnefeld, S. Nunes, M. Oehring and D. Fritsch, Structural characterization of catalytically active metal nanoclusters in Polyamide (imide) films with high metal loading, *The Journal of Physical Chemistry B*, 101, 8: pp. 1279–1291 (**1997**), ISSN 1520-6106, doi:10.1021/jp962096i.

[61] K. Günther-Schade, H. L. Castricum, H. J. Ziegler, H. Bakker and F. Faupel, Free volume changes in mechanically milled PS and PC studied by positron annihilation lifetime spectroscopy (PALS), *Polymer Engineering and Science*, 44, 7: pp. 1351–1359 (**2004**), ISSN 0032-3888, doi:10.1002/pen.20130.

[62] L. Martinu, H. Biederman and J. Zemek, Metal doped polymer films prepared by simultaneous plasma polymerization of tetrafluoromethane and evaporation of gold, *Vacuum*, 35, 4-5: pp. 171–176 (**1985**), ISSN 0042207X, doi:10.1016/0042-207X(85)90654-2.

[63] A. Biswas, Z. Marton, J. Kanzow, J. Kruse, V. Zaporojtchenko, F. Faupel and T. Strunskus, Controlled generation of Ni nanoparticles in the capping layers of Teflon AF by vapor-phase tandem evaporation, *Nano Letters*, 3, 1: pp. 69–73 (**2003**), ISSN 1530-6984, doi:10.1021/nl020228f.

[64] H. Biederman, RF sputtering of polymers and its potential application, *Vacuum*, 59, 2-3: pp. 594–599 (**2000**), ISSN 0042207X, doi:10.1016/S0042-207X(00)00321-3.

[65] U. Schürmann, W. Hartung, H. Takele, V. Zaporojtchenko and F. Faupel, Controlled syntheses of Agâpolytetrafluoroethylene nanocomposite thin films by co-sputtering from two magnetron sources, *Nanotechnology*, 16, 8: pp. 1078–1082 (**2005**), ISSN 0957-4484, doi:10.1088/0957-4484/16/8/014.

[66] H. Greve, A. Biswas, U. Schürmann, V. Zaporojtchenko and F. Faupel, Self-organization of ultrahigh-density FeâNiâCo nanocolumns in TeflonÂ® AF, *Applied Physics Letters*, 88, 12: p. 123,103 (**2006**), ISSN 00036951, doi:10.1063/1.2187436.

[67] W. R. Grove, On the Electro-chemical polarity of gases, *Philosophical Transactions of the Royal Society of London*, 142: pp. 87–101 (**1852**), ISSN 0261-0523, doi:10.1098/rstl.1852.0008.

[68] W. R. Grove, On some anomalous cases of electrical decomposition, *Philosophical Magazine Series 4*, 5, 31: p. 203 (**1853**), doi:10.1080/14786445308647227.

[69] G. Wehner and G. Anderson, *Handbook of thin film technology*, McGraw-Hill, Tx (**1970**), ISBN 978-0070397422.

[70] M. Ohring, *Materials science of thin films*, Elsevier, second edition (**2002**), ISBN 978-0-12-524975-1.

[71] B. Chapman, *Glow discharge processes: Sputtering and plasma etching*, Wiley-VCH Verlag (**1980**), ISBN 978-0-471-07828-9.

[72] F. Faupel, V. Zaporojtchenko, T. Strunskus, J. Erichsen, K. Dolgner and M. Kiene, Fundamental aspects of polymer metallization, in E. Sacher, editor, *Metallization of Polymers 2, ACS symposium series*, pp. 73–96, Kluwer Academic/Plenum Publishers, New York (**2002**).

[73] J. Zekonyte, V. Zaporojtchenko and F. Faupel, Investigation of the drastic change in the sputter rate of polymers at low ion fluence, *Nuclear Instruments and Methods in Physics Research Section B: Beam Interactions with Materials and Atoms*, 236, 1-4: pp. 241–248 (**2005**), ISSN 0168583X, doi:10.1016/j.nimb.2005.04.043.

[74] P. Lobl, M. Huppertz and D. Mergel, Nucleation and growth in TiO2 films prepared by sputtering and evaporation, *Thin Solid Films*, 251, 1: pp. 72–79 (**1994**), ISSN 00406090, doi:10.1016/0040-6090(94)90843-5.

[75] V. Zaporojtchenko, K. Behnke, T. Strunskus and F. Faupel, Determination of condensation coefficients of metals on polymer surfaces, *Surface Science*, 454-456, 1-2: pp. 412–416 (**2000**), ISSN 00396028, doi:10.1016/S0039-6028(00)00234-X.

[76] V. Zaporojtchenko, K. Behnke, T. Strunskus and F. Faupel, Condensation coefficients of noble metals on polymers: a novel method of determination by x-ray photoelectron spectroscopy, *Surface and Interface Analysis*, 30, 1: pp. 439–443 (**2000**), ISSN 0142-2421, doi:10.1002/1096-9918(200008)30:1<439::AID-SIA787>3.0.CO;2-K.

[77] K. Kambe, Cohesive energy of noble metals, *Physical Review*, 99, 2: pp. 419–422 (**1955**), ISSN 0031-899X, doi:10.1103/PhysRev.99.419.

[78] S. Klaumunzer, Ion tracks in quartz and vitreous silica, *Nuclear Instruments and Methods in Physics Research Section B: Beam Interactions with Materials and Atoms*, 225, 1-2: pp. 136–153 (**2004**), ISSN 0168583X, doi:10.1016/j.nimb.2004.05.014.

[79] S. Klaumünzer, M.-d. Hou and G. Schumacher, Coulomb explosions in a metallic glass due to the passage of fast heavy ions ?, *Physical Review Letters*, 57, 7: pp. 850–853 (**1986**), ISSN 0031-9007, doi:10.1103/PhysRevLett.57.850.

[80] A. Meftah, F. Brisard, J. Costantini, E. Dooryhee, M. Hage-Ali, M. Hervieu, J. Stoquert, F. Studer and M. Toulemonde, Track formation in SiO2 quartz and the thermal-spike mechanism, *Physical Review B*, 49, 18: pp. 12,457–12,463 (**1994**), ISSN 0163-1829, doi:10.1103/PhysRevB.49.12457.

[81] D. Fink and R. Klett, Latent ion tracks in polymers for future use in nanoelectronics : An overview of the present state-of-the-art, *Brazilian Journal of Physics*, 25, 1: pp. 54–75 (**1995**).

[82] C. Trautmann, Modifications induced by swift heavy ions, *Bulletin of Materials Science*, 22, 3: pp. 679–686 (**1999**), ISSN 0250-4707, doi:10.1007/BF02749985.

[83] D. Fink and L. T. Chadderton, Ion-solid interaction: status and perspectives, *Brazilian Journal of Physics*, 35, 3b: pp. 735–740 (**2005**), ISSN 0103-9733, doi:10.1590/S0103-97332005000500003.

[84] D. Fink, P. Alegaonkar, A. Petrov, A. Berdinsky, V. Rao, M. Müller, K. Dwivedi and L. Chadderton, The emergence of new ion tract applications, *Radiation Measurements*, 36, 1-6: pp. 605–609 (**2003**), ISSN 13504487, doi:10.1016/S1350-4487(03)00209-9.

[85] M. Toulemonde, C. Dufour and E. Paumier, Transient thermal process after a high-energy heavy-ion irradiation of amorphous metals and semiconductors, *Physical Review B*, 46, 22: pp. 14,362–14,369 (**1992**), ISSN 0163-1829, doi:10.1103/PhysRevB.46.14362.

[86] R. Johnson and W. Brown, Electronic mechanisms for sputtering of condensed-gas solids by energetic ions, *Nuclear Instruments and Methods in Physics Research*, 198, 1: pp. 103–118 (**1982**), ISSN 01675087, doi:10.1016/0167-5087(82)90059-X.

[87] R. L. Fleischer, P. B. Price and R. M. Walker, Ion explosion spike mechanism for formation of charged-particle tracks in solids, *Journal of Applied Physics*, 36, 11: p. 3645 (**1965**), ISSN 00218979, doi:10.1063/1.1703059.

[88] G. Schiwietz, G. Xiao, P. L. Grande, E. Luderer, R. Pazirandeh and U. Stettner, Determination of the electron temperature in the thermal spike of amorphous carbon, *Europhysics Letters (EPL)*, 47, 3: pp. 384–390 (**1999**), ISSN 0295-5075, doi:10.1209/epl/i1999-00400-0.

[89] A. Ryazanov, A. Volkov and S. Klaumünzer, Model of track formation, *Physical Review B*, 51, 18: pp. 12,107–12,115 (**1995**), ISSN 0163-1829, doi:10.1103/PhysRevB.51.12107.

[90] M. Toulemonde, J. Costantini, C. Dufour, A. Meftah, E. Paumier and F. Studer, Track creation in SiO2 and BaFe12O19 by swift heavy ions: a thermal spike description, *Nuclear Instruments and Methods in Physics Research Section B: Beam Interactions with Materials and Atoms*, 116, 1-4: pp. 37–42 (**1996**), ISSN 0168583X, doi:10.1016/0168-583X(96)00007-9.

[91] A. Meftah, F. Brisard, J. Costantini, M. Hage-Ali, J. Stoquert, F. Studer and M. Toulemonde, Swift heavy ions in magnetic insulators: A damage-cross-section velocity effect, *Physical Review B*, 48, 2: pp. 920–925 (**1993**), ISSN 0163-1829, doi:10.1103/PhysRevB.48.920.

[92] J. Biersack and L. Haggmark, A Monte Carlo computer program for the transport of energetic ions in amorphous targets, *Nuclear Instruments and Methods*, 174, 1-2: pp. 257–269 (**1980**), ISSN 0029554X, doi:10.1016/0029-554X(80)90440-1.

[93] R. Sanz, J. Jensen, A. Johansson, M. Skupinski, G. Possnert, M. Boman, M. Hernandez-Vélez, M. Vazquez and K. Hjort, Well-ordered nanopore arrays in rutile TiO2 single crystals by swift heavy ion-beam lithography, *Nanotechnology*, 18, 305303: pp. 1–6 (**2007**), ISSN 0957-4484, doi:10.1088/0957-4484/18/30/305303.

[94] K. L. Kelly, E. Coronado, L. L. Zhao and G. C. Schatz, The optical properties of metal nanoparticles: The influence of size, shape, and dielectric environment, *The Journal of Physical Chemistry B*, 107, 3: pp. 668–677 (**2003**), ISSN 1520-6106, doi:10.1021/jp026731y.

[95] H. Raether, *Surface plasmons*, Springer Verlag (**1988**), ISBN 0387173633.

[96] W. L. Barnes, A. Dereux and T. W. Ebbesen, Surface plasmon subwavelength optics, *Nature*, 424, 6950: pp. 824–30 (**2003**), ISSN 1476-4687, doi:10.1038/nature01937.

[97] A. Henglein, Small-particle research: physicochemical properties of extremely small colloidal metal and semiconductor particles, *Chemical Reviews*, 89, 8: pp. 1861–1873 (**1989**), ISSN 0009-2665, doi:10.1021/cr00098a010.

[98] T. Ung, L. M. Liz-Marzán and P. Mulvaney, Optical properties of thin films of Au@SiO2 particles, *The Journal of Physical Chemistry B*, 105, 17: pp. 3441–3452 (**2001**), ISSN 1520-6106, doi:10.1021/jp003500n.

[99] S. Underwood and P. Mulvaney, Effect of the solution refractive index on the color of gold colloids, *Langmuir*, 10, 10: pp. 3427–3430 (**1994**), ISSN 0743-7463, doi:10.1021/la00022a011.

[100] V. S. K. Chakravadhanula, M. Elbahri, U. Schürmann, H. Takele, H. Greve, V. Zaporojtchenko and F. Faupel, Equal intensity double plasmon resonance of bimetallic quasi-nanocomposites based on sandwich geometry, *Nanotechnology*, 19, 22: p. 225,302 (**2008**), ISSN 0957-4484, doi:10.1088/0957-4484/19/22/225302.

[101] U. Kreibig and L. Genzel, Optical absorption of small metallic particles, *Surface Science*, 156: pp. 678–700 (**1985**), ISSN 00396028, doi:10.1016/0039-6028(85)90239-0.

[102] U. Kreibig, Electronic properties of small silver particles: The optical constants and their temperature dependence, *Small*, 4, 7: p. 999 (**1974**), doi:10.1088/0305-4608/4/7/007.

[103] S. Link and M. a. El-Sayed, Size and temperature dependence of the plasmon absorption of colloidal gold nanoparticles, *The Journal of Physical Chemistry B*, 103, 21: pp. 4212–4217 (**1999**), ISSN 1520-6106, doi:10.1021/jp984796o.

[104] C. Noguez, Surface plasmons on metal nanoparticles: The influence of shape and physical environment, *Journal of Physical Chemistry C*, 111, 10: pp. 3806–3819 (**2007**), ISSN 1932-7447, doi:10.1021/jp066539m.

[105] S. Link and M. a. El-Sayed, Spectral properties and relaxation dynamics of surface plasmon electronic oscillations in gold and silver nanodots and nanorods, *The Journal of Physical Chemistry B*, 103, 40: pp. 8410–8426 (**1999**), ISSN 1520-6106, doi:10.1021/jp9917648.

[106] K. I. Winey and R. A. Vaia, Polymer nanocomposites, *MRS Bulletin*, 32, 04: pp. 314–322 (**2011**), ISSN 0883-7694, doi:10.1557/mrs2007.229.

[107] L. M. Liz-Marzán, Tailoring surface plasmons through the morphology and assembly of metal nanoparticles, *Langmuir*, 22, 1: pp. 32–41 (**2006**), ISSN 0743-7463, doi:10.1021/la0513353.

[108] Q. Cheng, C. Li, V. Pavlinek, P. Saha and H. Wang, Surface-modified antibacterial TiO2/Ag+ nanoparticles: Preparation and properties, *Applied Surface Science*, 252, 12: pp. 4154–4160 (**2006**), ISSN 01694332, doi:10.1016/j.apsusc.2005.06.022.

[109] W. Glomm, Functionalized gold nanoparticles for applications in bionanotechnology, *Journal of Dispersion Science and Technology*, 26, 3: pp. 389–414 (**2005**), ISSN 0193-2691, doi:10.1081/DIS-200052457.

[110] J. H. Leibfarth and R. H. Persellin, Mechanisms of action of gold, *Agents and Actions*, 11, 5: pp. 458–472 (**1981**), ISSN 0065-4299, doi:10.1007/BF02004707.

[111] D. N. Williams, S. H. Ehrman and T. R. Pulliam Holoman, Evaluation of the microbial growth response to inorganic nanoparticles, *Journal of Nanobiotechnology*, 4: pp. 1–8 (**2006**), ISSN 1477-3155, doi:10.1186/1477-3155-4-3.

[112] Y. Cao, R. Jin and C. a. Mirkin, DNA-modified core-shell Ag/Au nanoparticles, *Journal of the American Chemical Society*, 123, 32: pp. 7961–2 (**2001**), ISSN 0002-7863.

[113] I. Tokareva and E. Hutter, Hybridization of oligonucleotide-modified silver and gold nanoparticles in aqueous dispersions and on gold films., *Journal of the American Chemical Society*, 126, 48: pp. 15,784–9 (**2004**), ISSN 0002-7863, doi:10.1021/ja046779k.

[114] W. Wang, X. Chen and S. Efrima, Silver nanoparticles capped by long-chain unsaturated carboxylates, *The Journal of Physical Chemistry B*, 103, 34: pp. 7238–7246 (**1999**), ISSN 1520-6106, doi:10.1021/jp991101q.

[115] L. Quaroni and G. Chumanov, Preparation of polymer-coated functionalized silver nanoparticles, *Journal of the American Chemical Society*, 121, 45: pp. 10,642–10,643 (**1999**), ISSN 0002-7863, doi:10.1021/ja992088q.

[116] J. Gao, J. Fu, C. Lin, J. Lin, Y. Han, X. Yu and C. Pan, Formation and photoluminescence of silver nanoparticles stabilized by a two-armed polymer with a crown ether core, *Langmuir*, 20, 22: pp. 9775–9 (**2004**), ISSN 0743-7463, doi:10.1021/la049197p.

[117] Q. L. Feng, J. Wu, G. Q. Chen, F. Z. Cui, T. N. Kim and J. O. Kim, A mechanistic study of the antibacterial effect of silver ions on Escherichia coli and Staphylococcus aureus, *Journal of Biomedical Materials Research*, 52, 4: pp. 662–8 (**2000**), ISSN 0021-9304.

[118] Y. Matsumura, K. Yoshikata, S.-i. Kunisaki and T. Tsuchido, Mode of bactericidal action of silver zeolite and its comparison with that of silver nitrate, *Applied and Environmental Microbiology*, 69, 7: pp. 4278–4281 (**2003**), ISSN 0099-2240, doi:10.1128/AEM.69.7.4278-4281.2003.

[119] I. Sondi and B. Salopek-Sondi, Silver nanoparticles as antimicrobial agent: a case study on E. coli as a model for gram-negative bacteria, *Journal of colloid and interface science*, 275, 1: pp. 177–82 (**2004**), ISSN 0021-9797, doi:10.1016/j.jcis.2004.02.012.

[120] J. R. Morones, J. L. Elechiguerra, A. Camacho, K. Holt, J. B. Kouri, J. T. Ramírez and M. J. Yacaman, The bactericidal effect of silver nanoparticles, *Nanotechnology*, 16, 10: pp. 2346–2353 (**2005**), ISSN 0957-4484, doi:10.1088/0957-4484/16/10/059.

[121] M. Yamanaka, K. Hara and J. Kudo, Bactericidal actions of a silver ion solution on Escherichia coli, studied by energy-filtering transmission electron microscopy and proteomic analysis, *Applied and environmental microbiology*, 71, 11: pp. 7589–93 (**2005**), ISSN 0099-2240, doi:10.1128/AEM.71.11.7589-7593.2005.

[122] M. Rai, A. Yadav and A. Gade, Silver nanoparticles as a new generation of antimicrobials, *Biotechnology advances*, 27, 1: pp. 76–83 (**2009**), ISSN 1873-1899, doi:10.1016/j.biotechadv.2008.09.002.

[123] F. Raimondi, G. G. Scherer, R. Kötz and A. Wokaun, Nanoparticles in energy technology: examples from electrochemistry and catalysis, *Angewandte Chemie*, 44, 15: pp. 2190–209 (**2005**), ISSN 1433-7851, doi:10.1002/anie.200460466.

[124] Y. Liu, X. Wang, F. Yang and X. Yang, Excellent antimicrobial properties of mesoporous anatase TiO2 and Ag/TiO2 composite films, *Microporous and Mesoporous Materials*, 114, 1-3: pp. 431–439 (**2008**), ISSN 13871811, doi:10.1016/j.micromeso.2008.01.032.

[125] M. Manera, J. Spadavecchia, D. Buso, C. de Julián Fernández, G. Mattei, A. Martucci, P. Mulvaney, J. Pérez-Juste, R. Rella, L. Vasanelli and P. Mazzoldi, Optical gas sensing of TiO2 and TiO2/Au nanocomposite thin films, *Sensors and Actuators B: Chemical*, 132, 1: pp. 107–115 (**2008**), ISSN 09254005, doi:10.1016/j.snb.2008.01.014.

[126] I. Tanahashi, H. Iwagishi and G. Chang, Localized surface plasmon resonance sensing properties of photocatalytically prepared Au/TiO2 films, *Materials Letters*, 62, 17-18: pp. 2714–2716 (**2008**), ISSN 0167577X, doi:10.1016/j.matlet.2008.01.023.

[127] G. Li and K. A. Gray, The solid–solid interface: Explaining the high and unique photocatalytic reactivity of TiO2 based nanocomposite materials, *Chemical Physics*, 339, 1-3: pp. 173–187 (**2007**), ISSN 03010104, doi:10.1016/j.chemphys.2007.05.023.

[128] T. Pradeep, Noble metal nanoparticles for water purification: A critical review, *Thin Solid Films*, 517, 24: pp. 6441–6478 (**2009**), ISSN 00406090, doi:10.1016/j.tsf.2009.03.195.

[129] H. Takele, *Optical and electrical properties of metal-polymer nanocomposites prepared by vapor-phase co-evaporation*, Ph.D. thesis, Institute for Materials Science, Chair for Multicomponent Materials, Technical Faculty, Christian Albrechts University of Kiel (**2008**).

[130] W. Cheng, M. J. Campolongo, J. J. Cha, S. J. Tan, C. C. Umbach, D. A. Muller and D. Luo, Free-standing nanoparticle superlattice sheets controlled by DNA, *Nature Materials*, 8: pp. 519–525 (**2009**), doi:10.1038/NMAT2440.

[131] B. Samir, *STEM-HAADF nanotomography : application to nanomaterials*, Ph.D. thesis, INSA de Lyon (**2009**).

[132] P. A. Midgley and R. E. Dunin-Borkowski, Electron tomography and holography in materials science., *Nature materials*, 8, 4: pp. 271–80 (**2009**), ISSN 1476-1122, doi:10.1038/nmat2406.

[133] K. J. Batenburg, S. Bals, J. Sijbers, C. Kübel, P. A. Midgley, J. C. Hernandez, U. Kaiser, E. R. Encina, E. A. Coronado and G. Van Tendeloo, 3D imaging of nanomaterials by discrete tomography., *Ultramicroscopy*, 109, 6: pp. 730–40 (**2009**), ISSN 0304-3991, doi:10.1016/j.ultramic.2009.01.009.

[134] http://www.amira.com/.

[135] C. Kuebel, T.-C. Lee, D. Su, J.-S. Luo, H.-M. Lo and J. Russell, Application of Electron Tomography for Semiconductor Device Analysis, *Microscopy and Microanalysis*, 12, S02: p. 1552 (**2006**), ISSN 1431-9276, doi:10.1017/S1431927606065068.

[136] A. Sbaei, Synthesis, characterization, and antimicrobial properties of Ag, Au-polymer nanocomposite films (**2007**).

[137] V. Kotnur, Ag ion release from nanocomposites: A plasmonic study for antimicrobial coatings (**2009**).

[138] S. S. Martinos, Optical absorption spectra for silver spherical particles, *Physical Review B*, 39, 2: pp. 1363–1364 (**1989**).

[139] A. Dakka, J. Lafait, C. Sella, M. Maaza and M. Abd-Lefdil, Optical study of Ag-TiO 2 nanocermet thin films prepared by R . F . co-sputtering, *The European Physical Journal Applied Physics*, 114: pp. 105–114 (**2000**).

[140] W. Lee, S. Woo, J. Kim, S. Choi and K. Oh, Preparation and properties of amorphous TiO2 thin films by plasma enhanced chemical vapor deposition, *Thin Solid Films*, 237, 1-2: pp. 105–111 (**1994**), ISSN 00406090, doi:10.1016/0040-6090(94)90245-3.

[141] D. Buso, J. Pacifico, a. Martucci and P. Mulvaney, Gold-Nanoparticle-Doped TiO2 Semiconductor Thin Films: Optical Characterization, *Advanced Functional Materials*, 17, 3: pp. 347–354 (**2007**), ISSN 1616301X, doi:10.1002/adfm.200600349.

[142] I. M. Arabatzis, T. Stergiopoulos, D. Andreeva, S. Kitova, S. G. Neophytides and P. Falaras, Characterization and photocatalytic activity of Au/TiO2 thin films for azo-dye degradation, *Journal of Catalysis*, 220: pp. 127–135 (**2003**), doi:10.1016/S0021-9517(03)00241-0.

[143] S. Cho, S. Lee, S.-g. Oh, S. J. Park, W. M. Kim, M. Chung, K. B. Song, T. S. Lee and S. G. Kim, Optical properties of Au nanocluster embedded dielectric films, *Thin Solid Films*, 377-378: pp. 97–102 (**2000**).

[144] S. Hazra, A. Gibaud and C. Sella, Role of ceramic matrix and Au fraction on the morphology and optical properties of cosputtered Au-ceramic thin films, *Journal of Applied Physics*, 101, 113532: pp. 1–6 (**2007**), doi:10.1063/1.2745124.

[145] M. Manera, J. Spadavecchia, D. Buso, C. Dejulianfernandez, G. Mattei, A. Martucci, P. Mulvaney, J. Perezjuste, R. Rella, L. Vasanelli and P. Mazzoldi, Optical gas sensing of TiO2 and TiO2/Au nanocomposite thin films, *Sensors and Actuators B: Chemical*, 132, 1: pp. 107–115 (**2008**), ISSN 09254005, doi:10.1016/j.snb.2008.01.014.

[146] T. Sasaki, N. Koshizaki, M. Koinuma and Y. Matsumoto, PREPARATION OF M/TiO2 (M = Au, Pt) NANOCOMPOSITE FILMS USING CO-SPUTTERING METHOD, *NanoStructured Materials*, 12: pp. 511–514 (**1999**).

[147] K. Zakrzewska, Nanocermets TiO2:Au(Ag) for photoanodes, *Thin Solid Films*, 451-452: pp. 93–97 (**2004**), ISSN 00406090, doi:10.1016/j.tsf.2003.11.060.

[148] W. Li, Z. Bin, C. LiXian and Z. WenJun, Fabrication of ZnO nanorods in ionic liquids and their photoluminescent properties, *Science in China Series B: Chemistry*, 50, 2: pp. 224–229 (**2007**), ISSN 1006-9291, doi:10.1007/s11426-007-0032-x.

[149] M. S. Chen and D. W. Goodman, The structure of catalytically active gold on titania., *Science (New York, N.Y.)*, 306, 5694: pp. 252–5 (**2004**), ISSN 1095-9203, doi:10.1126/science.1102420.

[150] H. Tada, T. Ishida, A. Takao and S. Ito, Drastic enhancement of TiO2-photocatalyzed reduction of nitrobenzene by loading Ag clusters., *Langmuir: the ACS journal of surfaces and colloids*, 20, 19: pp. 7898–7900 (**2004**), ISSN 0743-7463, doi:10.1021/la049167m.

[151] L. Zhang, J. C. Yu, H. Y. Yip, Q. Li, K. W. Kwong, A.-W. Xu and P. K. Wong, Ambient Light Reduction Strategy to Synthesize Silver Nanoparticles and Silver-Coated TiO 2 with Enhanced Photocatalytic and Bactericidal Activities, *Langmuir*, 19, 24: pp. 10,372–10,380 (**2003**), ISSN 0743-7463, doi:10.1021/la035330m.

[152] K. Naoi, Y. Ohko and T. Tatsuma, Switchable rewritability of Ag-TiO2 nanocomposite films with multicolor photochromism., *Chemical communications (Cambridge, England)*, , 10: pp. 1288–1290 (**2005**), ISSN 1359-7345, doi:10.1039/b416139d.

[153] Y. Tian and T. Tatsuma, Plasmon-induced photoelectrochemistry at metal nanoparticles supported on nanoporous TiO2., *Chemical communications (Cambridge, England)*, , 16: pp. 1810–1811 (**2004**), ISSN 1359-7345, doi:10.1039/b405061d.

[154] H. Wolpert, Optical Filters in Nature, *Optics and Photonics News*, 20, 2: pp. 22–27 (**2009**), ISSN 1047-6938, doi:10.1364/OPN.20.2.000022.

[155] K. Zakrzewska, Nanocermets TiO2:Au(Ag) for photoanodes, *Thin Solid Films*, 451-452: pp. 93–97 (**2004**), ISSN 00406090, doi:10.1016/j.tsf.2003.11.060.

[156] J. Yoon, T. Sasaki, N. Koshizaki and E. Traversa, Preparation and characterization of M/TiO2 (M = Ag, Au, Pt) nanocomposite thin films, *Scripta Materialia*, 44, 8-9: pp. 1865–1868 (**2001**), ISSN 13596462, doi:10.1016/S1359-6462(01)00732-1.

[157] H. M. Gong, S. Xiao, X. R. Su, J. B. Han and Q. Q. Wang, Photochromism and two-photon luminescence of Ag-TiO(2) granular composite films activated by near infrared ps/fs pulses., *Optics express*, 15, 21: pp. 13,924–13,929 (**2007**), ISSN 1094-4087.

[158] U. Schürmann, H. Takele, V. Zaporojtchenko and F. Faupel, Optical and electrical properties of polymer metal nanocomposites prepared by magnetron co-sputtering, *Thin Solid Films*, 515, 2: pp. 801–804 (**2006**), ISSN 00406090, doi:10.1016/j.tsf.2005.12.249.

[159] V. S. K. Chakravadhanula, T. Hrkac, V. Zaporojtchenko, R. Podschun, V. G. Kotnur, A. Kulkarni, T. Strunskus, L. Kienle and F. Faupel, Nanostructural and functional properties of Ag-TiO2 coatings prepared by co-sputtering deposition technique, *Journal of Nanoscience and Nanotechnology*, 11 (**2011**), doi:10.1166/jnn.2011.3881.

[160] V. Zaporojtchenko, J. Zekonyte, A. Biswas and F. Faupel, Controlled growth of nanosize metal clusters on polymers by using VPD method, *Surface Science*, 532-535, 10 June 2003: pp. 300–305 (**2003**), ISSN 00396028, doi:10.1016/S0039-6028(03)00128-6.

[161] A. Dakka, J. Lafait, C. Sella, S. Berthier, M. Abd-Lefdil, J.-c. Martin and M. Maaza, Optical properties of Ag â TiO 2 nanocermet films deposition techniques, *Applied Optics*, 39, 13: pp. 2745–2753 (**2000**).

[162] H. P. Marques, A. R. Canário, A. M. C. Moutinho and O. M. N. D. Teodoro, Shaping Ag clusters on titania, *Journal of Physics: Conference Series*, 61: pp. 775–779 (**2007**), ISSN 1742-6588, doi:10.1088/1742-6596/61/1/155.

[163] H. Marques, A. R. Canario, A. M. C. Moutinho and O. M. N. D. Teodoro, Work function changes in the Ag deposition on TiO2 (110), *Vacuum*, 82: pp. 1425–1427 (**2008**), ISSN 0042207X, doi:10.1016/j.vacuum.2008.03.016.

[164] Y. Mishra, S. Mohapatra, D. Kabiraj, B. Mohanta, N. Lalla, J. Pivin and D. Avasthi, Synthesis and characterization of Ag nanoparticles in silica matrix by atom beam sputtering, *Scripta Materialia*, 56, 7: pp. 629–632 (**2007**), ISSN 13596462, doi: 10.1016/j.scriptamat.2006.12.008.

[165] R. Paul, R. N. Gayen, S. Hussain, V. Khanna, R. Bhar and a. K. Pal, Synthesis and characterization of composite films of silver nanoparticles embedded in DLC matrix prepared by plasma CVD technique, *The European Physical Journal Applied Physics*, 47, 1: p. 10,502 (**2009**), ISSN 1286-0042, doi:10.1051/epjap/2009086.

[166] D. J. De Rosier and A. Klug, Reconstruction of Three Dimensional Structures from Electron Micrographs, *Nature*, 217: pp. 130–134 (**1968**), doi:doi:10.1038/217130a0.

[167] M. Weyland and P. A. Midgley, Electron tomography, *Materials Today*, 7, 12: pp. 32–40 (**2004**), ISSN 13697021, doi:10.1016/S1369-7021(04)00569-3.

[168] H. Oh and P. F. Green, Polymer chain dynamics and glass transition in athermal polymer/nanoparticle mixtures., *Nature materials*, 8, 2: pp. 139–43 (**2009**), ISSN 1476-1122, doi:10.1038/nmat2354.

[169] Y. Zhao, K. Thorkelsson, A. J. Mastroianni, T. Schilling, J. M. Luther, B. J. Rancatore, K. Matsunaga, H. Jinnai, Y. Wu, D. Poulsen, A. P. Alivisatos and T. Xu, Small-molecule-directed nanoparticle assembly towards stimuli-responsive nanocomposites, *Nature materials*, 8, October: pp. 979 – 985 (**2009**), doi:10.1038/NMAT2565.

[170] P. Midgley, 3D electron microscopy in the physical sciences: the development of Z-contrast and EFTEM tomography, *Ultramicroscopy*, 96, 3-4: pp. 413–431 (**2003**), ISSN 03043991, doi:10.1016/S0304-3991(03)00105-0.

[171] J. R. Kremer, D. N. Mastronarde and J. R. McIntosh, Computer visualization of three-dimensional image data using IMOD., *Journal of structural biology*, 116, 1: pp. 71–6 (**1996**), ISSN 1047-8477, doi:10.1006/jsbi.1996.0013.

[172] J. H. Yao, K. Elder, H. Guo and M. Grant, Theory and simulation of Ostwald ripening, *Physical Review B*, 47, 21: pp. 14,110–14,125 (**1993**).

[173] S. Bartkowski, M. Neumann, E. Kurmaev, V. Fedorenko, S. Shamin, V. Cherkashenko, S. Nemnonov, a. Winiarski and D. Rubie, Electronic structure of titanium monoxide, *Physical Review B*, 56, 16: pp. 10,656–10,667 (**1997**), ISSN 0163-1829, doi: 10.1103/PhysRevB.56.10656.

[174] A. N. Enyashin and A. L. Ivanovskii, Modeling of the atomic structure and thermal stability of titanium monoxide nanocrystals, *Russian Journal of Inorganic Chemistry*, 51, 8: pp. 1302–1306 (**2006**), ISSN 0036-0236, doi:10.1134/S0036023606080171.

[175] M. Zribi, M. Kanzari and B. Rezig, Structural, morphological and optical properties of thermal annealed TiO thin films, *Thin Solid Films*, 516, 7: pp. 1476–1479 (**2008**), ISSN 00406090, doi:10.1016/j.tsf.2007.07.195.

[176] P. Stadelmann, EMS - a software package for electron diffraction analysis and HREM image simulation in materials science, *Ultramicroscopy*, 21, 2: pp. 131–145 (**1987**), ISSN 03043991, doi:10.1016/0304-3991(87)90080-5.

[177] Z. Li, S. Miyake, M. Makino and Y. Wu, Microstructure and properties of nanocrystalline titanium monoxide films synthesized by inductively coupled plasma assisted reactive direct current magnetron sputtering, *Applied Surface Science*, 255, 5: pp. 2370–2374 (**2008**), ISSN 01694332, doi:10.1016/j.apsusc.2008.07.108.

[178] D. Fink, *Fundamentals of Ion–Irradiated Polymers*, Springer Verlag, springer s edition (**2004**), ISBN 978-3-540-04027-9.

[179] G. Bacmeister and W. Enge, Observations of the latent track structure in polymers by diffusion measurements, *Nuclear Instruments and Methods in Physics Research Section B: Beam Interactions with Materials and Atoms*, 131, 1-4: pp. 64–70 (**1997**), ISSN 0168583X, doi:10.1016/S0168-583X(97)00333-9.

[180] T. Turowski, *Schockwellenmodell zur Beschreibung des ionendichteabhängigen Diffusionsverhaltens bestrahlter Polymerfolien*, Ph.D. thesis, Christian-Albrechts-Universität zu Kiel (**2001**).

[181] C. Riedel and R. Spohr, Statistical properties of etched nuclear tracks: Analytical theory and computer simulation, *Radiation Effects*, 42: pp. 69–75 (**1979**).

[182] C. Riedel and R. Spohr, Correcting overlapping counts in dose calibration at high event-densities, *Nuclear Tracks*, 5, 3: pp. 265–270 (**1981**), ISSN 0191278X, doi: 10.1016/0191-278X(81)90004-4.

[183] S. A. Maier, P. G. Kik, L. A. Sweatlock and H. A. Atwater, Energy transport in metal nanoparticle plasmon waveguides, in *Mater. Res. Soc. Symp. Proc.*, volume 777, pp. 1–12 (**2003**).

[184] J. P. Kottmann and O. J. Martin, Retardation-induced plasmon resonances in coupled nanoparticles, *Optics letters*, 26, 14: pp. 1096–8 (**2001**), ISSN 0146-9592.

[185] S. Nie, Probing single molecules and single nanoparticles by surface-enhanced raman scattering, *Science*, 275, 5303: pp. 1102–1106 (**1997**), ISSN 00368075, doi:10.1126/science.275.5303.1102.

[186] P. Mulvaney, Surface plasmon spectroscopy of nanosized metal particles, *Langmuir*, 12, 3: pp. 788–800 (**1996**), ISSN 0743-7463, doi:10.1021/la9502711.

[187] G. Chumanov, K. Sokolov and T. M. Cotton, Unusual extinction spectra of nanometer-sized silver particles arranged in two-dimensional arrays, *The Journal of Physical Chemistry*, 100, 13: pp. 5166–5168 (**1996**), ISSN 0022-3654, doi:10.1021/jp9536716.

[188] M. Quinten, *Optical properties of nanoparticle systems: Mie and beyond*, Wiley-VCH Verlag GmbH & Co. KGaA (**2011**), ISBN 978-3-527-41043-9.

[189] M. Elbahri, M. K. Hedayati, V. S. K. Chakravadhanula, M. Jamali, T. Strunskus, V. Zaporojtchenko and F. Faupel, Omnidirectional Transparent Conducting Metal based Plasmonic Nanocomposite By, *Advanced Materials*, pp. 1–17 (**2011**), doi: 10.1002/adma.201003811.

[190] J. J. Mock, D. R. Smith and S. Schultz, Local Refractive Index Dependence of Plasmon Resonance Spectra from Individual Nanoparticles, *Nano Letters*, 3, 4: pp. 485–491 (**2003**), ISSN 1530-6984, doi:10.1021/nl0340475.

[191] A. D. McFarland and R. P. Van Duyne, Single silver nanoparticles as real-time optical sensors with zeptomole sensitivity, *Nano Letters*, 3, 8: pp. 1057–1062 (**2003**), ISSN 1530-6984, doi:10.1021/nl034372s.

[192] Z. Wang, Optical properties of anatase TiO2 thin films prepared by aqueous sol-gel process at low temperature, *Thin Solid Films*, 405, 1-2: pp. 50–54 (**2002**), ISSN 00406090, doi:10.1016/S0040-6090(01)01767-9.

[193] E. Assim, Optical constants of titanium monoxide TiO thin films, *Journal of Alloys and Compounds*, 465, 1-2: pp. 1–7 (**2008**), ISSN 09258388, doi:10.1016/j.jallcom.2007.10.059.

[194] J. R. Morones and W. Frey, Environmentally sensitive silver nanoparticles of controlled size synthesized with PNIPAM as a nucleating and capping agent, *Langmuir*, 23, 15: pp. 8180–6 (**2007**), ISSN 0743-7463, doi:10.1021/la7008336.

[195] G. Fu, P. S. Vary and C.-t. Lin, Anatase TiO2 Nanocomposites for Antimicrobial Coatings, *The Journal of Physical Chemistry B*, 109, 18: pp. 8889–8898 (**2005**).

[196] L. Lifen, J. Barford and Y. King Lun, Non-UV germicidal activity of fresh TiO2 and Ag/TiO2, *Journal of Environmental Sciences*, 21, 5: pp. 700–706 (**2009**), ISSN 10010742, doi:10.1016/S1001-0742(08)62327-X.

[197] W.-C. Chiang, L. R. Hilbert, C. Schroll, T. Tolker-Nielsen and P. Mø ller, Bacterial inhibiting surfaces caused by the effects of silver release and/or electrical field, *Electrochimica Acta*, 54, 1: pp. 108–115 (**2008**), ISSN 00134686, doi:10.1016/j.electacta.2008.02.112.

[198] T. Hirakawa and P. V. Kamat, Charge separation and catalytic activity of Ag@TiO2 core-shell composite clusters under UV-irradiation., *Journal of the American Chemical Society*, 127, 11: pp. 3928–3934 (**2005**), ISSN 0002-7863, doi:10.1021/ja042925a.

[199] C. Werry, J. M. Lawrence and P. J. Sanderson, Contamination of detergent cleaning solutions during hospital cleaning, *Journal of Hospital Infection*, 11, 1: pp. 44–49 (**1988**), ISSN 01956701, doi:10.1016/0195-6701(88)90038-2.

[200] D. Fink, *Transport Processes in Ion–Irradiated Polymers*, Springer-Verlag (**2004**), ISBN 978-3-540-20943-0.

[201] P. A. Buffat, Dynamical behaviour of nanocrystals in transmission electron microscopy: size, temperature or irradiation effects., *Philosophical Transactions of the Royal Society of London A*, 361, 1803: pp. 291–295 (**2003**).

[202] M. José-Yacaman, C. Gutierrez-Wing, M. Miki, D.-Q. Yang, K. N. Piyakis and E. Sacher, Surface diffusion and coalescence of mobile metal nanoparticles., *The journal of physical chemistry B*, 109, 19: pp. 9703–9711 (**2005**), ISSN 1520-6106, doi:10.1021/jp0509459.

[203] A. BISWAS, D. AVASTHI, D. FINK, J. KANZOW, U. SCHURMANN, S. DING, O. AKTAS, U. SAEED, V. ZAPOROJTCHENKO, F. FAUPEL, R. GUPTA and N. KUMAR, Nanoparticle architecture in carbonaceous matrix upon swift heavy ion irradiation of polymerâmetal nanocomposites, *Nuclear Instruments and Methods in Physics Research Section B: Beam Interactions with Materials and Atoms*, 217, 1: pp. 39–50 (**2004**), ISSN 0168583X, doi:10.1016/j.nimb.2003.09.032.

[204] E. Hutter and J. H. Fendler, Exploitation of Localized Surface Plasmon Resonance, *Advanced Materials*, 16, 19: pp. 1685–1706 (**2004**), ISSN 0935-9648, doi:10.1002/adma.200400271.

[205] D. K. Avasthi and J. C. Pivin, Ion beam for synthesis and modification of nanostructures, *Current Science*, 98, 6: pp. 780–792 (**2010**).

[206] M. Es-Souni, H. Fischer-Brandies and M. Es-Souni, Versatile nanocomposite coatings with tunable cell adhesion and bactericidity, *Advanced Functional Materials*, 18, 20: pp. 3179–3188 (**2008**), ISSN 1616301X, doi:10.1002/adfm.200800354.

[207] G.-F. Wang, X.-M. Tao and R.-X. Wang, Flexible organic light-emitting diodes with a polymeric nanocomposite anode, *Nanotechnology*, 19, 14: p. 145,201 (**2008**), ISSN 0957-4484, doi:10.1088/0957-4484/19/14/145201.

[208] L. Ravagnan, G. Divitini, S. Rebasti, M. Marelli, P. Piseri and P. Milani, Poly(methyl methacrylate)âpalladium clusters nanocomposite formation by supersonic cluster beam deposition: a method for microstructured metallization of polymer surfaces, *Journal of Physics D: Applied Physics*, 42, 8: p. 082,002 (**2009**), ISSN 0022-3727, doi:10.1088/0022-3727/42/8/082002.

[209] A. Camenzind, W. R. Caseri and S. E. Pratsinis, Flame-made nanoparticles for nanocomposites, *Nano Today*, 5, 1: pp. 48–65 (**2010**), ISSN 17480132, doi: 10.1016/j.nantod.2009.12.007.

[210] N. Cioffi, L. Torsi, N. Ditaranto, L. Sabbatini, P. G. Zambonin, D. Chimica, C. Km, L. Ghibelli, M. D. Alessio, D. Biologia, R. Tor, R. Scientifica, T. Bleve-zacheo and E. Traversa, Antifungal activity of polymer-based copper nanocomposite coatings, *Applied Physics Letters*, 85, 12: pp. 2417–2419 (**2004**), doi:10.1063/1.1794381.

[211] Ulrich Schürmann, *Eigenschaften von Polymer-Silber-Nanokompositen hergestellt durch Co-Sputtern*, Ph.D. thesis, Christian-Albrechts-Universität zu Kiel (**2006**).

[212] Jurgita Zekonyte, *Sputtering and surface modification of thermoplastic polymers with low energy ion beams*, Ph.D. thesis (**2005**).

[213] S. K. Srivastava, D. K. Avasthi and E. Pippel, Swift heavy ion induced formation of nanocolumns of C clusters in a Si based polymer, *Nanotechnology*, 17, 10: pp. 2518–2522 (**2006**), ISSN 0957-4484, doi:10.1088/0957-4484/17/10/013.

[214] J. Zhao, A. O. Pinchuk, J. M. McMahon, S. Li, L. K. Ausman, A. L. Atkinson and G. C. Schatz, Methods for describing the electromagnetic properties of silver and gold nanoparticles., *Accounts of chemical research*, 41, 12: pp. 1710–20 (**2008**), ISSN 1520-4898, doi:10.1021/ar800028j.

[215] D. Fink, *Fundamentals of Ion–Irradiated Polymers Fundamentals of Ion–Irradiated Polymers* (**2004**), ISBN 978-3-642-05709-0.

[216] D. Avasthi, J. Singh, a. Biswas and S. Bose, Study on evolution of gases from Mylar under ion irradiation, *Nuclear Instruments and Methods in Physics Research Section B: Beam Interactions with Materials and Atoms*, 146, 1-4: pp. 504–508 (**1998**), ISSN 0168583X, doi:10.1016/S0168-583X(98)00464-9.

[217] J. Prakash, a. Tripathi, S. Khan, J. Pivin, F. Singh, J. Tripathi, S. Kumar and D. Avasthi, Ion beam induced interface mixing of Ni on PTFE bilayer system studied by quadrupole mass analysis and electron spectroscopy for chemical analysis, *Vacuum*, 84, 11: pp. 1275–1279 (**2010**), ISSN 0042207X, doi:10.1016/j.vacuum.2010.02.003.

[218] F. Hubenthal, T. Ziegler, C. Hendrich, M. Alschinger and F. Träger, Tuning the surface plasmon resonance by preparation of gold-core/silver-shell and alloy nanoparticles, *The European Physical Journal D*, 34, 1-3: pp. 165–168 (**2005**), ISSN 1434-6060, doi:10.1140/epjd/e2005-00138-1.

[219] J. H. Hodak, A. Henglein, M. Giersig and G. V. Hartland, Laser-induced inter-diffusion in AuAg coreâshell nanoparticles, *The Journal of Physical Chemistry B*, 104, 49: pp. 11,708–11,718 (**2000**), ISSN 1520-6106, doi:10.1021/jp002438r.

[220] M. Schierhorn and L. M. Liz-Marzán, Synthesis of bimetallic colloids with tailored intermetallic separation, *Nano Letters*, 2, 1: pp. 13–16 (**2002**), ISSN 1530-6984, doi:10.1021/nl015616g.

[221] A. Steinbrück, A. Csáki, G. Festag and W. Fritzsche, Preparation and optical characterization of coreâshell bimetal nanoparticles, *Plasmonics*, 1, 1: pp. 79–85 (**2006**), ISSN 1557-1955, doi:10.1007/s11468-005-9000-5.

[222] J. Sinzig, U. Radtke, M. Quinten and U. Kreibig, Binary clusters: homogeneous alloys and nucleus-shell structures, *Zeitschrift für Physik D Atoms, Molecules and Clusters*, 26, 1-4: pp. 242–245 (**1993**), ISSN 0178-7683, doi:10.1007/BF01429157.

[223] P. Mulvaney, M. Giersig and A. Henglein, Electrochemistry of multilayer colloids: preparation and absorption spectrum of gold-coated silver particles, *The Journal of Physical Chemistry*, 97, 27: pp. 7061–7064 (**1993**), ISSN 0022-3654, doi:10.1021/j100129a022.

[224] G. C. Papavassiliou, Surface plasmons in small Au-Ag alloy particles, *Journal of Physics F: Metal Physics*, 6: pp. L103–L105 (**1976**), doi:10.1088/0305-4608/6/4/004.

[225] J. Gonzalo, D. Babonneau, C. N. Afonso and J.-P. Barnes, Optical response of mixed Ag-Cu nanocrystals produced by pulsed laser deposition, *Journal of Applied Physics*, 96, 9: p. 5163 (**2004**), ISSN 00218979, doi:10.1063/1.1792810.

[226] K. Shida, Multilayer sensing and aggregation approach to environmental perception with one multifunctional sensor, *IEEE Sensors Journal*, 2, 2: pp. 62–72 (**2002**), ISSN 1530-437X, doi:10.1109/JSEN.2002.1000243.

[227] Y. Sun and Y. Xia, Alloying and dealloying processes involved in the preparation of metal Nanoshells through a galvanic replacement reaction, *Nano Letters*, 3, 11: pp. 1569–1572 (**2003**), ISSN 1530-6984, doi:10.1021/nl034765r.

[228] N. Malikova, I. Pastoriza-Santos, M. Schierhorn, N. a. Kotov and L. M. Liz-Marzán, Layer-by-layer assembled mixed spherical and planar gold nanoparticles: Control of interparticle interactions, *Langmuir*, 18, 9: pp. 3694–3697 (**2002**), ISSN 0743-7463, doi:10.1021/la025563y.

[229] S. Nie, Probing Single Molecules and Single Nanoparticles by Surface-Enhanced Raman Scattering, *Science*, 275, 5303: pp. 1102–1106 (**1997**), ISSN 00368075, doi:10.1126/science.275.5303.1102.

[230] M. Quinten, A. Leitner, J. R. Krenn and F. R. Aussenegg, Electromagnetic energy transport via linear chains of silver nanoparticles, *Optics Letters*, 23, 17: pp. 1331–1333 (**1998**).

[231] W. Holland and D. Hall, Surface-plasmon dispersion relation: Shifts induced by the interaction with localized plasma resonances, *Physical Review B*, 27, 12: pp. 7765–7768 (**1983**), ISSN 0163-1829, doi:10.1103/PhysRevB.27.7765.

[232] K.-H. Su, Q.-H. Wei, X. Zhang, J. J. Mock, D. R. Smith and S. Schultz, Interparticle Coupling Effects on Plasmon Resonances of Nanogold Particles, *Nano Letters*, 3, 8: pp. 1087–1090 (**2003**), ISSN 1530-6984, doi:10.1021/nl034197f.

[233] S. a. Zynio, A. V. Samoylov, E. R. Surovtseva, V. M. Mirsky and Y. M. Shirshov, Bimetallic Layers Increase Sensitivity of Affinity Sensors Based on Surface Plasmon Resonance, *Sensors*, 2, 2: pp. 62–70 (**2002**), ISSN 1424-8220, doi: 10.3390/s20200062.

[234] S. R. Ekanayake, M. Ford and M. Cortie, Metal-insulator-metal (MIM) nanocapacitors and effects of material propertieson their operation, *Materials Forum*, 27: pp. 15 – 20 (**2004**).

[235] N. Engheta, A. Salandrino and A. Alù, Circuit Elements at Optical Frequencies: Nanoinductors, Nanocapacitors, and Nanoresistors, *Physical Review Letters*, 95, 9: pp. 1–4 (**2005**), ISSN 0031-9007, doi:10.1103/PhysRevLett.95.095504.

[236] E. J. Heilweil and R. M. Hochstrasser, Nonlinear spectroscopy and picosecond transient grating study of colloidal gold, *The Journal of Chemical Physics*, 82, 11: p. 4762 (**1985**), ISSN 00219606, doi:10.1063/1.448693.

[237] H. Hövel, S. Fritz, A. Hilger, U. Kreibig and M. Vollmer, Width of cluster plasmon resonances: Bulk dielectric functions and chemical interface damping, *Physical Review B*, 48, 24: pp. 18,178–18,188 (**1993**), ISSN 0163-1829, doi:10.1103/PhysRevB.48.18178.

[238] W. Rechberger, A. Hohenau, A. Leitner, J. Krenn, B. Lamprecht and F. Aussenegg, Optical properties of two interacting gold nanoparticles, *Optics Communications*, 220, 1-3: pp. 137–141 (**2003**), ISSN 00304018, doi:10.1016/S0030-4018(03)01357-9.

[239] E. G. Manoilov, Optical and photoluminescent properties of Ag/Al2O3 nanocomposite films obtained by pulsed laser deposition, *Semiconductor Physics, Quantum Electronics & Optoelectronics*, 12, 3: pp. 298–301 (**2009**).

[240] S. Singh and B. D. Gupta, Simulation of a surface plasmon resonance-based fiber-optic sensor for gas sensing in visible range using films of nanocomposites, *Measurement Science and Technology*, 21, 11: p. 115,202 (**2010**), ISSN 0957-0233, doi:10.1088/0957-0233/21/11/115202.

[241] P. H. C. Camargo, K. G. Satyanarayana and F. Wypych, Nanocomposites: synthesis, structure, properties and new application opportunities, *Materials Research*, 12, 1: pp. 1–39 (**2009**), ISSN 1516-1439, doi:10.1590/S1516-14392009000100002.

Acknowledgements

I express my sincere gratitude to the people of Germany for facilitating me to pursue my doctoral studies in Germany. I express my sincere thanks to Prof. Dr. Franz Faupel, Head of the Chair for Multicomponent Materials for his guidance, constant encouragement, support, keeping faith in me and motivating me at all stages, in carrying out my work. It is an honor for me to thank Prof. Dr. Lorenz Kienle for his support during the final stages of my work. I thank profusely Dr. Vladimir Zaporojtchenko for research supervision and guidance. Special thanks to Prof. Dr. Klaus Rätzke for the scientific discussions which were extremely helpful at various stages. I am indebted to Dr. Christoph Mitterbauer and Dr. Klemens Kelm for their fruitful discussions and help rendered during learning advanced techniques of transmission electron microscopy.

I owe my deepest gratitude to Dr. Dietmar Fink and Dr. Christian Kübel for their special discussions, support and cooperation. Special regards to Dr. Devesh Kumar Avasthi and Dr. Yogendra Mishra for their kind cooperation and help during irradiation experiments within the frame of the DFG–DST project. Special thanks to Prof. S. Cruz–Jimenez, UAM Mexico, for valuable discussions that leading to the proposed model for the formation of TiO. I am also thankful to Prof. Dr. Mady Elbahri and Dr. Thomas Strunskus, for their help at various stages in discussing my results.

Special thanks to Dipl.-Ing. Stefan Rehders for design and construction of the equipment and as well as for technical assistance. I am also very grateful to Dipl.-Ing. Rainer Kloth for setting up various devices at various times. They both had very practical and logical solutions for almost anything in the laboratory. Many thanks to Dr. Ulrich Schürmann for being the first person to introduce me into the laboratory of nanocomposites, Dr. Seid

Jebril, Dr. Haile Takele, Dr. Christian Hanisch and Dipl. Phys. Tomislav Hrkac for the kind cooperation during the course of my work with joyful smiles.

This thesis would not have been possible without the support of Dr. Henry Greve, Dr. Jan Kruse, Dr. Ulrich Schürmann, Dr. Stephan Warnat and Dr. Michael Scharnberg. I express my hearty thanks to Dipl.-Geo. Beate Minten, Mrs. Christiane Otte-Hüls, Dipl.-Chem. Sieglinde Kastaun and Mrs. Katrin Brandenburg for all the help they have done regarding the office work. I express my thanks to Prof. Dr. Rainer Adelung for the lectures and fruitful discussions during group seminars.

I would like to thank Dr. Alexander Bartsch, MSc. Burak Erkartal, Dipl.Phys. Viktor Hrkac and MSc. Dawit Gedamu for their nice company during my work in our room.

Thanks to MSc. Girish Kotnur and MSc. Ali Sbaei for helping me in the preparation of samples and for their Masters thesis. My special thanks are to MSc. Amit Kulkarni my friend and a great person for being with me during my stay in Kiel, Germany. Not to forget my parents, my younger brother and my wife, without whose support I could not have done anything. Additionally, Mr. and Mrs. Menon and the members of the Satya Sai Organization, Kiel for their parental support rendered during my stay in Kiel.

I thank the entire group AG – Multicomponent Materials, AG – Synthesis and Real Structure, the Technical Faculty and Deutsche Forschungsgemeinschaft which helped me not only financially during my stay in Kiel, but also made my work interesting by motivating me, giving new directions to my career.

Finally, I would like to thank one and all who have helped me directly or indirectly in completing my doctoral work successfully.

April 21, 2011